TUM School of Computation, Information and Technology

Radiation degradation of III-V multijunction space solar cells

Manuel Wildfeuer

Vollständiger Abdruck der von der TUM School of Computation, Information and Technology der Technischen Universität München zur Erlangung des akademischen Grades eines
Doktors der Ingenieurwissenschaften (Dr.-Ing.)
genehmigten Dissertation.

Vorsitzender
Prof. Dr.-Ing. Klaus Diepold
Prüfer der Dissertation
1. Prof. Dr. Paolo Lugli
2. Prof. Dr.-Ing. Christian Jirauschek

Die Dissertation wurde am 29.03.2022 bei der Technischen Universität München eingereicht und durch die TUM School of Computation, Information and Technology am 09.11.2022 angenommen.

Abstract

Charged particle radiation in space, consisting of protons and electrons trapped in the Van Allen belts as well as of solar flare protons, is the single most important factor that degrades solar cell performance. Currently, a major shift in space photovoltaic power generation is taking place due to two developments: i) New missions employ electric orbit raising, which increases the equivalent radiation fluence by up to a factor of ten. ii) Four-junction devices are gaining momentum in space power generation, which are manufactured by new growth techniques such as metamorphic growth or wafer bonding. Therefore, it is necessary to understand the degradation behavior of both the new four-junction as well as of the currently used three-junction cells in this new environment. With this goal in mind, a degradation campaign was started. Three- and four-junction cells as well as their respective isotype cells were irradiated in particle accelerators with electrons with an energy of 1 and 3 MeV and protons with an energy of 1, 2 and 5 MeV. The energies and fluences were chosen to be representative of the radiation environment in space. The cells were characterized in order to determine their electrical properties and their characteristic degradation curves.

In order to analyze the degradation data, the displacement damage dose method was adapted: the threshold energy for atomic displacement $T_{d,eff}$ was explicitly introduced as fit parameter. With this change, the non-ionizing energy loss was calculated analytically. This led to a collapse of the electron data on a single curve which is necessary to gain the characteristic degradation curve. No additional exponent without physical meaning needed to be introduced, unlike during the previous analysis method.

The adapted analysis method was successfully applied to the degradation data of 4J and 3J cells as well as to their respective isotype cells. Characteristic degradation curves, degradation parameters and threshold energies for atomic displacement were obtained for the short-circuit current, the open-circuit voltage and the power at maximum power point. For the collapse of 3J cell data, GaAs NIEL with a threshold energy of 21 eV was found. For the collapse of 4J cell data, $In_{0.3}Ga_{0.7}As$ NIEL with a threshold energy of 25 eV was found.

The particle environment of a specific electric orbit raising mission was computed. Using the computed particle environment as well as the determined 4J degradation characteristics, the degradation of the cells was determined dependent on the cover glass thickness. It was found that the power at maximum power point degrades to $87\,\%$ of

its original value at the end of the mission when $100\,\mu$m cover glass is used.
Moreover, it was found that the current-voltage characteristics of GaAs cells under illumination exhibit a voltage-dependent photocurrent. The photocurrent has its origin in the voltage-dependent width of the space charge region in combination with a strongly decreased minority carrier diffusion length and was modeled accordingly. By extracting the width of the space charge region from capacitance measurements and the base layer diffusion length from the external quantum efficiency of the cell, the experimental behavior of the photocurrent was reproduced accurately.
Furthermore, a method of determining subcell characteristics of multi-junction cells using pulsed lasers was introduced and results of 3J and 4J cells were determined. The subcells of multi-junction cells, especially of irradiated ones, were directly investigated, which would not be possible with the help of well-established methods relying on the EL or PL spectrum. Pulsed lasers were employed to determine the open-circuit voltage and the dark current-voltage characteristics of all subcells of BOL as well as of electron and proton irradiated 3J and 4J cells. Therefore, this characterization method makes the need for isotype cells obsolete.

Kurzfassung

Geladene Teilchenstrahlung im Weltraum, bestehend aus in den Van-Allen-Gürteln gefangenen Protonen und Elektronen als auch aus von Sonneneruptionen freigesetzten Protonen, ist derjenige Faktor, der für die Degradation von Solarzellleistung hauptsächlich verantwortlich ist. Im Moment findet eine große Veränderung in der photovoltaischen Energieerzeugung im Weltraum statt, was sich anhand der folgenden zwei Entwicklungen zeigt: i) Neue Missionen nutzen elektrische Triebwerke zur Erhöhung der Satellitenumlaufbahn, was die äquivalente Teilchenfluenz um einen Faktor von bis zu zehn erhöht. ii) Vierschicht-Solarzellen werden zukünftig zur Energieerzeugung im Weltraum eingesetzt, welche durch neue Wachstumstechniken wie metamorphes Wachstum oder Waferbonding hergestellt werden. Deshalb ist es notwendig, das Degradationsverhalten der neuen Vierschicht- als auch der gegenwärtig verwendeten Dreischichtzellen in dieser neuen Teilchenumgebung zu verstehen. Um dieses Ziel zu erreichen, wurde eine Bestrahlungskampagne gestartet. Drei- und Vierschichtzellen sowie auch ihre entsprechenden Komponentenzellen wurden in Teilchenbeschleunigern mit Elektronen der Energien 1 and 3 MeV als auch mit Protonen der Energien 1, 2 and 5 MeV bestrahlt. Die Energien und Fluenzen wurden so gewählt, dass sie repräsentativ für die Strahlungsumgebung im Weltraum sind. Die Zellen wurden charakterisiert, um ihre elektrischen Eigenschaften sowie auch ihre charakteristische Degradationskurve zu bestimmen.

Um die Degradationsdaten zu analysieren, wurde die DDD Methode dahingehend angepasst, dass die Schwellenenergie für atomare Versetzungen $T_{d,eff}$ explizit als Anpassungsparameter eingeführt wurde. Mit dieser Änderung wurde der nichtionisierende Energieverlust analytisch berechnet. Das führte dazu, dass die Elektronendaten auf eine einzige gemeinsame Kurve zusammenfallen, was notwendig ist, um eine charakteristische Degradationskurve zu erhalten, ohne einen zusätzlichen Exponenten ohne physikalische Bedeutung einzuführen, was in der bisherigen Analysemethode notwendig war.

Diese veränderte Analysemethode wurde erfolgreich an den Degradationsdaten von 4J und 3J Zellen als auch an deren entsprechenden Komponentenzellen angewendet. Charakteristische Degradationskurven, Degradationsparameter und Schwellenenergien für atomare Versetzung wurden bestimmt für den Kurzschlussstrom, die offene Klemmspannung und die maximale Leistung. Für das Zusammenfallen der 3J-Zelldaten wurde ein GaAs NIEL mit einer Schwellenenergie von 21 eV gefunden. Für das Zusammenfallen der 4J-Zelldaten wurde ein $In_{0.3}Ga_{0.7}As$ NIEL mit einer Schwellenenergie von 25 eV ge-

funden.
Die Teilchenumgebung einer konkreten Satellitenmission mit elektrischen Triebwerken zur Orbiterhöhung wurde berechnet. Unter Verwendung dieser berechneten Teilchenumgebung als auch der bestimmten 4J-Degradationscharakteristik wurde die Degradation der Zellen in Abhängigkeit ihrer verwendeten Deckglasdicke bestimmt. Es wurde herausgefunden, dass die maximale Leistung auf $87\,\%$ ihres ursprünglichen Wertes am Missionsende degradiert, wenn $100\,\mu$m dickes Deckglas verwendet wird.
Des Weiteren wurde herausgefunden, dass die Hellkennlinie von GaAs-Zellen einen spannungsabhängigen Photostrom zeigt. Die Ursache des Photostroms liegt in der spannungsabhängigen Dicke der Raumladungszone in Kombination mit einer stark verringerten Minoritätsladungsträgerdiffusionslänge und wurde auch dementsprechend modelliert. Das experimentelle Verhalten des Photostroms ist exakt nachgebildet worden unter Einbeziehung der Dicke der Raumladungszone, welche durch Kapazitätsmessungen herausgefunden wurde und der Basisschichtdiffusionslänge, welche durch Messungen der externen Quanteneffizienz bestimmt wurde.
Eine Methode der Bestimmung der Teilzellcharakteristiken von Mehrschichtsolarzellen unter Verwendung von gepulsten Lasern wurde vorgestellt und Charakteristiken von 3J- und 4J-Zellen wurden gemessen. Die Teilzellen von Mehrschichtzellen, speziell von bestrahlten Zellen, konnten somit direkt untersucht werden, was nicht möglich wäre mit etablierten Methoden, die das EL oder das PL Spektrum dazu benötigen. Die offene Klemmspannung als auch die Dunkelkennlinien aller Teilzellen sowohl von unbestrahlten als auch von mit Elektronen oder Protonen bestrahlten 3J- und 4J-Zellen wurden durch die Verwendung gepulster Laser bestimmt. Diese Charakterisierungsmethode macht die Notwendigkeit von Komponentenzellen überflüssig.

Contents

1 Introduction

Photovoltaics is the most promising technology for direct energy conversion from photons of the sun to electric power. The physics behind the solar cell began with the discovery of the photoelectric effect by Bequerel in 1839 [1]. He detected a voltage between two silver chloride-coated platinum electrodes in an electrolyte under illumination. The solar cell was finally made possible by the research into silicon p-n junctions carried out by Shockley, Bardeen, and Brittain in 1947 [2]. Shortly after the p-n junction was researched, the first modern silicon-based solar cell with an efficiency of $6\,\%$ was invented by Chapin, Pearson, and Fuller at the Bell laboratories in 1954 [3]. Ever since, researchers have tried to increase the efficiency of solar cells. With that goal in mind, different material systems were tried and their fabrication further developed since 1954, i.e. Ge, CdTe, CIGS, amorphous, poly- and single- crystalline Si, GaAs, InP, and organic materials. Moreover, different concepts such as quantum dot cells, concentrator cells, and multi-junction cells were developed to increase energy conversion efficiency. The evolution over time of the best research-cell efficiencies by cell material and technology is shown in Fig. 1.1. Multi-junction cells offer at the moment the highest efficiencies. The current record solar cell is a six-junction concentrator solar cell with an efficiency of $47.1\,\%$.

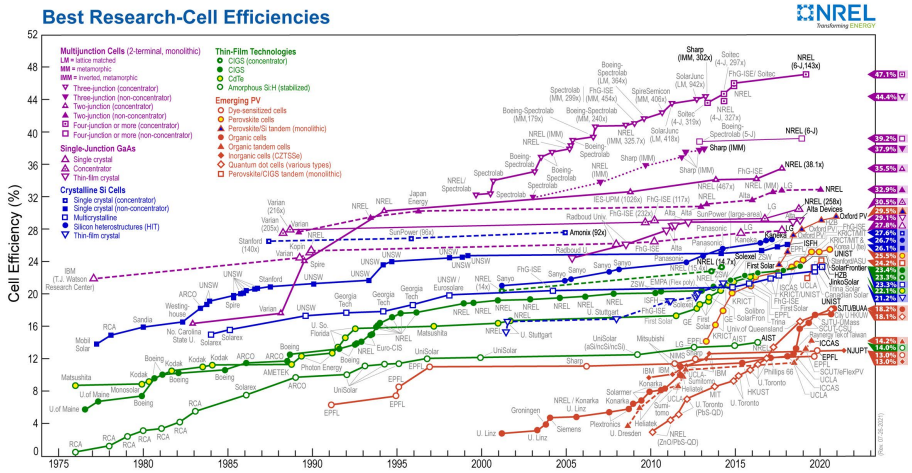

Figure 1.1 Table of best research-cell efficiencies from 2021. This plot is courtesy of the National Renewable Energy Laboratory, Golden, CO [4].

At the present time, solar cells are used as terrestrial energy source along with other energy sources, i.e. water power, wind power, fossil fuels, and nuclear power. In space, however, not many alternatives to photovoltaic energy exist.

Photovoltaic energy is the only energy source used to generate electric energy to power satellites in orbits around Earth or on exploration missions as far away as Jupiter.

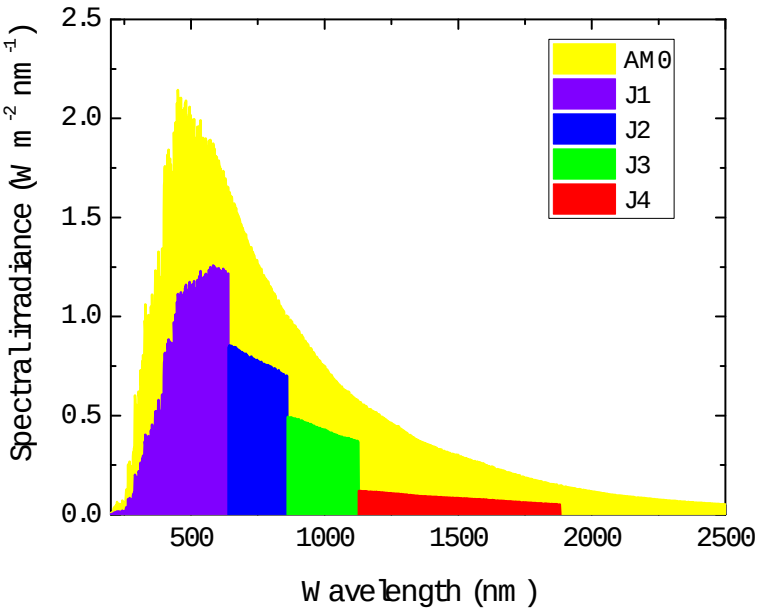

Figure 1.2 AM0 spectrum with the corresponding ratios convertible to electric power by 4J cells. The band gaps of the junctions J1 to J4 are $1.9\,\mathrm{eV}$, $1.4\,\mathrm{eV}$, $1.1\,\mathrm{eV}$, and $0.67\,\mathrm{eV}$.

Only on missions beyond Jupiter, the solar irradiance is too low to generate enough power for satellites. On such deep-space missions, satellites are powered by radioisotope thermoelectric generators. The first artificial satellite constructed by mankind was Sputnik, which was launched in 1957. It was powered only by batteries. Not long after this event, in 1958, the first satellite powered by solar cells called Vanguard 1 was launched. This event led to a worldwide increase in publicity for photovoltaic technology. The use of solar cells extended the maximum achievable satellite mission time. On Vanguard 1, six panels, each populated with eighteen $2 \times 0.5\,\mathrm{cm}^2$cells were mounted directly onto the hull of the satellite, which in sum generated a power of approximately $1\,\mathrm{W}$. The first satellite using fold-out solar panels was Explorer 6, which was equipped with four panels and an overall number of 9600 solar cells. Solar cells offer a very good power to mass ratio and are therefore the best choice to power satellites in the vicinity of the sun. The demand for solar cells in space was and still is the main driver of the development of solar cells with higher efficiencies. Up to approximately 1990, the bulk of the solar cells used in space was made of silicon. After 1990, GaAs-based solar cells began to replace

silicon. As shown in Fig. 1.1, the efficiencies of GaAs solar cells began to increase around 1990. GaAs-based cells showed higher efficiencies than silicon solar cells. While silicon solar cells in this day and age mainly play a role in terrestrial power generation due to their superior cost per watt ratio, they are not used in space anymore. The main solar cell technology deployed in space is multi-junction solar cells based on GaAs, which can use the spectrum of the sun more efficiently than single-junction cells. In Fig. 1.2, the AM0 spectrum, which is present outside of Earth's atmosphere, is depicted along with the maximum ratios of irradiance which can be converted to electric power by the four different junctions of a typical GaAs-based four-junction (4J) solar cell. The power per area of a junction can be computed by integrating the spectral irradiance of the junction with the wavelength. The image shows that a multijunction cell can use a larger proportion of the provided solar power when relying on material systems with band gaps adapted to the solar spectrum and when minimizing thermalization losses.

In Fig. 1.3, a present-day satellite wing consisting of four panels populated with multi-junction solar cells is shown. The panels have to be foldable due to the volume restrictions inside a rocket which transports a satellite into space. Once in space, the satellites solar generator unfolds and begins to generate power. Solar cells on satellites

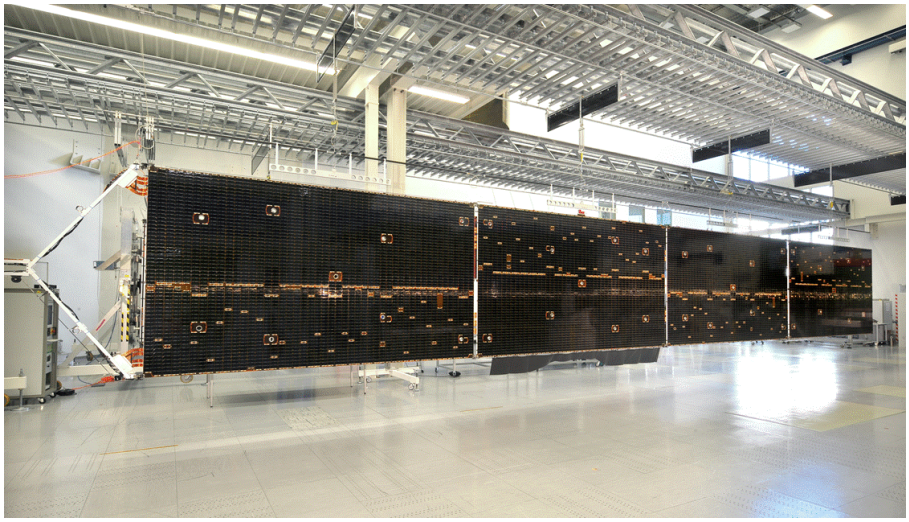

Figure 1.3 Solar generator wing used to power a satellite consisting of four panels populated with solar cells.

are exposed to extreme environmental loads, i.e. vibrations and acoustic noise during launch, temperature cycles due to eclipses, and also particle irradiation. The presence of charged particles in space around Earth was first proven by James Van Allen and his team, who designed and attached a Geiger counter on the satellite Explorer 1, which was launched in 1958. Data from Explorer 1 and Explorer 3 showed Van Allen that a belt consisting of charged particles existed around Earth. The particles trapped in the belt originate from solar wind, which is an omnidirectional stream of charged particles coming from the sun. Data from Pioneer 3 and Explorer 4 showed that there is an

outer radiation belt encircling the inner belt [5] [6]. Sergei Vernov was also a pioneer in researching the radiation belts around Earth [7]. These radiation belts are today known as the Van Allen belts. They mainly consist of electrons and protons trapped in Earth's magnetic field. The Van Allen belts are sketched in Fig. 1.4. In the center of

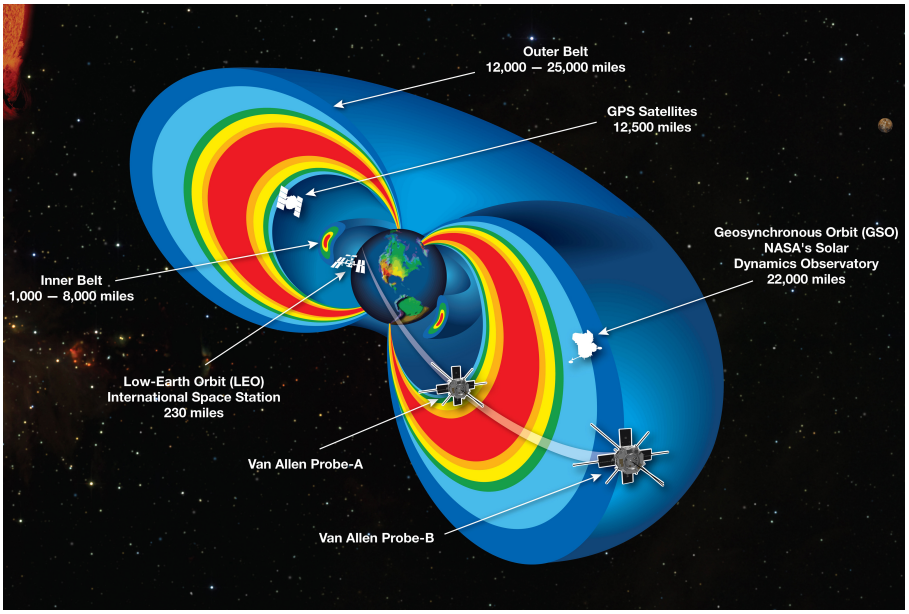

Figure 1.4 Cutaway model of the Van Allen radiation belts around earth. Credits: NASA [8].

the figure, Earth is depicted. Around Earth a cutaway model of the torus shaped inner and outer Van Allen belt is shown with red color indicating regions of high particle flux and blue regions indicating regions of lower particle flux. Within the belts sketches of some spacecrafts are shown along with their approximate orbits. Also the two Van Allen Probes are depicted, which were used by NASA to study the belts. Spacecrafts which transit these belts or operate in an orbit in a belt are exposed to high particle fluxes, which damage all materials, in particular semiconductors.

Therefore, there is a need for representative testing of the continuous particle spectrum on ground combined with an improved understanding of the degradation mechanism in order to develop cells with improved radiation hardness.

This thesis is structured in the following manner:

Chapters 2 and 3 First of all, the fundamentals of solar cell physics as well as the experimental setups used are explained.

Chapter 4 It is necessary to compute the non-ionizing damage which is caused by high-energetic charged particles in semiconductors. In this section, the computation of the non-ionizing energy loss of charged particles in matter is explained.

Chapter 5 In this section, a method to analyze degradation data gained from irradiation experiments is advanced. Typical degradation curves of 3J cells and their respective 1J subcells are determined with the help of this method.

Chapter 6 In this section, a new phenomenon, namely the voltage-dependent pho-

tocurrent of irradiated GaAs cells, is introduced. Its origin was researched and fully explained.

Chapter 7 In this section, the results of the irradiation of 4J cells and their respective 1J subcells and the following characterization and analysis are shown. Moreover, a power prediction of an electric-orbit-raising mission to a geostationary orbit until its end of life is presented depending on the employed cover glass thickness.

Chapter 8 In this section, a new method of determining the subcell characteristics of a multi-junction solar cell is introduced and the results of 3J and 4J cells are presented.

2 Fundamentals of space photovoltaics

In this chapter, the fundamentals of photovoltaics in space are introduced, with special attention to particle irradiation. Firstly, the theory of solar cells is given. Secondly, the particle environment in space and the theoretical aspects of defects in solar cells are explained.

2.1 Solar cell

2.1.1 pn-junction

In order to create a pn-junction, a semiconductor is doped with atoms of other elements. Atoms belonging to a main group with a higher atomic number than the semiconductor material are called donors because they donate electrons to the semiconductor. A semiconductor doped with donors is negatively doped or n-doped, which means there is an excess of free electrons, which are the majority charge carriers in an n-type semiconductor. Atoms belonging to a main group with a lower atomic number than the semiconductor material are called acceptors because they accept electrons or donate holes. A semiconductor doped with acceptors is positively doped or p-doped, which means there is an excess of free holes, which are the majority charge carriers in a p-type semiconductor. A pn-junction consists of a p-doped and an n-doped region in direct contact. A sketch of a pn-junction is shown in Fig. 2.1a).

In an n-doped semiconductor, the Fermi energy E_f is close to the conduction band energy E_c as shown in Fig. 2.1b). In a p-doped semiconductor, E_f is close to the valence band energy E_v. When the two doped semiconductors are brought into contact, the Fermi energy remains flat. This causes majority electrons from the n-region to move to the p-region and majority holes to move from the p- to the n-region until a thermal equilibrium is established. In thermal equilibrium, the bands are bent as sketched in Fig. 2.1b). The potential difference between the n- and the p-doped regions is called the built-in potential or built-in voltage V_b, see Eq. 2.1. The built-in voltage

$$V_b = \frac{k_B T}{e} \left(ln \left(\frac{N_D N_A}{n_i} \right) \right) \tag{2.1}$$

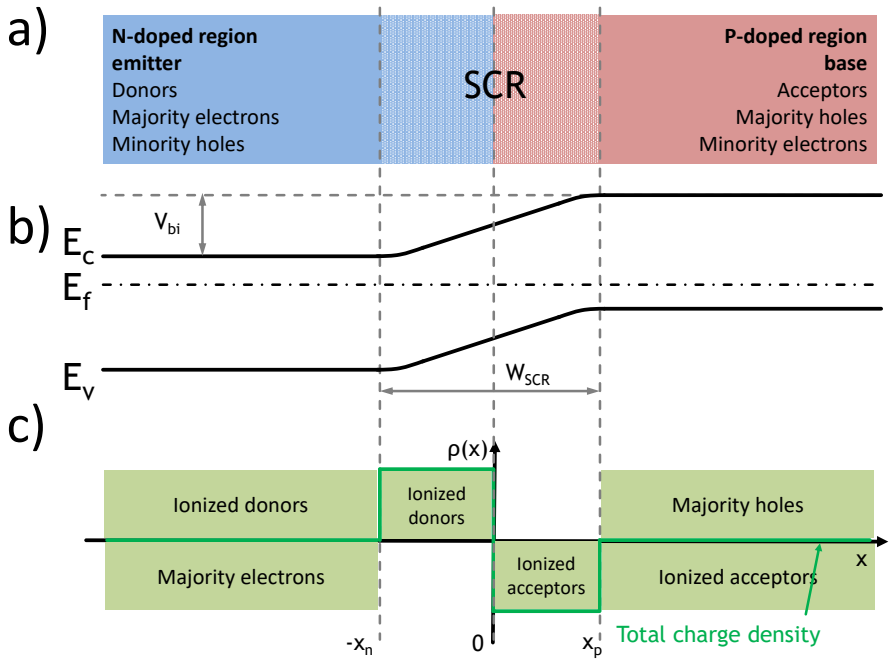

Figure 2.1 a) Sketch of a pn-junction b) Band diagram of a pn-junction c) Charge distribution of a pn-junction

is dependent on the temperature T, the donor doping density N_D, the acceptor doping density N_A, and the intrinsic carrier density n_i [9].

Around the contact region where the bands are bent, excess electrons and holes electrically neutralize each other. The remaining dopant atoms create a net positive resp. negative charge as sketched in Fig. 2.1c). Therefore, this region is called the depletion layer or space charge region (SCR). The total width of the SCR is W_{SCR}. The regions outside of the SCR are electrically neutral because dopant atoms and their excess charge carriers neutralize each other's charges. The width of the SCR W_{SCR} is given in Eq. 2.2. It is

$$W_{SCR} = \sqrt{\frac{2\epsilon_0\epsilon_r}{e}\frac{N_A + N_D}{N_A N_D}V_b} \tag{2.2}$$

is dependent on the permittivity $\epsilon_0\epsilon_r$, the donor doping density N_D, the acceptor doping density N_A and the built-in voltage V_b [9].

Within the SCR, an electrical field spreads from the positively to the negatively charged region. This is in principle the structure of a plate capacitor. Therefore, there is a capacitance, the so-called depletion-layer capacitance:

$$C = \frac{dQ}{dV} = \sqrt{\frac{e\epsilon_0\epsilon_r N_{D/A}}{2(V_b \pm V - \frac{2k_B T}{e})}} \tag{2.3}$$

By applying a voltage dV to the pn-junction and changing it incrementally, the charge per unit area dQ at the depletion layer changes incrementally as well. The capacitance of

the depletion layer depends on the permittivity $\epsilon_0\epsilon_r$, the doping density N_A if $N_D >> N_A$, and vice versa, the built-in voltage V_b, the applied voltage V, and $\frac{2k_BT}{e}$, which is a correction factor introduced because the charge distribution within the SCR is not exactly rectangular as sketched in Fig. 2.1c), but the majority-carrier distribution introduces tails to the distribution [9].

In a solar cell, the n-doped part of the semiconductor, which is thinner, higher doped, and facing to the sun, is called emitter, and the p-doped part of the semiconductor, which is thicker, lower doped, and facing away from the sun, is called base. Therefore, this terminology is also applied in the following. When a voltage is applied to the base and emitter, the width of the SCR changes depending on the polarity of the voltage. When the applied voltage increases the width, the pn-junction is operated in backwards direction and only a small backwards current can flow. Changing the polarity of the applied voltage will allow an exponentially growing current to flow through the pn-junction, which is then operated in forward direction.

Two regions have to be discriminated regarding the recombination of electrons and holes in order to fully describe the recombination behavior. Firstly, there is the recombination in the base and emitter region. Secondly, there is the recombination in the SCR. The current-voltage characteristics of an ideal pn-junction are described by the Shockley equation 2.4, which neglects recombination in the SCR. This equation is based on four assumptions [9]: 1) the abrupt SCR approximation, which states that an abrupt change occurs between the SCR and neutral regions 2) the Boltzmann relations are valid within the SCR 3) minority carrier densities are small compared to the majority carrier densities 4) no generation current exists in the depletion layer. This leads to the Shockley equation

$$I_1 = I_{01}(\exp\frac{eV}{k_BT} - 1) \tag{2.4}$$

where I_{01} describes the recombination of electrons and holes in the neutral base and emitter regions.

$$I_{01} = I_p + I_n = e(\frac{D_p p_{n0}}{L_p} + \frac{D_n n_{p0}}{L_n}) \tag{2.5}$$

I_p and I_n are the hole and electron recombination currents, D_p and D_n are diffusion coefficients, p_{n0} and n_{p0} are the equilibrium hole resp. electron densities in the n- and p-region and L_p and L_n are the diffusion lengths. In an asymmetrically doped solar cell, either I_p or I_n dominates and the other one can be neglected due to different doping densities of the n- and p-region.

The ideal Shockley equation describes the behavior of pn-junctions based on some semiconductor materials well. However, e.g. for GaAs-based pn-junctions, the generation and recombination process in the SCR has to be considered as well, which is neglected

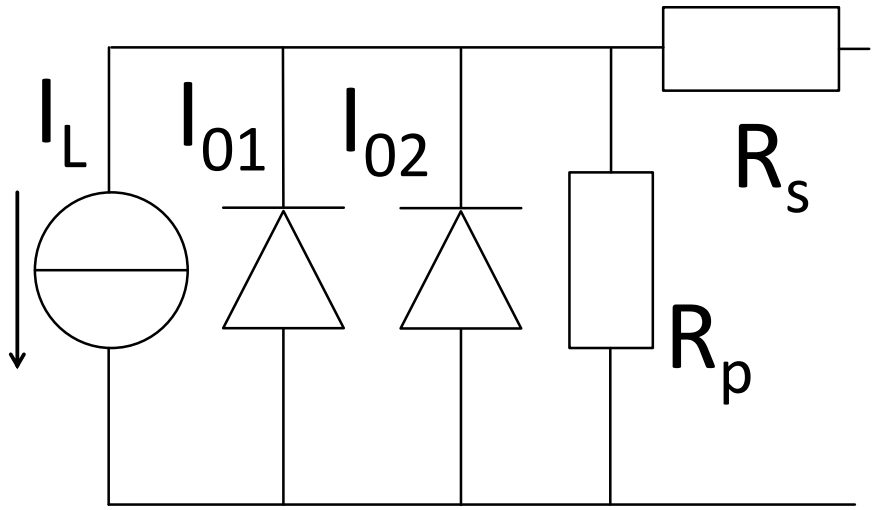

Figure 2.2 Equivalent circuit of an 1J solar cell.

in the Shockley equation. The recombination current in the depletion region is given by Eq. 2.6

$$I_2 = I_{02}(\exp \frac{eV}{2k_BT} - 1) \tag{2.6}$$

where I_{02} describes the recombination of electrons and holes in the SCR. It is important to note that the so-called ideality factor is 2 in the denominator of the exponential function of Eq. 2.6 in contrast to 1 in Eq. 2.4.

$$I_{02} = \frac{eW_{SCR}\sigma_{p/n}v_{th}N_tn_i}{2} = \frac{eW_{SCR}n_i}{\tau_{p/n}2} \tag{2.7}$$

W_{SCR} is the thickness of the SCR, σ is the capture cross section of an assumed trap in the middle of the bandgap with energy $E_g = \frac{E_c - E_v}{2}$ and density N_t, thermal carrier velocity v_{th}, and lifetime $\tau_{p/n}$ [9].

2.1.2 Real solar cell

In a real solar cell, both recombination currents I_1 and I_2 have to be considered. Moreover, series and parallel resistance R_s and R_p are responsible for losses. The equivalent circuit diagram of a single-junction solar cell is depicted in Fig. 2.2. It consists of two diodes, a current source, and a shunt resistor connected in parallel as well as a resistor connected in series. The two diodes represent two recombination currents I_1 and I_2. The current source represents the current generated in the solar cell under illumination. The resistors represent resistances present in the solar cell itself.

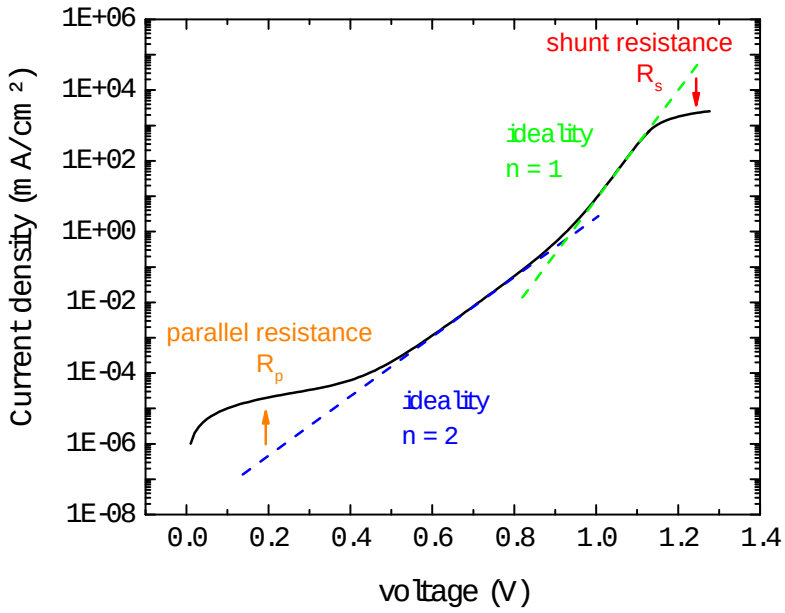

Figure 2.3 Typical current-voltage characteristics of a GaAs pn-junction in forward direction.

A single-junction solar cell without illumination can be described by the two-diode-model Eq. 2.8

$$I_{dark} = I_{01}(\exp\frac{e(V-IR_s)}{k_BT} - 1) + I_{02}(\exp\frac{e(V-IR_s)}{2k_BT} - 1) + \frac{V-IR_s}{R_p} \tag{2.8}$$

A typical current-voltage measurement of a single-junction solar cell without illumination is depicted in Fig. 2.3. The curve is dominated by four different parameters depending on the applied voltage range. At the lowest voltage range, the characteristic dark current-voltage curve shows an increased current density due to the parallel resistance R_p of the cell. Next, the curve shows an exponential increase, which is dominated by the recombination current I_2. This means that most of the recombination takes place in the space-charge region. At higher voltages, the recombination in the emitter and base regions increases so that the overall cell current is dominated by this kind of recombination current, which is represented by I_1. At the highest applied voltages possible without permanently damaging the solar cell, the behavior is dominated by the series resistance of the cell, which reflects the resistance of the contact metalization and the semiconductor shunt resistance.

$$I = I_{dark} - I_L \tag{2.9}$$

The current voltage characteristics of a solar cell under illumination is described by Eq. 2.9. The equation represents the superposition of the two-diode-model recombination current and the photocurrent I_L [10]. A typical IV-curve under illumination is depicted

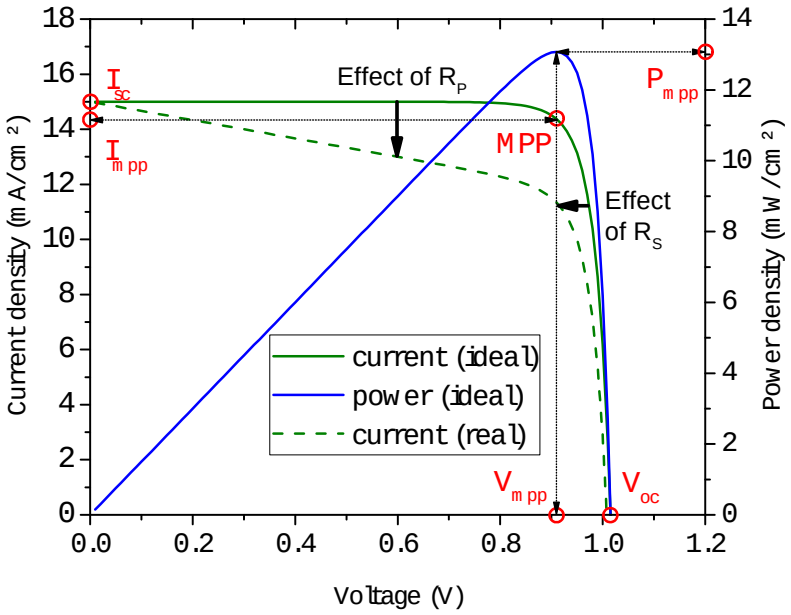

Figure 2.4 Typical current-voltage and power-voltage characteristics of a solar cell under illumination.

in Fig. 2.4. It is important to note that the LIV-curve is depicted in its typical notation, which consists of a linear current axis in contrast to the logarithmic current axis of the DIV curve. Moreover, the current axis is inverted, which is the reason why the current I_L is positive while Eq. 2.9 states a negative photocurrent. The important electrical parameters of a solar cell IV-curve under illumination are highlighted in the graph: The short-circuit current I_{sc}, which is the maximum current a real solar cell can generate, the current at maximum power point I_{mpp}, the maximum power P_{mpp}, the voltage at maximum power point V_{mpp}, and the open-circuit voltage V_{oc}. The maximum power point MPP can be easily determined by plotting the power-voltage curve of the solar cell, which is shown as the blue graph. It is computed by simple multiplication $P(V) = V \cdot I(V)$. In a real solar cell measured, a series resistance R_s and a shunt resistance R_p can appear. In the IV-curve, a shunt resistance would result in a slope of the otherwise horizontal current branch of the curve from approximately $V = 0$ to $V = V_{mpp}$. A series resistance would result in a less steep slope of the current branch from approximately $V = V_{mpp}$ to $V = V_{oc}$. A real IV-curve including R_s and R_p is shown as dashed line in Fig. 2.4.

The power at maximum power point can be computed using Eq. 2.10

$$P_{mpp} = I_{mpp} \cdot V_{mpp} \tag{2.10}$$

The fill factor of a solar cell describes the squareness of the LIV curve and is given by Eq. 2.11.

$$FF = \frac{P_{mpp}}{I_{sc} \cdot V_{oc}} \tag{2.11}$$

The spectral response (SR) of a solar cell is the ratio of the current generated by a solar cell to the power incident to the solar cell wavelength dependent. The SR is necessary to calculate the maximum photocurrent, a solar cell can generate I_{Lmax}. The I_{Lmax} is determined by the incoming photon flux, the band gap of the solar cell, and the average number of electron-hole pairs generated per incoming photon. The maximum photocurrent is described by Eq. 2.12, which is the integral from the wavelengths starting from 0 to the bandgap wavelength λ_g over the product of the spectral response SR(λ) and the photon spectrum outside of Earth's atmosphere AM0(λ), which stands for air mass zero.

$$I_{Lmax} = \int_0^{\lambda_g} SR(\lambda) \cdot AM0(\lambda) d\lambda \tag{2.12}$$

The bandgap wavelength λ_g can be calculated using Eq. 2.13. The higher the band gap, the fewer photons contribute to the photocurrent, but the generated voltage is higher.

$$E_g = \frac{hc}{\lambda_g} \tag{2.13}$$

The spectral response SR of a solar cell correlates with the external quantum efficiency EQE, which states the average number of electron-hole pairs generated per incoming photon, by Eq. 2.14.

$$EQE = \frac{n_e}{n_{ph}} = \frac{\frac{It}{e}}{\frac{Pt\lambda}{hc}} = \frac{hc}{e\lambda} SR \tag{2.14}$$

The EQE should be close to 1 for an efficient solar cell. In Fig. 2.5, the SR and EQE of a J1 cell of a 4J cell are depicted. At approximately $650\,\text{nm}$, both values are zero, which means that this is approximately the bandgap wavelength of J1.

2.1.3 Multi-junction solar cell

Solar cells can only use the energy of photons up to the bandgap of the semiconductor. The additional energy of higher energetic photons is lost. These thermalization losses can be minimized by using multi-junction instead of single-junction solar cells. In a multi-junction cell, more than one solar cell are connected in series on top of each other. This can be achieved by different approaches, such as epitaxial growth from bottom to top on a substrate, epitaxial growth from top to bottom, and a final lift-off step to get rid of the substrate or wafer bonding of two independently grown parts of a multi-junction cell. As an example, a detailed layered sketch of a 3J cell is shown in Fig. 2.6. To connect different subcells in a multi-junction cell, tunnel diodes are used.

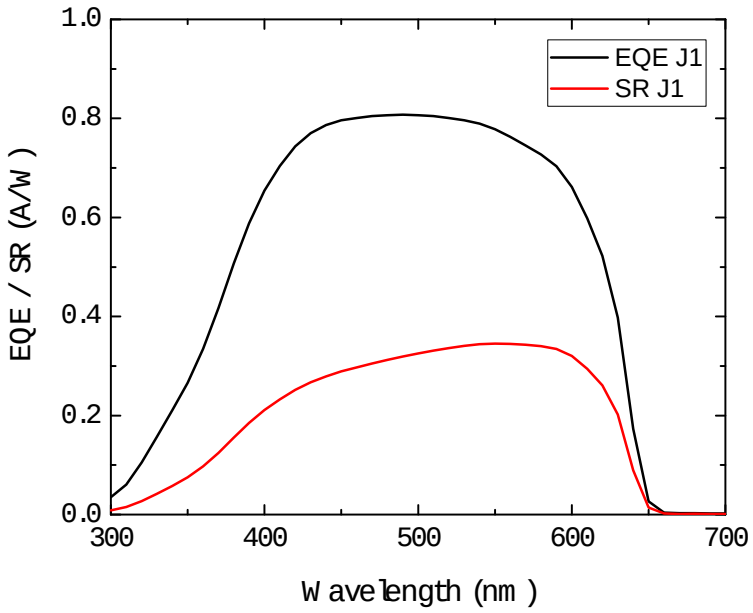

Figure 2.5 External quantum efficiency and spectral response of a J1 subcell.

Otherwise i.e. the n-contact of the bottom cell and the p-contact of the middle cell would form a diode in reverse direction and no current could flow through the 3J cell. Tunnel diodes are pn-junctions which are heavily doped, which leads to degeneration of both the p- and the n-side. This means that the Fermi energy E_f lies below E_v at the p-side and above E_c on the n-side. Applying reverse voltage to the junction will bend the bands in a way that direct tunneling from charge carriers from the valence band to the conduction band becomes possible. Above the top cell, there is a window layer. High-energy photons are absorbed close to the surface and the window layer is necessary to prevent surface recombination. It consists of a high band gap material ensuring that it is transparent for the wavelengths absorbable by the three cells below. The top of the window layer is covered by an anti-reflection coating (ARC) made from TiO_x/Al_2O_3 as well as by the metal grid fingers. The bottom of the cell is fully metalized. Due to the connection in series of several subcells, the overall current of a multi-junction cell is determined by the lowest current of all subcells:

$$I_{MJ} = min(I_n) \tag{2.15}$$

The voltage of a multi-junction cell is the sum of the individually generated voltages:

$$V_{MJ} = \sum V_n \tag{2.16}$$

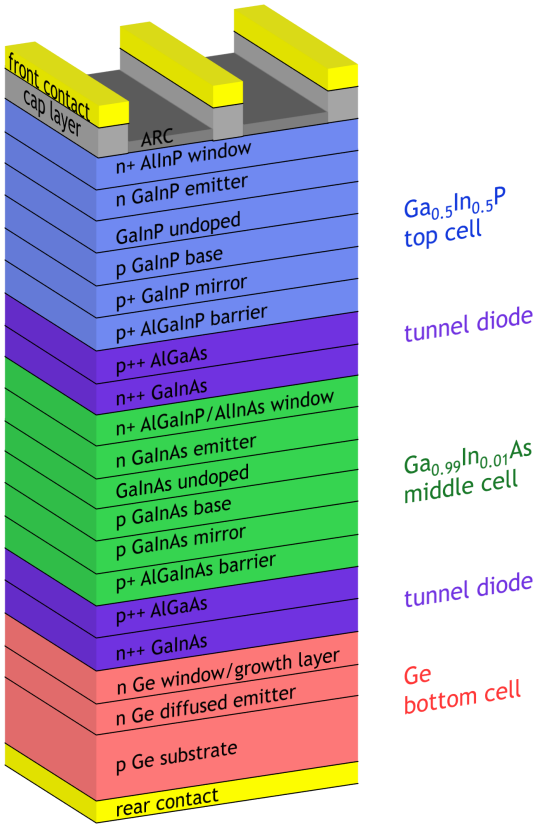

Figure 2.6 Sketch showing the layer structure of a 3J cell. Typical layers according to [11].

2.2 Generation and recombination

2.2.1 Generation

In a solar cell, electron-hole pairs are generated by the absorption of photons γ. To deduce the distribution of a photon current j_γ incoming on a semi-infinite semiconductor, the continuity equation given by Eq. 2.17 is used.

$$\frac{\partial n_\gamma(x)}{\partial t} = G_\gamma(x) - R_\gamma(x) - \frac{\partial j_\gamma(x)}{\partial x} \tag{2.17}$$

It means that the density n_γ of photons in a volume element at location x changes over time by considering the generation rate G_γ of photons as well as the recombination rate R_γ and the incoming or outgoing photon current j_γ. We only consider the static case marked by no change over time ($\frac{\partial n_\gamma(x)}{\partial t} = 0$). We assume that no photons are created in the semiconductor. (G_γ=0, radiative recombination is neglected). The recombination rate inside the semiconductor is assumed to be proportional to the incident photon current ($R_\gamma = \alpha j_\gamma$) with the absorption coefficient α to be determined later in this section. These conditions lead to Eq. 2.18, which is the continuity equation for photons in a semiconductor:

$$div\, j_\gamma(x) = -\alpha j_\gamma(x) \tag{2.18}$$

The solution to this differential equation is Eq. 2.19

$$j_\gamma(x) = j_\gamma(0) \exp(-\alpha x) \tag{2.19}$$

which is also called the Lambert-Beer-law. $j_\gamma(0)$ is the photon current which is not transmitted or reflected but absorbed at the surface of the semiconductor. The most important process in a solar cell is the creation of electron-hole pairs by absorption of photons. The probability of a photon with energy E_γ being absorbed in a semiconductor is determined by the absorption coefficient $\alpha(E_\gamma)$ of a semiconductor.

Direct bandgap

The generation of electron-hole pairs can occur via a direct or an indirect bandgap of a semiconductor. Direct transitions are defined as transitions of electrons and holes between the valence band energy E_v and the conduction band energy E_c where the momentum of the electron-hole system does not change, because the momentum brought into the system by the photon is negligible. When a photon γ is absorbed and creates an electron e and a hole h as it is shown in Eq. 2.20,

$$\gamma \rightarrow e + h \tag{2.20}$$

the absorption coefficient α can be computed using momentum and energy conservation [12]. α depends on the energy of the photon, see Eq. 2.21.

$$\begin{aligned} \alpha &= 0 \text{ for } E_\gamma < E_g \\ \alpha &\propto \sqrt{E_\gamma - E_g} \text{ for } E_\gamma > E_g \end{aligned} \tag{2.21}$$

For photon energies below the bandgap energy, the photons cannot be absorbed because inside the bandgap there are no allowed states for electrons and holes. For photon energies above the bandgap energy, the absorption edge of direct bandgap semiconductors like GaAs increases abruptly. At $x = \frac{1}{\alpha}$, the intensity of the photon current has decreased by the factor e. The corresponding length $L_\gamma = \frac{1}{\alpha}$ is called penetration depth. Due to the high absorption coefficient α of semiconductors with direct bandgaps, the thickness of solar cells grown from direct bandgap materials can be very thin within an order of magnitude of $1\,\mu$m.

Indirect bandgap

In indirect semiconductors, the transition of electrons and holes between the valence band and the conduction band is not possible only by photon absorption at the minimum bandgap energy. The momentum conservation is only fulfilled by bringing in the

momentum of another particle, which is a lattice vibration or phonon Γ as shown in Eq. 2.22.

$$\begin{aligned} \gamma + \Gamma &\rightarrow e + h \\ \gamma &\rightarrow e + h + \Gamma \end{aligned} \tag{2.22}$$

The additional momentum of the phonon enables transitions between the valence and the conduction band with different momentum values. The absorption coefficient α is

$$\begin{aligned} \alpha &\propto (E_\gamma - E_g + E_\Gamma)^2 \text{ for phonon absorption} \\ \alpha &\propto (E_\gamma - E_g - E_\Gamma)^2 \text{ for phonon emission} \end{aligned} \tag{2.23}$$

Due to the necessity of phonon participation, the probability of indirect transitions is small compared to direct transitions. This causes an increase of the absorption edge, which is less steep than of the absorption edge of direct transitions, and furthermore a longer penetration depth. Typical indirect bandgap semiconductors are silicon and germanium. Si and Ge solar cells have to be thicker than direct bandgap solar cells in order to absorb the same amount of photons. Their thickness has an order of magnitude of $10 - 100\,\mu$m

2.2.2 Recombination

Recombination describes the annihilation of electron hole pairs. Therefore, this process involves the transition of electrons resp. holes between valence and conduction band. The involved energy is released resp. provided as thermal energy or as photons. Recombination can be triggered by external excitation, which generates excess charge carriers within the system. When the external excitation stops, the system returns to its initial state. The excess charge carrier concentration decreases according to the recombination rate R, which is dependent on the kind of recombination. There are different kinds of recombination processes. Intrinsic recombination like radiative band-to-band recombination and Auger recombination can occur even in defect-free semiconductors. Other recombination processes involve defects in the bandgap or defects at the surface. The overall recombination rate is a sum of all individual recombination rates.

Radiative recombination

The radiative recombination of an electron and a hole is the opposite process of the direct absorption of a photon.

$$e + h \rightarrow \gamma \tag{2.24}$$

In the pure view of electrons this means the transition of an electron from the conduction band to the valence band thus creating a photon so the energy conservation is

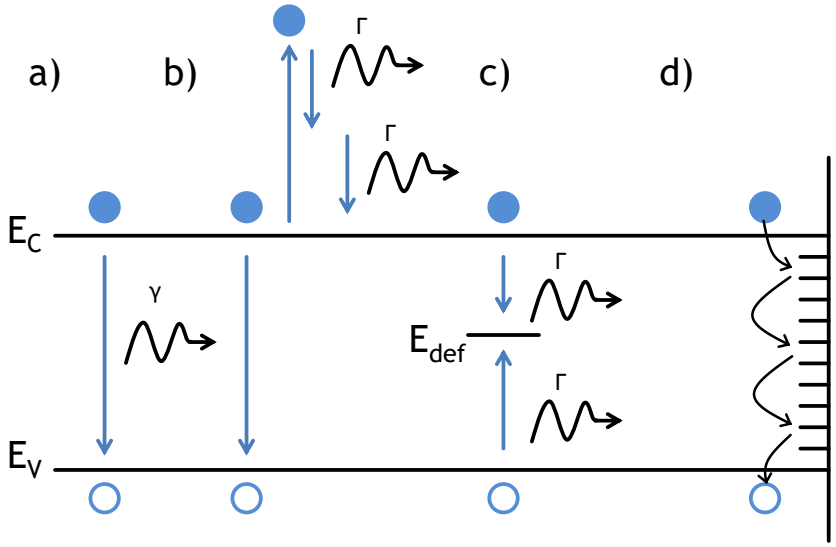

Figure 2.7 Electrons and holes can recombine a) radiatively by emitting a photon γ, b) by Auger recombination where the released energy is absorbed by an electron in the conduction band, which then thermalizes to its original energy level generating phonons Γ c) non-radiatively at a defect in the band gap by emitting phonons Γ and d) at the continously distributed defect states of a surface.

fulfilled, which is shown in Fig. 2.7a). Radiative recombination is negligible in indirect semiconductors but pronounced in direct semiconductors.

$$R_{rad} = Bn_e n_h \tag{2.25}$$

The radiative recombination rate R_{rad}, see Eq. 2.25 is dependent on the densities of free electrons n_e and free holes n_h as well as the material dependent coeffiecient B [12].

Auger recombination

Auger recombination is also the transition of an electron from the conduction band to the valence band, but it is a non-radiative kind of recombination. The released energy is absorbed by another electron in the conduction band (eeh-process) or by a hole in the valence band (ehh-process). The electron resp. hole which absorbed the recombination energy releases this additional energy to the crystal lattice in the form of phonons. The eeh-process is sketched in Fig. 2.7b).

$$R_{Aug} = n_e n_h (C_e n_e + C_h n_h) \tag{2.26}$$

The Auger recombination rate R_{Aug} is given by Eq. 2.26, which includes Auger recombination of both electrons and holes and their respective Auger coefficients C_e and

C_h. The dominant kind of Auger recombination is dependent on the semiconductor being n- or p-doped. Auger recombination in general is dominant in heavily doped semiconductors [12].

Shockley-Read-Hall recombination

Recombination through defects in the semiconductor bandgap (deep-level impurities or traps) is called Shockley-Read-Hall (SRH) recombination. The released energy during recombination dissipates by phonons or lattice vibrations. Therefore, it is a non-radiative kind of recombination. In solar cells, especially in the ones containing defects by particle irradiation, this is the dominant recombination process. Most important are defects with a defect energy in the middle of the bandgap. Recombination of an electron and a hole caused by a defect is also called electron-hole capture. It is shown in Fig. 2.7c).

$$R_{SRH} = \frac{n_e n_h - n_i^2}{\tau_h(n_e + \beta_e) + \tau_e(n_h + \beta_h)} \tag{2.27}$$

The recombination rate R_{SRH} is described by Eq. 2.27. It is dependent on the free carrier densities n_e and n_h as well as the intrinsic carrier density n_i, the average lifetime of a hole resp. an electron τ_h and τ_e and the emission coefficients of electrons from the defect into the conduction band β_e and of holes into the valence band β_h.

$$\begin{aligned} \tau_h &= \frac{1}{N_{def}\sigma_{h,def}}\nu_h \\ \tau_e &= \frac{1}{N_{def}\sigma_{e,def}}\nu_e \end{aligned} \tag{2.28}$$

The lifetimes are given by Eq. 2.28, where N_{def} is the density of defects in the semiconductor, $\sigma_{h/e,def}$ is the capture cross section of the defect regarding holes or electrons, and $\nu_{h/e}$ is the average carrier velocity. Different kinds of defects can capture either holes or electrons more efficiently.

$$\begin{aligned} \beta_h &= N_V \exp\frac{E_v - E_{def}}{k_B T} \\ \beta_e &= N_C \exp\frac{E_{def} - E_c}{k_B T} \end{aligned} \tag{2.29}$$

The emission coefficients β_h resp. β_e for captured holes resp. electrons into the conduction resp. valence band is given by Eq. 2.29. N_V and N_C are the effective density of states in the valence band resp. conduction band. E_{def} is the defect energy within the band gap [12].

Surface recombination

Recombination on surfaces of semiconductors is also a kind of non-radiative recombination. Defects existing on surfaces like dangling bonds provide continuous surface states where electrons and holes can recombine. In the picture of the band diagram, the bandgap is bypassed by the surface states, which is sketched in Fig. 2.7d).

$$R_{sur} = \nu_{e,sur} n_e + \nu_{h,sur} n_h \tag{2.30}$$

The surface recombination rate is given by Eq. 2.30. $\nu_{e,sur}$ and $\nu_{h,sur}$ are the surface recombination velocities which are characteristic for the surface [12]. To suppress surface recombination, surfaces of semiconductors are typically passivated.

2.3 Radiation induced defects

In real semiconductors, crystal defects are unavoidable. The intrinsic density of defects depends strongly on the manufacturing process and is typically well optimized. For applications of semiconductor devices in particle radiation environments, however, radiation induced defects accumulate over time. They influence the parameters of semiconductor devices. Defects are generated when energetic particles collide with crystal atoms. These collision or scattering events can be described by two kinds of scattering. Firstly, there is elastic scattering, which describes scattering events where the energy of the scattering particles is conserved. Secondly, there is inelastic scattering, which describes scattering events where the energy is lost or gained by additional processes such as nuclear fission. Considering that the radiation environment in space consists mostly of electrons and protons in an energy range where nuclear reactions are negligible, elastic scattering is the dominant scattering process in space for solar cells.
An incoming particle is called primary particle. The first atom of the crystal lattice the primary particle collides with is called primary knock-on atom (PKA). For the PKA and every other lattice atom to be displaced from its lattice site, a certain amount of energy is necessary, which is called the threshold energy for atomic displacement T_d. The primary particle or the PKA itself can collide with other lattice atoms causing a cascade of recoils. The total number of displaced atoms is described by the Kinchin-Pease model [13] and improved by Norgett et al. [14]. It states that the number of

displaced atoms N_d increases linearly with the energy of the PKA T_{PKA} as long as its energy is below the energy of the primary particle T_{pp} and above $\frac{2T_d}{0.8}$.

$$N_d = \begin{cases} 0 & \text{for } T_{PKA} < T_d \\ 1 & \text{for } T_d < T_{PKA} < \frac{2T_d}{0.8} \\ \frac{0.8T_{PKA}}{2T_d} & \text{for } \frac{2T_d}{0.8} < T_{PKA} < T_{pp} \end{cases} \tag{2.31}$$

The displaced atoms resp. the displacement sites form different defects with different properties. There are many different defect types occurring in semiconductors. Typical defects are

- Vacancy
  A vacancy is a point defect in an atomic site where one lattice atom is missing. A defect where two adjacent atoms are missing from the lattice is called divacancy.
- Interstitial
  An interstitial is a point defect where an atom occupies an interstitial site between surrounding atoms at normal sites.
- Frenkel defect
  A Frenkel defect or Frenkel pair is a combination of two defects. It consists of an atom leaving its normal site and coming to rest in an interstitial site. Therefore, a Frenkel pair is a vacancy-interstitial pair.
- Antisite defect
  An antisite defect is only possible in a crystal consisting of at least two different elements, i.e. A and B. An atom of type A resting at a site of an atom of type B is called an antisite defect.
- Substitute
  A substitute defect exists when an impurity atom is at the site of a crystal atom. Typical desired substitute defects are doping atoms. Undesired substitute defects are typically caused by contamination in the manufacturing process.
- Complex
  Combinations of different defects are called complexes and can show different properties than the single defects the complex consists of.

Some of the described defects are exemplarily depicted in Fig. 2.8 in a GaAs lattice.

The most important impact of radiation damage in semiconductors is the decrease of minority carrier lifetime τ and the minority carrier diffusion length L as described by Eqs. 2.32 and 2.33

$$\frac{1}{\tau} = \frac{1}{\tau_0} + K_\tau \Phi \tag{2.32}$$

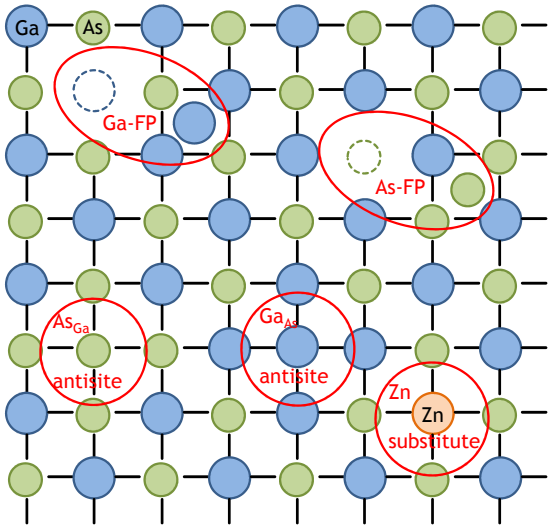

Figure 2.8 A sketch of a GaAs lattice is shown with the bigger blue circles being gallium and the smaller green circles being arsenide. A gallium Frenkel-pair is shown as well as an arsenide Frenkel pair, an As_{Ga} and a Ga_{As} antisite defect and a Zn_{Ga} substitute defect.

$$\frac{1}{L^2} = \frac{1}{L_0^2} + K_L \Phi \tag{2.33}$$

The initial values of minority carrier lifetime and diffusion length are τ_0 and L_0. The incoming particle fluence per area is Φ. The lifetime damage constant is K_τ and the diffusion length damage constant is K_L. The damage constants depend on particle type, particle energy, and semiconductor type. Lifetime and diffusion length affect the probabilities of an electron-hole pair to reach the SCR, of being collected, or of recombining.

2.4 Degradation analysis of solar cell parameters

The space environment causes degradation of solar cell parameters, i.e. open-circuit voltage, short-circuit current, and power at maximum power point. To provide sufficient power over the lifetime of a satellite, it is necessary to accurately predict the degradation of the cell parameters. In order to accomplish this, the particle environment in space is simulated by irradiating solar cells on earth with particles provided by particle accelerators. The continuous energy range which prevails in space cannot be directly tested on Earth since accelerators provide monoenergetic particle beams in a limited energy range. Therefore, it is necessary to correlate the limited test data from monoenergetic irradiation with the expected environment in space. Two methods are

of importance. The JPL method is explained in the following subchapter. The NRL method, which is used in this thesis, is described in detail in chapter 5.

2.4.1 Equivalent fluence method

The original method was developed at the JPL (Jet Propulsion Laboratory) and is referred to as the JPL method or equivalent fluence method. To determine the equivalent fluence curve of a solar cell technology, the first step is to measure a large set of degradation data for both electrons and protons. Such a data set can be found for GaAs/Ge cells in the GaAs Solar Cell Radiation Handbook [15]. Four electron energies and eight proton energies with eight fluences for each energy were measured. From this data, relative damage coefficients (RDCs) are determined by relating the fluence of a certain electron energy to the fluence of $1\,\text{MeV}$ electrons, which cause a certain degradation (i.e. $75\,\%$). For protons, the energy for the relation is typically $10\,\text{MeV}$. The proton RDCs can be related to electron RDCs by using a proton to electron damage equivalency ratio, which converts $10\,\text{MeV}$ proton to $1\,\text{MeV}$ electron fluence. The experimentally determined RDCs are then multiplied with the expected spectrum in orbit and integrated over all energies to get an equivalent $1\,\text{MeV}$ electron fluence $\phi_{1\,\text{MeV electron equivalent}}$, which represents the whole radiation level of a mission as given by Eq. 2.34.

$$\phi_{1\,\text{MeV electron equivalent}} = \int \frac{d\phi_e(E)}{dE} RDC_e(E)dE + R_{pe} \int \frac{d\phi_p(E)}{dE} \cdot RDC_p(E)dE \quad (2.34)$$

The remaining factors (i.e. of current, voltage, or power) of all tested cells can then be plotted against the equivalent $1\,\text{MeV}$ electron fluences determined in this way. The resulting data points show the degradation of this parameter. The degradation of the cell parameters can be fitted with the semi-empirical equation 2.35.

$$RF = 1 - C_\phi \cdot log(1 + \frac{\phi}{\phi_{crit}}) \quad (2.35)$$

RF is the remaining factor of the cell parameter under investigation, i.e. $\frac{I_{sc}(irradiated)}{I_{sc}(beginoflife)}$. C_ϕ and ϕ_{crit} are the fitting parameters of this equation representing the slope of the decrease of the cell parameter with increasing fluence and the approximate fluence where the majority of the decrease begins. The expected degradation of solar cells after the mission can then be read off the $1\,\text{MeV}$ electron degradation curve. A big disadvantage of the JPL method is the large amount of irradiation data needed to characterize the degradation behavior of each new cell technology, which requires a large data set.

3 Experimental details

In this chapter, the details of the tested samples and of the experimental setups used in this work will be explained. Firstly, the solar cells used for characterization and irradiation will be described. Secondly, the details of the particle irradiation and irradiation facilities will be explained. Thirdly, the cell characterization setups will be described in detail. The cells are characterized by current-voltage measurement under the AM0 spectrum (LIV), dark current voltage measurement (DIV), capacitance-voltage measurements (CV), external quantum efficiency (EQE) measurements, and pulsed laser measurements.

3.1 Solar cell samples

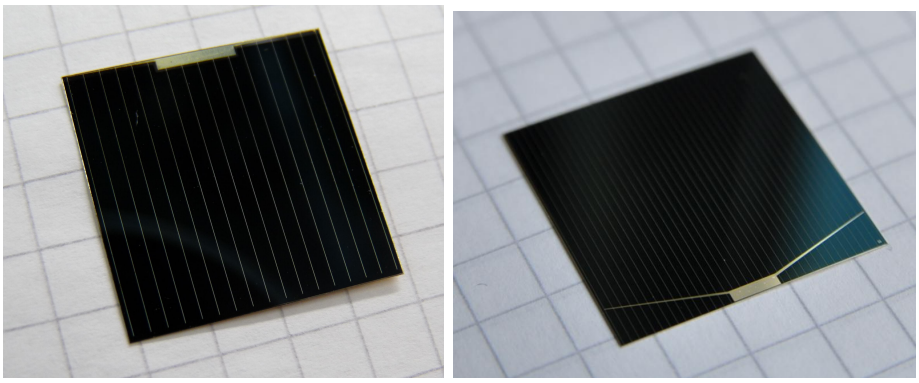

(a) 3G30 cell front side (b) 4G32 cell front side

Figure 3.1 Exemplary images of the experimental solar cells with size of $2 \cdot 2\,\mathrm{cm}^2$ used in this thesis.

To analyze and characterize the influence of particle irradiation on 3G30 and 4G32 multi-junction and isotype solar cells, 136 3G30 3J cells, 34 3G30 top cells, 34 3G30 middle cells, 34 3G30 bottom cells, 112 4G32 4J cells, 56 4G32 J1 cells, 56 4G32 J2 cells, 56 4G32 J3 cells, and 56 4G32 J4 cells are irradiated with electrons and protons with different energies and fluences. Exemplary images of the cells are shown in Fig. 3.1a) and b). The area of each cell is $2 \cdot 2\,\mathrm{cm}^2$. The design of the grid fingers is different for the two cell types, which leads to different active cell areas. It is important to note that the area of the metal contact and metal grid of the cells is not subtracted from the

cell surface area in the analysis of area-dependent solar cell values. The active cell area is assumed to be $4\,\mathrm{cm}^2$. This leads to a systematic error in the area-dependent values such as the current density of a cell. The metal contact bar at the front side of the 3G30 cells measures $5.5 \cdot 0.8\,\mathrm{mm}^2$, the bar of the 4G32 is smaller with $3.5 \cdot 0.8\,\mathrm{mm}^2$. Taking into account only the metal contact bars, area-dependent values such as current densities are underestimated $1.1\,\%$ for 3G30 cells and $0.7\,\%$ for 4G32 cells.

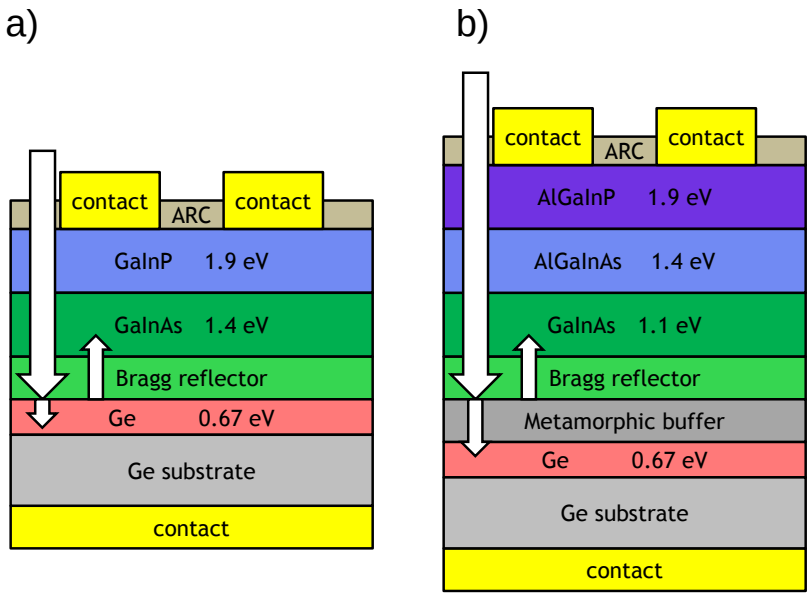

Figure 3.2 Sketch of the structure of a 3G30 3J cell (a) and a 4G32 4J cell (b).

In Fig. 3.2a) and b), the structure of a 3G30 3J cell and a 4G32 4J cell is shown. The 3G30 cell is grown on a germanium wafer. All subcells are lattice matched at a lattice constant of $5.66\,\text{Å}$ as shown in Fig. 3.3, so there is no need for a metamorphic layer. The bottom cell is a germanium cell. On top of the bottom cell, a Bragg reflector is grown [16]. The Bragg reflector is reflective near the band edge of GaInAs and transparent in the wavelength region, which is absorbed by the Ge cell. This allows thinning of the GaInAs cell while still maintaining sufficient current collection. The photons which could not be absorbed by the thin GaAs cell due to its low thickness are partly reflected by the Bragg reflector and can be absorbed in the second passage through the GaInAs cell. The thinner a cell is, the more the necessary minority carrier diffusion length for current generation decreases. Therefore, the thinner a solar cell is, the radiation harder it becomes. The middle cell is a $Ga_{0.99}In_{0.01}As$ cell, but due to the low Indium content, it will be referred to as GaAs cell or middle cell in the relevant main chapters of this work. The top cell consists of $Ga_{0.5}In_{0.5}P$. The top of each cell is covered by anti-reflective coating (ARC) and metal grid fingers as well as a metal contact bar. The rear side of the cell is fully metalized.

The 4G32 cell is grown on a germanium wafer as well. The Ge or J4 cell has a different lattice constant than the other three subcells, which is why there is a metamorphic layer on top of the Ge cell of the 4G32. On top of it, there is a Bragg reflector. On top of the Bragg reflector, there is the $Ga_{0.7}In_{0.3}As$ or J3 cell. On top of J3, there is the $Al_{0.36}Ga_{0.36}In_{0.28}As$ or J2 cell and the $Al_{0.3}Ga_{0.02}In_{0.68}P$ or J1 cell. Similarly to the 3G30, there is an ARC and a metal grid on the very top of the cell. The rear side is fully metalized. The element ratios of J3, J2, and J1 are important for the NIEL calculation of the different subcells and are therefore determined using Fig. 3.3. For the three element subcell InGaAs, the ratios of In and Ga are directly read off the graph. For the four element subcell AlInGaP, the ratios are determined as follows: The ratio of Ga is small and estimated to be 0.02. The ratios of Al and In are then calculated by determining the distance from the AlInGaP data point to the AlP resp. the InP data point and by translating the distances into proportional element amounts. The ratios of the AlInGaAs are also determined by distance determination of the AlInGaAs data point to each of the data points of GaAs, InAs, and AlAs and by weighing these distances with the full distance from i.e. InAs to the line GaAs-AlAs. In a last step, these three ratios are normalized to the value of one.

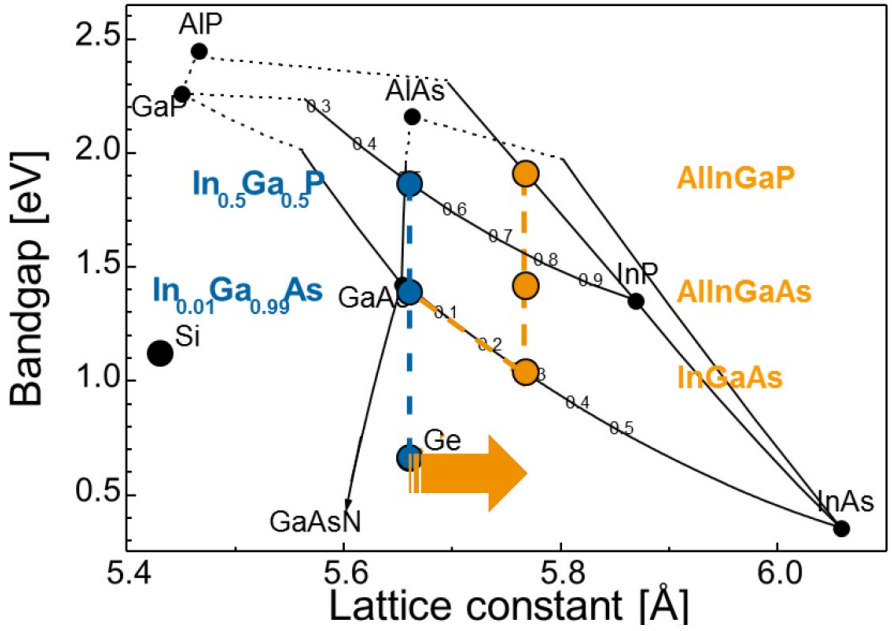

Figure 3.3 Bandgap and lattice constant of different material combinations including the subcell materials of the 3G30 and the 4G32 cell.

In Fig. 3.4, the structure of both the three isotype cells of the 3G30 (a-c) as well as of the four isotype cells of the 4G32 (d-g) are shown. Each isotype cell is a single junction cell. In each isotype cell, only one subcell is electrically active. The purpose of the cell materials of the other subcells is to provide representative shielding from particles and representative absorption of photons. However, the cell materials of the other subcells

are not both p- and n-doped to create a solar cell. Instead, they are only n-doped if the inactive subcell material lies above (meaning sun-facing) the active cell and they are only p-doped if the inactive subcell material lies below (meaning non sun-facing) the active cell.

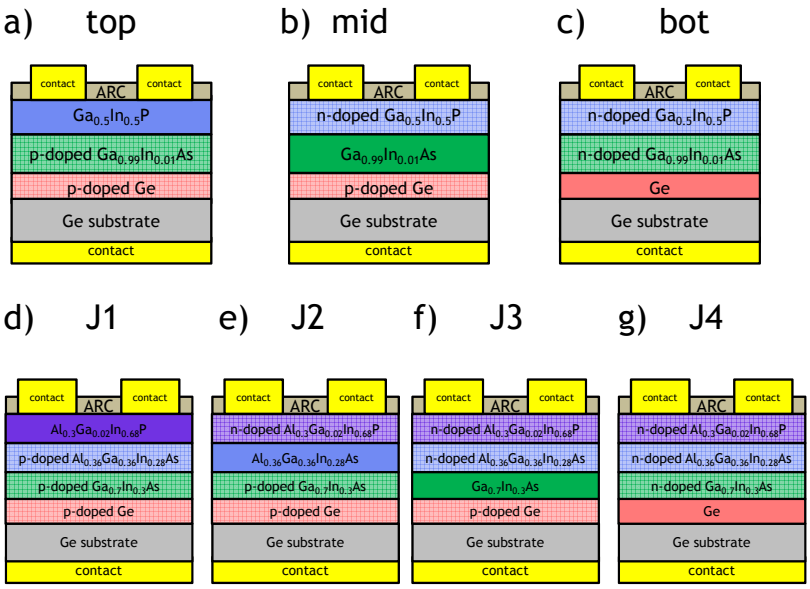

Figure 3.4 Sketch of the structure of a 3G30 top (a), middle (b), and bottom cell (c) as well as of a 4G32 J1 (d), J2 (e), J3 (f), and J4 cell (g).

3.2 Particle irradiation details

For this thesis, 3G30 and 4G32 solar cells were irradiated with electrons and protons according to Tables 3.1 and 3.2. All irradiated solar cells had an area of $4\,\mathrm{cm}^2$. The irradiations were carried out at different particle accelerators because no single facility exists that can offer all particles and energies. In addition, few particle accelerators are equipped with the required beam-widening optics because they are typically built for nuclear physics experiments during which the beam is focused as much as possible.

For irradiating the 3G30 and 4G32 cells with 1 and $3\,\mathrm{MeV}$ electrons, the van de Graaff accelerator at Technical university (TU) Delft was used. The samples were irradiated at a flux of $1.5e12\,\frac{e}{s \cdot cm^2}$. The cell temperature was monitored during particle irradiation and remained between $21.5\,^{\circ}\mathrm{C}$ and $22.0\,^{\circ}\mathrm{C}$. The irradiation took place in nitrogen atmosphere. The homogeneity of the irradiation fluence had an uncertainty of $5\,\%$ over the irradiated area. In the irradiation chamber, 60 cells were irradiated simultaneously. The energy uncertainty was $0.6\,\%$.

In order to irradiate the cells with 1 and $2\,\mathrm{MeV}$ protons, the ion accelerator at Centre de

Sciences Nucléaires et de Sciences de la Matière (CSNSM) was used. Up to a fluence of $1e11\ \frac{e}{cm^2}$, the samples were irradiated using a flux of $1.9e9\ \frac{p}{s \cdot cm^2}$. For higher fluences, a flux of $5.7e10\ \frac{p}{s \cdot cm^2}$ was used. The thermal impact of the irradiation to the cells was calculated resulting in a temperature increase below $1\,°C$. Temperature monitoring was not available at the time of the irradiation. The irradiation took place in vacuum. The homogeneity of the irradiation fluence has an uncertainty of $5\,\%$ over the irradiated area. Seven cells were irradiated simultaneously. The energy uncertainty was $0.7\,\%$.
In order to irradiate the cells with $5\,$MeV protons, the ion accelerator at Centro Nacional de Aceleradores (CNA) was used. The samples were irradiated using a flux of $1e9\ \frac{p}{s \cdot cm^2}$. The thermal impact of the irradiation to the cells was calculated with the result that the power density of the protons was too low to cause any temperature increase above $2\,°C$. The irradiation took place in vacuum. The homogeneity of the irradiation fluence had an uncertainty of $10\,\%$ over the irradiated area, which was $16 \cdot 20\,\mathrm{cm}^2$. The energy uncertainty was $0.1\,\%$.

particle energy (MeV)	electron 1	electron 3	proton 1	proton 2
fluence (cm^{-2})	1e15	1e14	5e10	1e11
fluence (cm^{-2})	5e15	1e15	1e12	1e12
fluence (cm^{-2})	1e16	2e15	3e12	2e12
fluence (cm^{-2})	2e16	5e15	1e13	5e12
fluence (cm^{-2})		1e16		

Table 3.1 Irradiation details for the irradiation of 3G30 3J and isotype cells. Eight 3J, two top isotype, two middle isotype, and two bottom isotype cells were irradiated per particle energy and fluence.

particle energy (MeV)	electron 1	electron 3	proton 1	proton 2	proton 5
fluence (cm^{-2})	1e14	3e13	3e10	3e10	1e11
fluence (cm^{-2})	3e14	1e14	1e11	1e11	3e11
fluence (cm^{-2})	5e14	3e14	3e11	3e11	1e12
fluence (cm^{-2})	1e15	1e15	1e12	1e12	3e12
fluence (cm^{-2})	3e15	3e15	3e12	3e12	1e13
fluence (cm^{-2})	5.5e15	6e15			
fluence (cm^{-2})	1e16				

Table 3.2 Irradiation details for the irradiation of 4G32 4J and isotype cells. Four 4J, two J1 isotype, two J2 isotype, two J3 isotype, and two J4 isotype cells were irradiated per particle energy and fluence.

Under operation in space, the cells are exposed to elevated temperatures and photon irradiation. Since this can have an effect on the performance of particle-irradiated solar cells, these conditions are reproduced experimentally. After the particle irradiation, the cells are annealed in two steps. Firstly, the cells are irradiated with AM0 light by a solar simulator for $48\,\mathrm{h}$ while being kept at $25\,^{\circ}\mathrm{C}$. Secondly, the cells are annealed for $24\,\mathrm{h}$ at $60\,^{\circ}\mathrm{C}$ under darkness. These parameters for annealing are taken from the European cooperation for space standardization (ECSS) [17].

3.3 Characterization setup

In this section, the measurement setups used for cell characterization are described.

3.3.1 Dark current-voltage measurement

In order to measure the current-voltage characteristics of a solar cell under darkness, a Keithley 2420 3A sourcemeter is used. The solar cell is contacted on the fully metalized bottom side by laying it on a brass block and applying vacuum through small holes in the block. The block is temperature controlled. It is connected via a heat exchanger to a water reservoir, which can be heated or cooled. The top side of the cell is contacted by brass pins, which are pressed with pre-loaded springs on the top metal pad. Four-terminal sensing is used, which means that the voltage is applied by the Keithley on two contacts and the current through the cell is measured on two separate contacts to exclude the wire resistance. The cell and the contact system are located in an enclosed chamber during the measurement to ensure that no light affects the measurement. The Keithley device is connected by GPIB to a desktop computer. To control the measurement, the software Labview is used.

3.3.2 Solar Simulator

To determine the behavior of a solar cell under AM0 illumination, the AM0 spectrum has to be generated artificially by a solar simulator in the laboratory. For the purposes of this thesis, two separate solar simulators are used for the illumination of 3J and 4J cells. The schematic structure of the solar simulators is depicted in Fig. 3.5a) and b).

For 3G30 cells, three different lamps with adjustable currents are used to control the light input resp. current output of each of the three subcells. A xenon lamp with $1600\,\mathrm{W}$ power is used to control the top cell current. For the middle cell, a halogen lamp with $400\,\mathrm{W}$ power is used. Another $400\,\mathrm{W}$ halogen lamp is used for the bottom cell in combination with a low pass filter to reduce the influence of this lamp to the middle cell. The light is guided resp. filtered by a dichroic filter according to Fig. 3.5a)

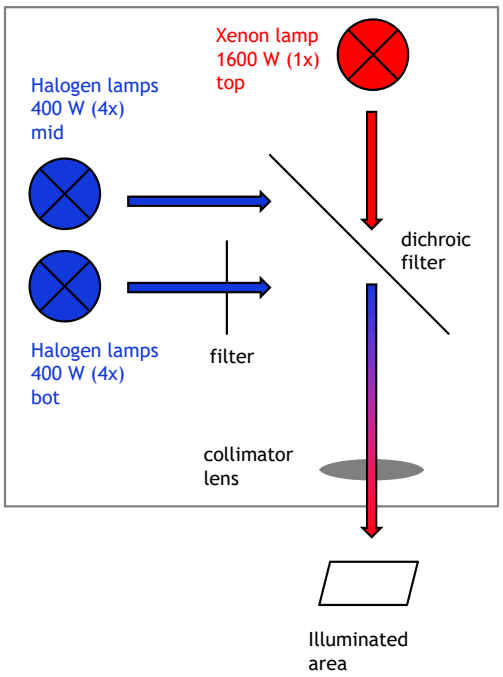

(a) Solar simulator used to characterize 3J cells.

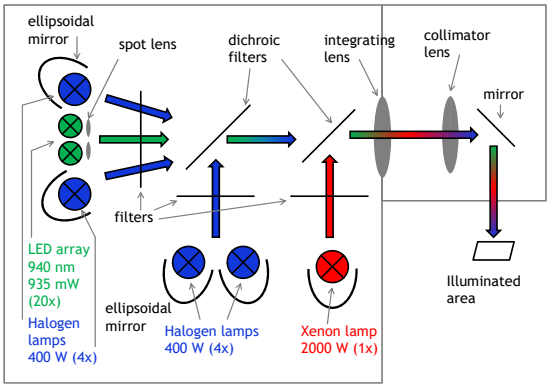

(b) Solar simulator used to characterize 4J cells.

Figure 3.5 Sketches of the solar simulators used to characterize solar cells.

onto a common path. Before leaving the housing of the solar simulator and irradiating the sample, the light of all three lamps is collected and focused by a collimator lens. Before the measurement, the spectrum of each solar simulator is calibrated to ensure comparable results. In order to achieve this, two sets of calibration standards, so-called secondary working standards (SWS), are used. One set consists of a 3J cell, a top, a middle and a bottom isotype cell. The other set consists of a 4J, J1, J2, J3, and J4 isotype cell. Each of these secondary working standards is calibrated with reference to a primary standard. Primary standards have been calibrated from time to time since 1976 by CNES using stratospheric balloons [18]. To calibrate the solar simulator, the

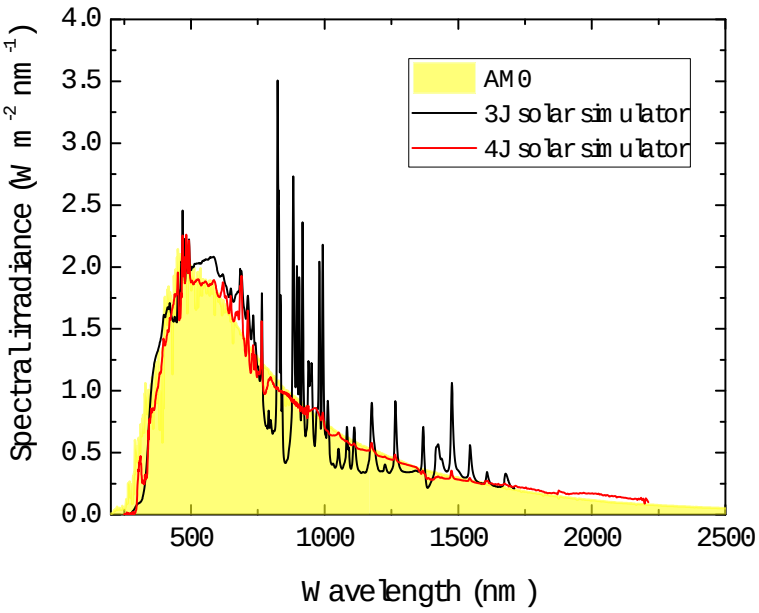

Figure 3.6 AM0 spectrum compared to the spectra of the 3J and 4J solar simulator.

isotype cells are placed in the illumination field and the generated current is measured by measuring the voltage drop on a $0.1\,\Omega$ resistor. Subsequently, the lamp intensities of the solar simulator's different lamp arrays are adjusted until the current equals the calibration value. The same is done for every isotype cell at least two times in a row to adjust for mutual impact of the different lamps to the different isotype cells. As a final means of control, the calibrated MJ cell is measured.

For 4J LIV measurements, the 4J solar simulator is used. It offers four sets of lamps whose intensities can be tuned. The 4J solar simulator is depicted in Fig. 3.5b). For the J1 subcell, there is a $2000\,$W xenon lamp. For the J2 subcell, there are two $400\,$W halogen lamps. For the J3 subcells, there is an LED array, which consists of 20 $935\,$mW LEDs with a peak wavelength of $940\,$nm. The light of each LED is confined by a condensing spot lens. For the J4 subcells, there are two $400\,$W halogen lamps. An ellipsoidal mirror is placed behind each of the xenon and halogen lamps with respect to the light path to collect all of the isotropically emitted light. A filter is placed in the path of each lamp to adjust the wavelength range of each lamp or group of lamps. Two dichroic filters are used to couple the light of all sources to a common path. Once the light of all sources is on a common path, it is first homogenized by an integrating lens, then focused by a collimator lens, and finally diverted by a mirror out of the solar simulator onto the solar cell sample.

At both solar simulators, the cell sample is placed on a brass chuck. Small holes in the brass chuck can be evacuated to pull the cell towards the chuck in order to thermally connect the cell to the chuck. The chuck is temperature-controlled by water cooling and

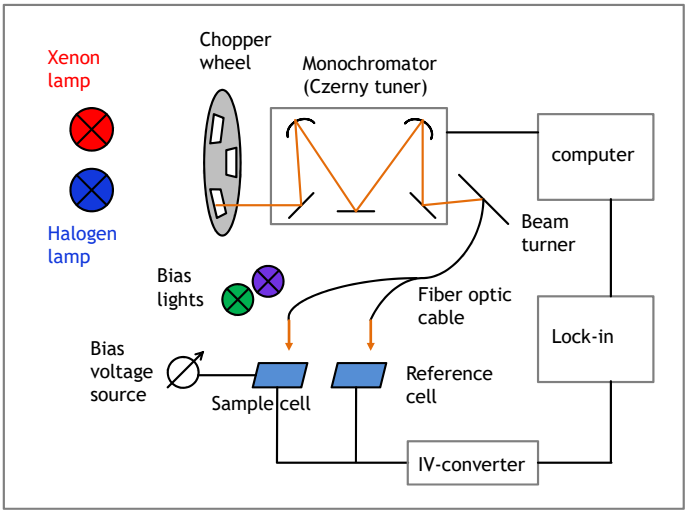

Figure 3.7 Measurement setup for external quantum efficiency.

current heating. The cells are connected on the rear side by the brass chuck and on the front side by measurement pins. The IV-curve of the cell is measured using the counter voltage method. This means that a voltage is applied to the solar cell to counter the voltage generated by the cell. The applied voltage basically simulates a resistive load to the solar cell. At each voltage applied, the current is measured from $V = 0$ to V_{oc}. This process is controlled by a Labview program, which allows measurement of the whole IV-curve in a time frame of less than a second.

In Fig. 3.6, the AM0 spectrum is shown in comparison to the measured spectra of the 3J and the 4J solar simulator. In the wavelength range from $200\,\text{nm}$ to app. $600\,\text{nm}$ the xenon lamps dominate the spectra. The peak at $450\,\text{nm}$ is the typical emission maximum of xenon lamps. The distinct maxima between $800\,\text{nm}$ and $1700\,\text{nm}$ are typical xenon emission lines. They are visible in the 3J simulator spectrum but not in the 4J simulator spectrum due to the filters installed in the 4J simulator, which prevent these peaks in order to generate less deviation from the AM0 spectrum. The 4J SoSim can match the actual AM0 spectrum better than the 3J SoSim, but the UV range is still underrepresented.

3.3.3 External quantum efficiency

The wavelength dependent ratio of generated electron-hole pairs per incoming photon is called quantum efficiency. Internal quantum efficiency, on the one hand, is the ratio of electron-hole pairs per photon already inside the solar cell. External quantum efficiency,

on the other hand, is the ratio of electron-hole pairs per incoming photon before it enters the solar cell. The difference of the IQE and the EQE is the reflectivity of the solar cell surface. In this thesis, only the EQE is measured. A measurement setup called Spequest Quantum Efficiency from RERA Solutions is used to determine the EQE. It is sketched in Fig. 3.7 and designed to determine the EQE of 1J, 3J, and 4J cells with a maximum wavelength resolution of 1 nm in the range of 300 to 1800 nm. As a means of illumination, a 1 kW xenon lamp is used for the wavelength range from 300 to 1050 nm as well as a 300 W halogen lamp for the wavelength range from 1050 to 1800 nm. Due to the temperature-dependent illumination spectra of the lamps, the lamps are turned on half an hour before the EQE measurement of a solar cell. The setup is calibrated using a Thorlabs silicon photodiode for 300 to 1050 nm and a germanium photodiode for 1050 to 1800 nm. Only one of the lamps is used at a time, which is controlled by a turnable mirror. To determine only the generated solar cell signal, the light is modulated using a chopper wheel and a lock-in amplifier. The light is monochromated using a Czerny turner. The monochromatic light is guided by a beam turner and fibre optic cables to the sample cell as well as to a reference cell. The current of the cell is measured in short-circuit mode and converted to voltage by an IV-converter, which is connected to the lock-in amplifier and a computer.
To be able to measure the different subcells of the 3J and 4J cells, bias lighting is used to inject current in all but the subcell under test in order to ensure that the subcell under test is the current limiting cell for photons of all incoming wavelengths. One halogen lamp and four different LEDs with wavelengths of 470 nm, 730 nm, 870 nm, and 1300 nm are operated with different intensities depending on the subcell under test. Furthermore, the working point of the subcell under test of an MJ cell has to be adjusted by a bias voltage so that the measured subcell is operated under short-circuit conditions.

3.3.4 Capacitance-voltage measurement

Capacitance-voltage (CV) measurements are performed using a Hewlett Packard 4192A LF impedance analyzer. The cell under test is placed on a brass chuck and contacted by spring-loaded pin contacts. The cell is measured in darkness to avoid influence of voltage generated by stray light. The 4192A impedance analyzer can apply voltages with frequencies from 100 Hz to 1 MHz to the device under test. The voltage ranges measured of the cells under test are chosen approximately from 0 V to V_{oc}. For a measurement frequency of 1 kHz, a measurement artifact appears at approximately 0.6 V, which is why this frequency is not used. For the measurements, 2 kHz are used.

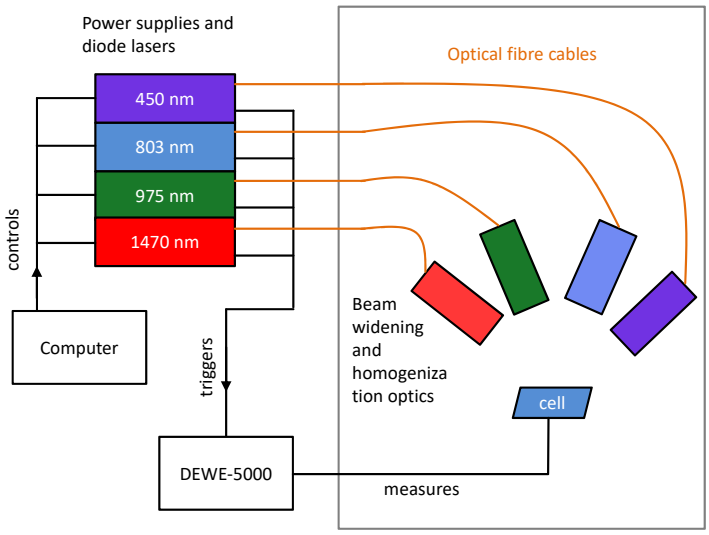

Figure 3.8 Pulsed laser measurement setup.

3.3.5 Pulsed laser measurement

The setup for generating and measuring individual subcell voltages and currents in multi-junction solar cells is depicted in Fig. 3.8. It uses lasers with wavelengths aligned to the multi-junction subcell photon absorption depths that allow generating current in individual subcells only. The setup consists of four high-power diode lasers with a maximal optical power of each $25\,\mathrm{W}$ in continuous wave mode. The wavelengths of the lasers are $\lambda_1 = 450\,\mathrm{nm}$, $\lambda_2 = 803\,\mathrm{nm}$, $\lambda_3 = 975\,\mathrm{nm}$, and $\lambda_4 = 1470\,\mathrm{nm}$. These wavelengths are chosen in such a way that each wavelength is absorbed in a different subcell of a 4J cell. Each laser is connected to a power supply. The power supplies are controlled by Labview programs.

The lasers are led by optical fibers into the measurement chamber, which is a metal casing of approximately one m^2 area and a height of two meters. The chamber fulfills two functions. Firstly, it is important to prevent any stray light from falsifying the measurement. Secondly, the high-power lasers are all class 4 lasers and can cause damage to eyes and skin. The chamber has a security feature which shuts down the lasers if anyone opens the chamber door. Inside the chamber, the fibers are connected to homogenization optics to widen the laser beam and homogenize it to ensure equally distributed illumination all over the solar cell up to $8 \cdot 8\,\mathrm{cm}^2$ [19]. Inside the chamber, the cells are placed onto a temperature-controlled brass chuck. They are fixed on the chuck by applying vacuum to small holes in the chuck. The electrical connection takes place using spring-loaded metal pin contacts on the cell front side and connecting the brass chuck for the cell rear side. The measurement of the voltage generated in the cells by the lasers is performed by a DEWE-5000 measurement system from Dewetron

GmbH. This high-impedance voltage-time logging device has an internal resistance of $1\,\mathrm{M}\Omega$. To trigger the measurement, trigger signals from the lasers are used.

4 Calculation of non-ionizing energy loss

4.1 Introduction

Energetic particles in space can penetrate or even be stopped in matter, causing damage while doing so. Typical damage mechanisms are the displacement of atoms and the ionization of atoms, which are both cumulative effects in space. The dose transferred to the matter due to the ionization of atoms is called total ionizing dose (TID). Ionization of atoms, however, does not alter solar cell properties, but displacement of atoms does. In contrast to TID, the dose corresponding to the displacement of atoms is called total non-ionizing dose (TNID), which is more commonly referred to as displacement damage dose (DDD). It is found in literature as DDD or D_d. In this thesis, D_d is used. D_d in units of $\frac{MeV}{g}$ is the energy per mass which goes into the displacement of semiconductor lattice atoms from their regular position. At the sites where lattice atoms are removed from their regular positions, vacancies are created. Interstitials are created where the removed lattice atoms come to rest. A vacancy and an interstitial are called a Frenkel-pair, which is the simplest kind of electrically active crystal defect and acts, as most defects do, as recombination centers for electrons and holes. Various combinations of vacancies and interstitials of different elements are possible and can form different defects. The defects change the electrical properties of solar cells.

The non-ionizing energy loss (NIEL) describes the rate of energy transfer to the material causing D_d in a similar way as the linear energy transfer (LET) or stopping power does the same for TID. All kinds of charged and uncharged energetic particles such as i.e. electrons, protons, neutrons, alpha particles, muons, and heavy ions can cause D_d. In orbits around Earth, mainly electrons and protons are responsible for solar cell degradation, which is why the testing and simulation is limited to these two particle types. In the following, the computation of the D_d and therefore of the NIEL is explained in detail. This is important because the NIEL is the basis for the solar cell degradation analyses in the following chapters.

4.2 Non-ionizing energy loss

The displacement damage dose caused by particles of fluence ϕ and energy T is computed as the integral over energy of the product of the NIEL in units $\frac{MeVcm^2}{g}$ and the differential particle flux $\frac{d\phi}{dT}$ in units $\frac{\text{no. of particles}}{cm^2 MeV}$. The NIEL describes the energy loss rate of particles passing through matter causing atomic displacements.

$$D_d = \int NIEL(T) \cdot \frac{d\phi}{dT}(T) dT \tag{4.1}$$

For computing D_d in units $\frac{MeV}{g}$, the particle flux and the NIEL have to be known. The particle flux present during a space mission is continuous with regard to energy and can e.g. be computed using ESA's space environment information system (SPENVIS) [20] for specific orbits. Testing of solar cells on Earth is usually performed at particle accelerators with mono-energetic particle beams and a known flux. In each case, for the computation of D_d in an irradiated solar cell, it is necessary to compute the NIEL, which is dependent on the type and energy of the primary particles and on the target material.

Primary particles (electrons and protons in this thesis) are also called incoming or incident particles. They collide with matter (semiconductors in this thesis). The semiconductor atom with which the primary particle collides is called recoil atom. If enough energy is transferred to the recoil atom, the recoil atom itself can displace other semiconductor lattice atoms and cause a collision cascade.

The NIEL is calculated as the integral from the minimum energy required to displace a lattice atom T_d, also called the threshold energy for atomic displacement, to the maximum transferable energy T_{max} over the product of kinetic energy transferred to the target atom T, the Lindhard partition function L, which gives the ratio of primary energy that goes into displacements, and the scattering cross section $\frac{d\sigma}{dT}$, which is also dependent on the energy of the primary particle T_0 and gives the probability for the creation of a recoil with energy T. All parameters needed for the NIEL calculation have to be chosen correctly depending on the particle type and energy range and are explained in detail in the following sections. The NIEL calculation is crucial for the fitting of the solar cell degradation data.

$$NIEL = \frac{N_A}{A} \int_{T_d}^{T_{max}} L(T) T \left(\frac{d\sigma(T, T_0)}{dT} \right) dT \tag{4.2}$$

4.3 Threshold energy for atomic displacement

The threshold energy for atomic displacement T_d is the energy necessary to remove a lattice atom from its position in the crystal lattice to create a stable defect. This process is sketched in Fig. 4.1. A unit cell of a GaAs crystal is shown in its typical Zincblende structure with gallium atoms depicted in green and arsenic atoms in blue. An energetic proton is incoming and collides with an arsenic atom causing a displacement of the arsenic atom and a deflection of the proton. The displacement is only possible for the proton when the energy transferred from the proton through the collision lies above the threshold energy for the displacement of arsenic. This energy can be determined by

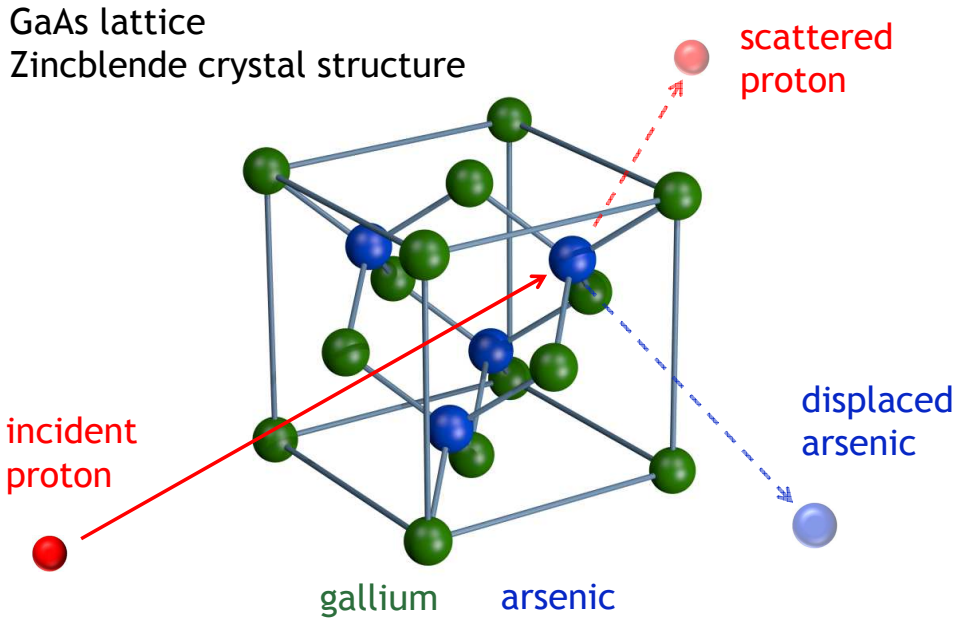

Figure 4.1 Sketch of a proton displacing one arsenic from a GaAs crystal lattice.

molecular dynamics (MD) simulations and is typically in the range of eV, i.e. $10\,\text{eV}$ for a vacancy-interstitial pair of arsenic as well as for gallium due to their similar atomic number and mass. T_d is dependent on the kind of atom, the crystal structure, and also on the angle of the incident particle with respect to the crystal structure. Literature values for several elements have been determined, but they are afflicted with uncertainty and still the topic of ongoing research. Moreover, different defects have different threshold energies, which anneal at different critical temperatures. Therefore, temperature annealing has to be considered.

To include all factors influencing the removal of a lattice atom from its site and therefore the creation of a defect, an 'effective' threshold energy for atomic displacement $T_{d,eff}$ is introduced as a fitting parameter in the degradation analysis of the cells.

4.4 Maximum transferred energy

The maximum energy transferred from an incoming electron or proton to the crystal lattice $T_{max,classical}$ in MeV is determined by the conservation of momentum and energy.

$$T_{max,classical} = 4T_0 \frac{A_R A_L}{(A_R + A_L)^2} \tag{4.3}$$

T_0 is the initial energy of the incoming particle in MeV, A_R its mass and A_L the mass of the lattice atom in atomic units. The classical equation can be used for protons because the relativistic effect does not have to be taken into account for protons in the energy range of interest, which is eV to several MeV. The equation of the classical energy transfer is an approximation of the relativistic energy transfer, which correctly gives the energy transferred from particles to the crystal lattice over all energies.

$$T_{max,relativistic} = 2T_0 \frac{T_0 + 2A_R uc^2}{(1 + \frac{A_R}{A_L})^2 A_L uc^2 + 2T_0} \tag{4.4}$$

The speed of light is c and u is the unified atomic mass unit.

4.5 Lindhard partition function

Primary particles transfer energy to lattice atoms basically in three ways. The first way is through inelastic collisions with bound lattice electrons. The transferred energy causes excitations and ionizations. The second way is through elastic collisions with the lattice nuclei. The transferred energy causes displacements of the lattice atoms. The third way is through inelastic collisions with the lattice nuclei. The transferred energy causes nuclear fissions and displacements. Inelastic collisions with nuclei can only occur at high energies. For protons, the minimum energy is app. $10\,$MeV [21]. Since the highest proton energy used in the experiments described in this thesis is $5\,$MeV, the computation of the NIEL caused by inelastic collisions to nuclei is neglected.

The Lindhard partition function or 'damage efficiency' L gives the ratio of the recoil energy that goes to the displacement process. The value 1-L would give the ratio of recoil energy transferred to ionizations. The Lindhard partition function, see Eq. 4.5 with Eqs. 4.6 and 4.7, is calculated using the Akkerman Barak approximation [22] of the Lindhard screened potential scattering theory based on the Thomas-Fermi model [23–25]. The

Akkerman Barak approximation is used because it gives values which are better in agreement with low-energy recoil ions than the original partition function [22].

$$L(T) = \frac{1}{1 + F_L(3.4008\epsilon^{\frac{1}{6}} + 0.40244\epsilon^{3/4} + \epsilon)} \tag{4.5}$$

$$F_L = \frac{0.0793 Z_R^{\frac{2}{3}} Z_L^{\frac{1}{2}} (A_R + A_L)^{\frac{3}{2}}}{(Z_R^{\frac{2}{3}} + Z_L^{\frac{2}{3}})^{\frac{3}{4}} A_R^{\frac{3}{2}} A_L^{\frac{1}{2}}} \tag{4.6}$$

$$\epsilon = \frac{T A_L}{30.724 Z_R Z_L (A_R + A_L)(Z_R^{\frac{2}{3}} + Z_L^{\frac{2}{3}})^{\frac{1}{2}}} \tag{4.7}$$

In these equations, Z_L and Z_R are the atomic numbers of the lattice and primary particles. A_L and A_R are the masses of the lattice and primary particles and T is the recoil energy.
The product of energy and Lindhard partition function $T \cdot L(T)$ is called damage energy. The damage energy is the energy value which is deposited via displacement damage inside a medium by a recoil nucleus with kinetic energy T.

4.6 Scattering cross section

The differential scattering cross section $\frac{d\sigma}{dT}$ gives the probability that a recoil with energy T is created in the collision with a primary particle with energy T_0. It is dependent on the particle type and energy range. For electrons, the collision is treated as coulombic collision with a point-like nucleus using the Mott-McKinley-Feshbach scattering cross section $\frac{d\sigma}{dT}_{Mott}$ [25, 26].

$$\frac{d\sigma}{dT}_{Mott} = \frac{Z_L^2 \pi r_e^2 T_{max}}{\gamma^2 \beta^4 T^2 (1 - \beta(\beta - \pi Z_L \alpha)\frac{T}{T_{max}} - \pi Z_L \beta \alpha \sqrt{\frac{T}{T_{max}}})} \tag{4.8}$$

As stated before, to compute the maximum transferred energy from electrons to the crystal atom, the relativistic term $T_{max,relativistic}$ is used. α is the fine structure constant and r_e the classical electron radius. The relativistic quantities β and γ are defined as

$$\beta = \sqrt{1 - \frac{1}{\gamma^2}} \tag{4.9}$$

and

$$\gamma = 1 + \frac{T_0}{m_R c^2} \tag{4.10}$$

, where T_0 is the kinetic energy of the primary particle, m_R is the rest mass of the primary particle, and c the speed of light.

Collisions of protons with lattice atoms are treated depending on the kinetic energy of the protons. Low-energy protons with $T_0 < 1\,\text{keV}$ are treated as screened Coulomb collisions using the Ziegler-Biersack-Littmark (ZBL) universal potential [27]. The universal screening potential is derived from experimental data on interatomic potentials.

$$\frac{d\sigma}{dT}_{ZBL} = \frac{\pi}{2} a_U^2 \frac{\sqrt{T_{max}}}{\epsilon} \frac{f}{T^{\frac{3}{2}}} \tag{4.11}$$

with coefficients $a = 1.1383$, $b = 0.01321$, $c = 0.21226$ and $d = 0.19593$ [27].

The function f is described as [28]

$$f(x) = \frac{ln(A)}{2B} + \frac{ax}{2AB} - \frac{x(ln(A))(1 + bcx^{c-1} + \frac{d}{2}x^{0.5})}{2B^2} \tag{4.12}$$

The dimensionless collision parameter x is

$$x = \epsilon' \sqrt{\frac{T}{T_{max}}} \tag{4.13}$$

. The parameters A and B are

$$A = 1 + ax \tag{4.14}$$

and

$$B = x + bx^c + d\sqrt{x} \tag{4.15}$$

. The dimensionless ZBL reduced energy is

$$\epsilon' = \frac{32.53 A_L T_0}{Z_L Z_R (A_L + A_R)(Z_L^{0.23} Z_R^{0.23})} \tag{4.16}$$

The parameter a_U is the ZBL universal screening length and is defined as

$$a_U = \frac{0.8854 a_0}{Z_L^{0.23} Z_R^{0.23}} \tag{4.17}$$

with a_0 being the Bohr radius of the hydrogen atom.
For protons with an energy higher than $1\,\text{keV}$, the Wentzel-Moliere (WM) cross section was used [29–31].

$$\frac{d\sigma}{dT}_{WM} = \frac{1}{(4\pi\epsilon_0)^2} (\frac{T_{\mu_r} Z_R Z_L e^2}{c p_{\mu_r}})^2 F\pi \frac{T_{max}}{(T_{max} A_s + T)^2} \tag{4.18}$$

. If the rest mass of the primary particle m_R is not negligible to the rest mass of the lattice particle m_L, an effective particle with a relativistic reduced mass μ_r has to be considered, which is

$$\mu_r = \frac{m_R m_L c^2}{T_{cm}} \tag{4.19}$$

, where the total center of mass energy T_{cm} is

$$T_{cm} = \sqrt{T_L^2 + T_R^2 + 2T_L T_R} \tag{4.20}$$

. The energy and momentum of the effective particle are

$$T_{\mu_r} = \gamma \mu_r c^2 \tag{4.21}$$

and

$$p_{\mu_r} = \gamma \mu_r c \tag{4.22}$$

with

$$\gamma = \frac{1}{\sqrt{1-\beta^2}} \tag{4.23}$$

and

$$\beta = \frac{v_r}{c} \tag{4.24}$$

. A_s is the Moliere and Bethe screening parameter [32]

$$A_s = \frac{\hbar}{2p_{\mu_r} a_{TF}}^2 (1.13 + 3.767 \frac{\alpha Z_L}{\beta}^2) \tag{4.25}$$

, where α is the fine structure constant and a_{TF} is the Thomas Fermi screening length and given by

$$a_{TF} = \frac{0.885 a_0}{Z_L^{\frac{1}{3}}} \tag{4.26}$$

. The Form factor from Butkevick [33] takes into account nuclear size effects at high energies and is given by

$$F = \frac{1}{(1 + \frac{(p_N R_N)^2}{12})^2} + \frac{1}{Z_L} \tag{4.27}$$

with R_N being the size of the target nucleus and p_N the momentum transferred to the target nucleus

$$p_N = \gamma m_R \beta c \sqrt{\frac{T}{T_{max}}} \tag{4.28}$$

4.7 Realization in matlab

The NIEL computation was realized as program in matlab. The program is structured modularly. The source code is attached in the annex of this thesis. The NIEL can be computed by the program for single- and multi-element semiconductors consisting of up to four elements. Four elements is the maximum which is needed for 4J subcells. The main functions to be executed are called NIEL1, NIEL2, NIEL3, and NIEL4. These functions then execute all other functions they need for the NIEL calculation on their

own. The input parameters which have to be provided are the primary particles (i.e. electrons or protons), the lattice elements (i.e Gallium or Arsenide), their ratio in the semiconductor (i.e. 0.5), and the threshold energy for atomic displacement (i.e. $10\,\mathrm{eV}$). The NIEL functions compute NIELs for a chosen range of particle energies and provide NIEL plots.

To calculate the NIEL of a compound semiconductor, the different components of the semiconductor are weighed according to their atomic masses using Bragg's rule [34, 35], i.e. for GaAs:

$$NIEL_{GaAs} = \frac{NIEL_{Ga}A_{Ga} + NIEL_{As}A_{As}}{A_{Ga} + A_{As}} \tag{4.29}$$

Each semiconductor compound has its own threshold energy for atomic displacement. For the fitting procedure of the solar cell degradation data, the simplification is used that the threshold energy of each element of a compound semiconductor is the same. The implications of this simplification are discussed later in this work.

To verify the function of the NIEL computation, NIEL curves determined with the matlab program are compared to literature values. As an example, the NIEL of GaAs with a threshold energy of $21\,\mathrm{eV}$ is computed and the data is compared to the NIEL data from [36]. The comparison is shown in Fig. 4.2.

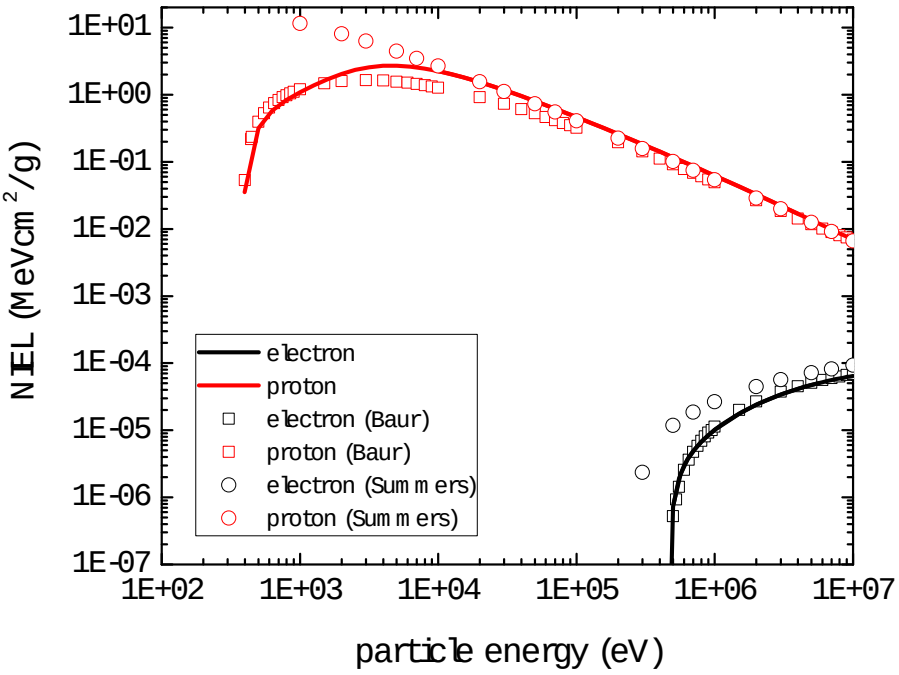

Figure 4.2 Computed NIEL of electrons and protons in GaAs (continuous lines) for $21\,\mathrm{eV}$ threshold energy. The data points are taken from [36] and [37] and show NIELs in GaAs with 21 resp. $10\,\mathrm{eV}$ threshold energy.

The NIEL of GaAs is chosen because it has strong heritage in literature and is also important for the fitting of multi-junction cell degradation done in this work.

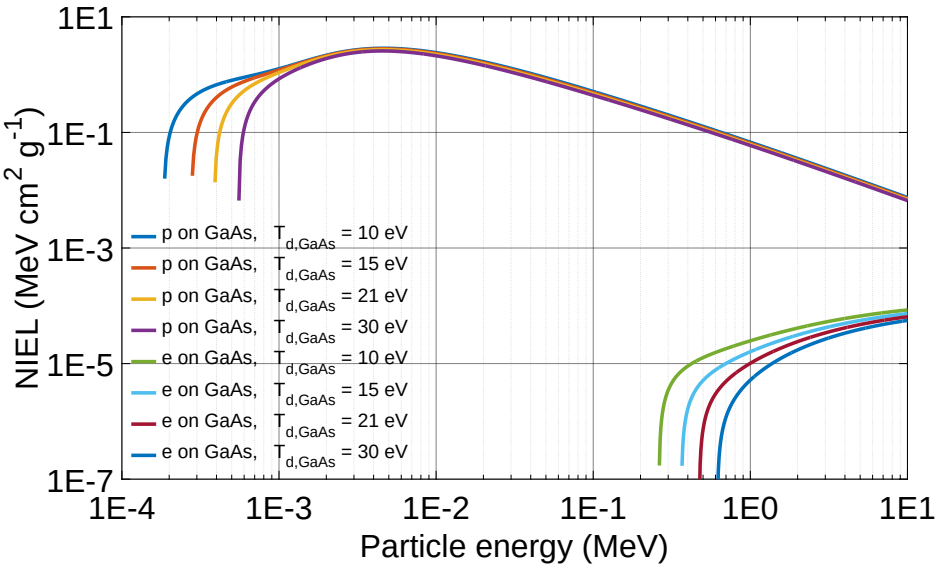

Figure 4.3 NIEL of electrons and protons in GaAs for different threshold energies for atomic displacement T_d

In Fig. 4.2, the data points of the calculated proton and electron NIEL in GaAs are shown as lines together with data points from Baur et al. [36] and Summers et al. [37] for comparison. The NIEL of the protons is in good agreement with the NIELs from literature for energies above approximately $100\,\text{keV}$. For energies below $100\,\text{keV}$, the computed NIEL and the NIEL from [36] are still aligned, whereas the NIEL from [37] diverts. This is due to the different threshold energies T_d. The NIEL from Summers is computed with a T_d of $10\,\text{eV}$, whereas the other two NIELs are computed with $21\,\text{eV}$. The whole energy range of the proton T_d is important for computing the D_d with a given particle environment in space with a continuous energy range. For the analysis of irradiation test results with typical solar cell irradiation test energies in the order of magnitude of $1\,\text{MeV}$, the proton NIEL cannot be used to fit T_d because it is not sensitive to it. For fitting T_d, the electron NIEL is used because it is more sensitive regarding changes in T_d than the proton NIEL. As can be seen in Fig. 4.2, the computed electron NIEL matches the NIEL from Baur well (both $21\,\text{eV}$ threshold energy), whereas the electron NIEL with $10\,\text{eV}$ has a different course for the whole energy range.

The NIEL computation is used in this thesis mainly to compute NIEL values for different threshold displacement energies. To highlight the strong dependence of the electron NIEL on threshold displacement energies, the electron and proton NIELs of GaAs with threshold energies of 10, 15, 21, and $30\,\text{eV}$ are shown in Fig. 4.3. For protons as well as for electrons, the NIEL increases with decreasing threshold displacement energy. The reason for this is: the lesser the necessary energy for the displacement of

lattice atoms, the more lattice atoms can be displaced by recoil particles. For protons, the NIEL reaches its maximum at app. $4\,\mathrm{keV}$. For higher energies, the NIEL decreases. The reason for the decrease is that the target lattice atom is screened by electrons. At low proton energies (compared to its rest mass), the time of transit is long enough so that the bound electrons of the target atom have time to move in response to the protons electric field. This so-called electron screening increases the effective cross section of the collision process and therefore increases the NIEL. For higher energies, the effective cross section decreases along with the NIEL.

For protons with an energy below $10\,\mathrm{keV}$, the NIEL is strongly dependent on T_d. This energy range is however not important for solar cells in space because low energetic protons are absorbed in the cover glass, which is present on solar cells in space. The NIEL of electrons however is dependent on T_d in the range from $100\,\mathrm{keV}$ to $10\,\mathrm{MeV}$. This makes degradation data from cells irradiated with electrons sensitive to T_d. This fact is used in the degradation data analysis process explained later in this work.

5 Method for the degradation analysis of solar cell data using the threshold energy for atomic displacement

Parts of this chapter are published in [38].

5.1 Introduction

The accurate prediction of solar cell degradation caused by the radiation environment in space is crucial for the correct sizing of the solar array for a given space mission. In order to simulate the degradation inflicted by the particle environment in space, solar cells are irradiated on Earth. Realistically, however, only irradiation tests with mono-energetic particle beams in a limited energy range can be performed. Therefore it is necessary to correlate the tested degradation behavior to the expected degradation behavior in space. Two methods are of importance for the degradation modeling. The first method for fitting the data was developed at the Jet Propulsion Laboratory and is commonly referred to as the JPL or equivalent fluence method [39], [40], [15]. This method requires comprehensive proton and electron irradiation data covering several different fluences and energies. From the degradation data, relative damage coefficients (RDC) are calculated, which relate the damage of various electron and proton energies to the damage of 1 MeV electrons and 10 MeV protons, respectively. Finally, the 10 MeV proton damage is empirically related to 1 MeV electron damage. With the help of these data, the particle environment in space is condensed into an equivalent 1 MeV electron fluence which would cause damage equivalent to the damage of the actual particle environment. The JPL method has a strong heritage, but the downside is that it requires a significant amount of testing for each new generation of solar cells.

An alternative method with a significantly reduced test effort was later developed at the Naval Research Laboratory (NRL), which is referred to as the displacement damage dose method [37, 41–46]. The D_d method was further developed and implemented in the matlab code SCREAM [47], [48], [49]. The difference between the JPL and the

D_d method is that the experimentally-generated RDC values from the JPL method are replaced by an analytical quantity, the non-ionizing energy loss (NIEL). The NIEL, in units of MeV cm^{-2}g^{-1}, represents the amount of energy which electrons and protons lose upon their trajectory through matter by creating displacements in the crystal lattice.

The equivalent fluence method and the displacement damage dose method both result in a similarly accurate prediction of the degradation of a solar cell type, which was shown in the 'Aging study' [50].

Recently, Baur et al. [36] showed that the electron RDCs are directly proportional to the electron NIEL of GaAs when an adapted threshold energy for atomic displacement value T_d for the NIEL calculation is used. This was suggested as an alternative approach to the standard approach in the D_d method, which uses a fixed T_d value but includes an exponent to the electron NIEL, which is treated as a fitting parameter [46]. The effect of the threshold energy for atomic displacements on the NIEL has been investigated by different authors i.e. for silicon [45], [51], GaAs [36] and apart from solar cells also i.e. for a superconducting material [52]. The threshold energy for atomic displacement is the minimum energy necessary to remove one atom from its lattice site and is a critical parameter in the NIEL. There are various T_d values reported in the literature according to varying defect levels introduced in the semiconductor band gap [53], [54], [55]. In the recent work of El Allam et al. [56], discrepancies throughout literature are summarized concerning the scaling of experimental GaAs data with NIEL. It is shown that a threshold energy for atomic displacement in the range of $15\,$eV to $21\,$eV is best suited to fit experimental degradation measurements for many GaAs data. As proposed by Baur, the choice of the appropriate T_d might depend on the temperature environment and associated annealing the cell is exposed to. By using T_d as a fitting parameter, it is more appropriate to refer to it as an effective threshold energy for atomic displacement or, to be even more precise, as an effective threshold energy for the creation of electrically active defects $T_{d,eff}$. Typically, the degradation data of a multijunction solar cell is fitted with the NIEL of one subcell only. Therefore, it is *a priori* not clear whether the $T_{d,eff}$ that is obtained fitting a 3J cell is still specific to this subcell. To address this question further, a comprehensive set of degradation data for 3J $Ga_{0.5}In_{0.5}P$/GaAs/Ge cells as well as for 1J $Ga_{0.5}In_{0.5}P$, GaAs, and Ge cells is analyzed in this work.

5.2 Fitting method with threshold energy

This section provides a detailed description of the fitting of the solar cell degradation data using a nonlinear least-squares approach. For the 3G28 $Ga_{0.5}In_{0.5}P$/GaAs/Ge 3J cell, a large set of irradiation test data exists [57]. Irradiations are carried out for the proton energies of $0.3\,$MeV, $0.75\,$MeV, $6.5\,$MeV and electron energies of $0.5\,$MeV, $1\,$MeV, and $3\,$MeV. Five to six fluences and five (1J isotype) or eight (3J) samples per fluence

are irradiated for each energy. The remaining factors (RF) of the maximum power point (P_{mpp}) are used as an example. The most recent version of the displacement damage dose method is applied, which is described in [47] and [49]. Following the work of Baur, et al. [36], [58], a linear relationship between the energy dependence of the experimental damage coefficients and NIEL is assumed with the effective threshold energy for atomic displacement being used as the fitting parameter. This means that no empirical exponent is needed to fit the data as a function of D_d for electrons. The imposed empiricism is shifted to the $T_{d,eff}$.

5.2.1 Finding the effective threshold energy for atomic displacement

Firstly, only the electron data are evaluated to determine the effective threshold energy for atomic displacement because they are most sensitive to variations in $T_{d,eff}$ as discussed in chapter 4. The displacement damage dose D_d is computed for the experimentally covered fluences ϕ using Equations 4.2 and 5.1.

$$D_d = NIEL(T_0, T_{d,eff}) \cdot \phi \tag{5.1}$$

At this stage, the NIEL of GaAs is chosen because the GaAs subcell is the most radiation-sensitive subcell. As a starting value, the literature value of $10\,\text{eV}$ is used for $T_{d,eff,\text{GaAs}}$ [59]. The RF is plotted against the computed D_d, as shown in Fig. 5.1.

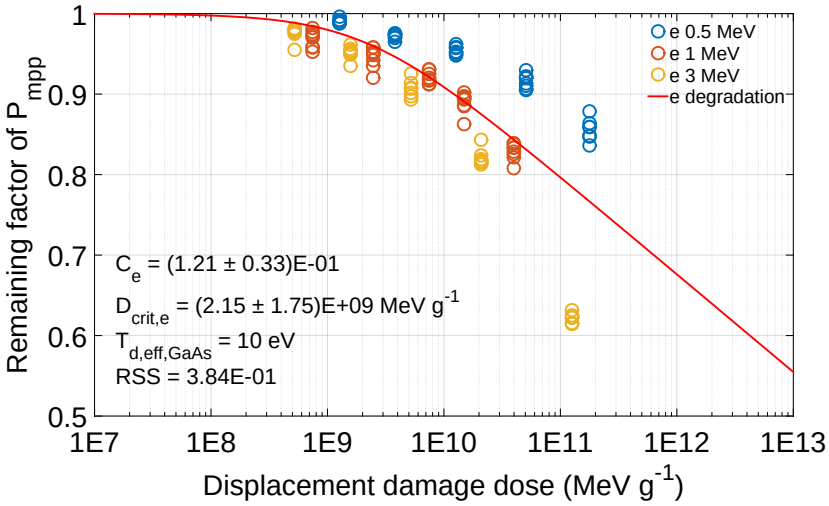

Figure 5.1 Electron data is plotted against D_d which is computed with a $T_{d,eff}$ of $10\,\text{eV}$

The data for the different electron energies do not collapse into a single, characteristic degradation curve. The RF data are expected to follow a logarithmic degradation curve. The fit in Fig. 5.1 is created using equations 5.1 and 5.2 with the three fitting parameters A, C, and D_{crit} [48].

$$RF = A - C \log\left(1 + \frac{D_d}{D_{crit}}\right) \tag{5.2}$$

D_{crit} is the critical D_d value where the remaining factor starts to follow an inverse logarithmic dependence on D_d. C describes the slope of the curve in the high degradation regime. The factor A is set to 1 in this work and not included in the fitting in contrast to the most general case [48]. The quality of the fit is quantified by the residual sum of squares (eq. 5.3), which is a measure of the difference of the fit to the data points.

$$RSS = \sum_i \left(RFfit(D_{d,i}) - RFdata(D_{d,i})\right)^2 \tag{5.3}$$

In the fitting process, the RSS is minimized using 3 fitting parameters (C, D_{crit}, and $T_{d,eff}$). A result is shown in Fig. 5.2.

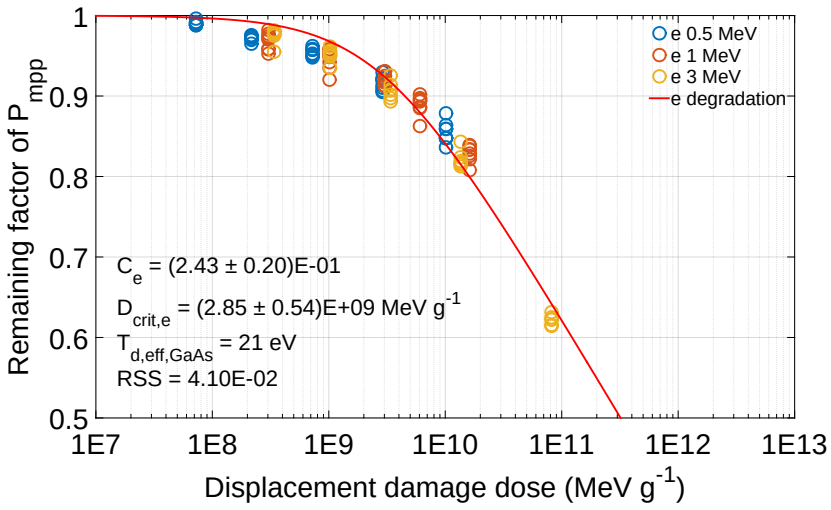

Figure 5.2 Electron data with a $T_{d,eff}$ of 21 eV, which results in a collapse of the electron data to a single curve.

The $T_{d,eff}$ minimizing the RSS is 21 eV, which is in agreement with [58] and produces a much better collapse of the data as a function of D_d. The errors in the fitted parameters C and D_{crit} are represented using $95\,\%$ confidence intervals. For the computation of the non-linear parameter confidence intervals, the standard matlab function 'nlparci' is used, see also [60].

5.2.2 Fitting electron and proton data separately

In the next step, a separate fit is performed for the proton data using (5.1) and (5.2) and the $T_{d,eff}$ is determined with the help of the electron data. Consequently, two sets of fit parameters, (C_p, $D_{crit,p}$) and (C_e, $D_{crit,e}$), are obtained. The results of the separate fits are shown in Fig. 5.3.

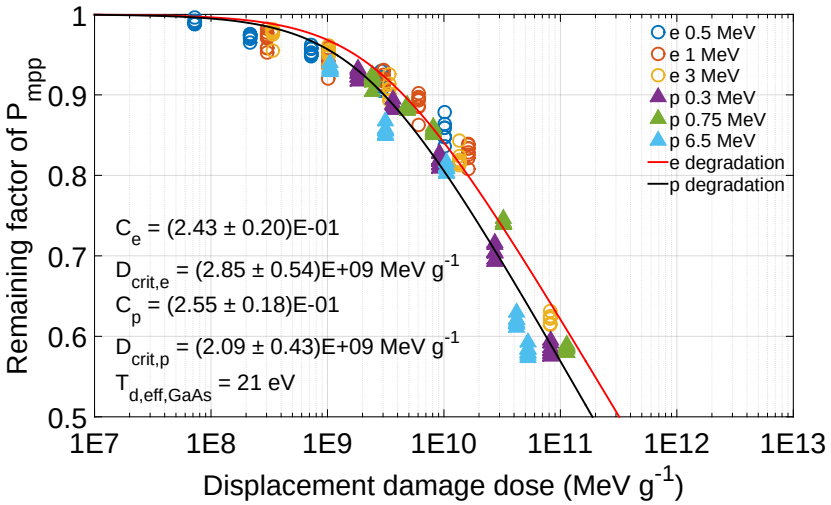

Figure 5.3 Both proton and electron data are fitted separately. The fit parameters are given in the inset.

5.2.3 Convert electron displacement damage dose

There are two possibilities to convert the electron displacement damage dose $D_{d,e}$ into an equivalent proton dose $D_{d,p}$. The first and earlier developed possibility is described i.e. in [46]. It requires that the electron curve and the proton curve degrade with the same slope $C = C_p = C_e$. If that is fulfilled, the electron displacement damage dose can be converted using Eq. 5.4. This method is not used in this chapter but shown for the sake of completeness.

$$D_{d,p} = \frac{D_{d,e}}{\frac{D_{crit,e}}{D_{crit,p}}} = \frac{D_{d,e}}{R_{ep}} \tag{5.4}$$

The second and later developed possibility is described in [48] and it will be used in this chapter. It does not require that the electron curve and the proton curve degrade with the same slope. The parameters determined in the last section are used in the conversion according to Eq. 5.5.

$$D_{d,p} = D_{crit,p} \cdot \left(10^{\frac{A_p - A_e}{C_p}} \cdot \left(1 + \frac{D_{d,e}}{D_{crit,e}} \right)^{\frac{C_e}{C_p}} - 1 \right) \tag{5.5}$$

The combined data, including the electron data with the recomputed D_d are shown in Fig. 5.4.

The characteristic degradation curve, in this case of P_{mpp} of the 3G28 cell type, characterized by the parameters C_p and $D_{crit,p}$, can be used to predict the degradation of the power at maximum power point for a particular orbit. The same analysis is performed for the cell parameters V_{oc} and I_{sc}. In all cases, it is found that the $T_{d,eff}$ of $21\,\text{eV}$ is most effective in minimizing the RSS data.

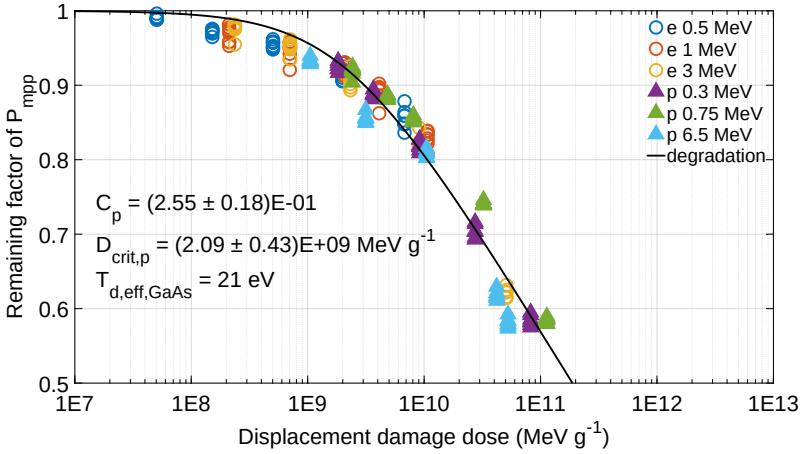

Figure 5.4 The fit parameters are used to recompute the displacement damage dose of the electron data so that all data points collapse to a single curve.

5.2.4 Irradiation boundary conditions

The $T_{d,eff}$ found for fitting all of the ground test data using GaAs NIEL is $21\,\text{eV}$. The result is in line with [58] and confirms the validity of the fitting method. Questions of practical importance relate to the amount of test data required to perform the fitting procedure described above including the choice of irradiation energies. The NRL method requires at least two electron energies to determine the scaling exponent for the electron NIEL or in this case the $T_{d,eff}$ and one proton energy to generate a characteristic degradation curve, which is also in line with the results presented here. The electron energies should be chosen in a range where the NIEL is sensitive to $T_{d,eff}$. The electron energies 0.5, 1, and $3\,\text{MeV}$ are in the energy range where the NIEL is sensitive to $T_{d,eff}$, as shown in Fig. 4.3. Concerning the penetration depths of the protons and electrons, the energies chosen in these analyses are suitable and sufficient to fully penetrate all the active regions of the cell. Range data for protons and electrons in the cell material is taken from [27] and shown in Fig. 5.5.

Moreover, the fitting method requires that the energies of the particles do not change during their transfer through the junctions. Due to the very low junction thicknesses, this is fulfilled for all electron energies with NIEL sensitive to $T_{d,eff}$ and proton energies above a certain level. If the energy of the protons is too low, their Bragg peak lies within a junction, which means the exponentially increased amount of energy at the end of a proton's track is deposited in a junction. This case is investigated for the lowest energy protons in the data, which are $0.3\,\text{MeV}$. The simulation tool TRIM is used to simulate the displacements of atoms in the 3J cell structure [27]. As illustrated by Fig. 5.6, the number of displacements steadily increases while the protons lose energy on their track through the top and middle cell.

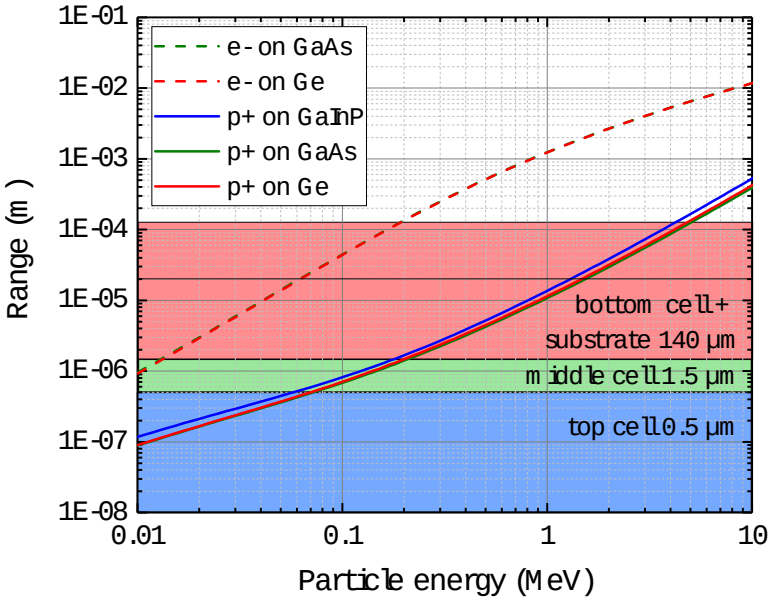

Figure 5.5 Range data for protons and electron in $Ga_{0.5}In_{0.5}P$, GaAs, and Ge. The range is the continuous slowing down approximation range taken from [27].

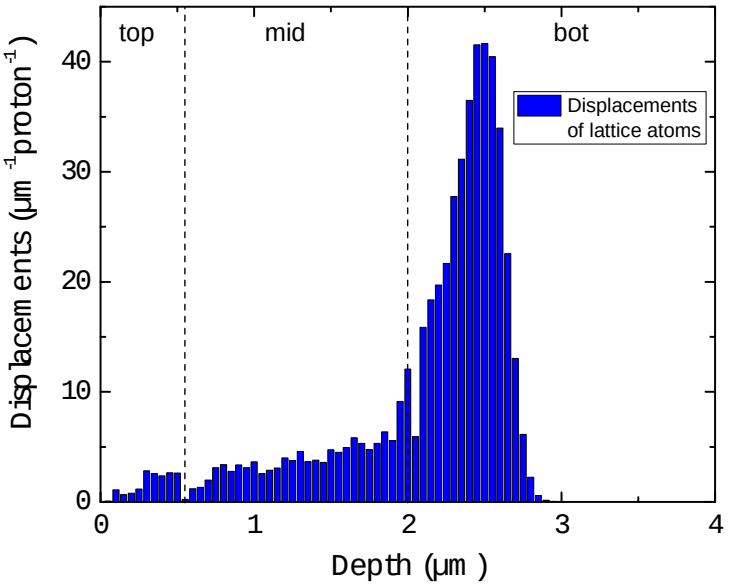

Figure 5.6 Number of lattice atom displacements simulated with TRIM [27] for $0.3\,\mathrm{MeV}$ protons on a $Ga_{0.5}In_{0.5}P$/GaAs/Ge structure.

With $d_{top} = 0.5\mu m$ and $d_{mid} = 1.5\mu m$, however, the cell is thin enough compared to the ion range of $2.5\mu m$, so that the Bragg peak at the end of the track is not located in the top or middle cell but in the bottom cell. The bottom cell generates more current than the top or middle cell and is never current limiting, therefore a slightly increased

damage in the bottom cell does not affect the analysis of the 3J cells. A comparison of the degradation with and without the 0.3 MeV data shows that the determined threshold energy does not change. It is important to mention that the electrical measurements of 3J cells are complicated by the fact that the cells are monolithically grown and therefore connected in series. For the V_{oc}, the contributions of all subcells are added, while the short-circuit current I_{sc} is limited by one subcell and this limitation can change as a function of D_d. The same analysis as for P_{mpp} is performed for the cell parameters V_{oc} and I_{sc}. In all cases, the $T_{d,eff}$ of 21 eV is found to best minimize the RSS data, which is shown in Figs. 5.7 and 5.8.

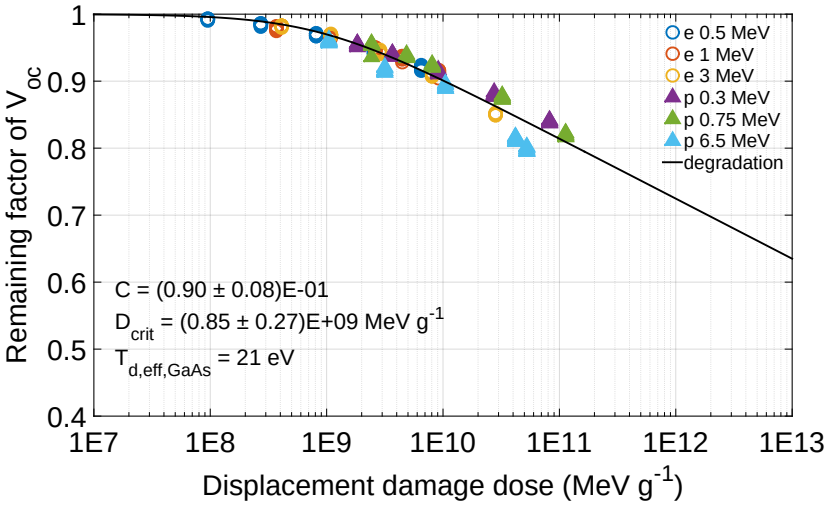

Figure 5.7 Degradation of the open-circuit voltage of 3G28 cells.

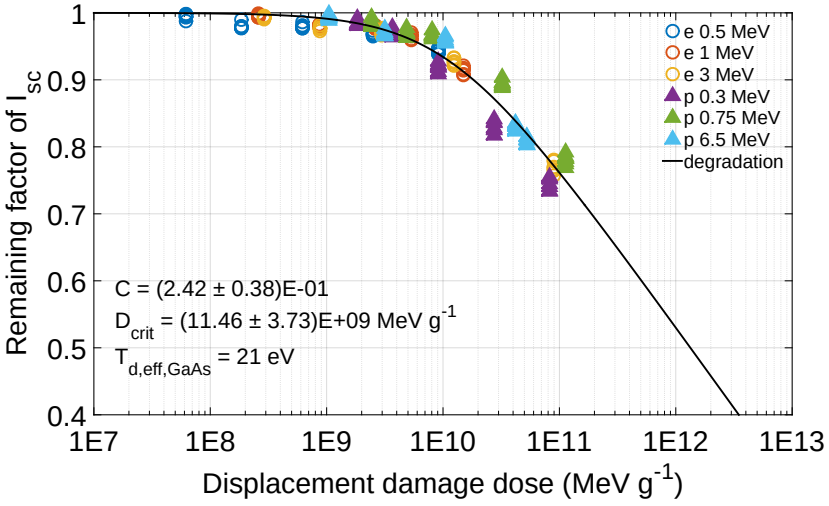

Figure 5.8 Degradation of the short-circuit current of 3G28 cells.

Both parameters can be fitted with the expected logarithmic degradation according to Eq. 5.2. The voltage decreases steadily from the lowest irradiation dose on but the slope is not as steep as the degradation slope of the current. The current degrades

slower than the voltage approximately up to a dose of $3e10\frac{\text{MeV}}{\text{g}}$. Since a multi-junction cell is current-limited at all times by only one of its subcells, the rapid decrease in current from approximately $3e10\frac{\text{MeV}}{\text{g}}$ on is triggered by a change of the current-limiting cell at this dose. At lower displacement damage doses, the current of the multi-junction cell is limited by its top cell, which is more radiation-hard than the middle cell. Therefore, the current of the multi-junction cell shows a relatively slight slope. From a dose of $3e10\frac{\text{MeV}}{\text{g}}$ onwards, the less radiation-hard middle cell generates less current than the top cell, which results in the current of the whole multi-junction cell to be limited by the middle cell. This results in a steeper slope of the multi-junction current. To compare the current degradation of the individual 3G28 subcells, isotype cells, which are single junction cells embedded in an otherwise electrically inactive triple-junction cell stack as described in chapter 3.1, were irradiated and characterized, which is described in section 5.3.4.

5.2.5 Comparison of fitting methods with threshold energy and exponent n

In this chapter, the 'classical' NRL method with exponent n and the NRL method with T_d shall be compared. The fitting method using $T_{d,eff}$ is presented along with results in fitting degradation data of 3J cells. Three data sets from the cell parameters V_{oc}, I_{sc} and P_{mpp} are analyzed and fitted using the classical approach described in [46]. In Table 5.1, the electron fit parameters C_e and $D_{crit,e}$ are compared. The parameters labelled 'n approach' in the Table are determined by applying the NRL method to the data leaving the T_d at a fixed value of $10\,\text{eV}$. The electron data is collapsed to a single curve by redefining the actual electron displacement damage dose $D_{d,e}$ by an effective $1\,\text{MeV}$ electron displacement damage dose $D_{d,e,eff}$ with Eq. 5.6 [41]. The label 'T_d approach' corresponds to the parameters gained by collapsing the electron data through adapting the effective threshold energy for atomic displacement as described earlier in this chapter. For comparison, also the proton fit parameters C_p and $D_{crit,p}$ are given in the Table, which are not dependent on the method of collapsing the electron data.

$$D_{d,e,eff}(1MeV) = \phi \cdot \frac{NIEL_e(E)^n}{NIEL_e(1MeV)^{n-1}} \tag{5.6}$$

The table shows degradation parameters for 3G28 3J cells. The D_d is calculated using the GaAs NIEL. The exponents n are between 2.74 and 2.87, which is in agreement with literature values 1 to 3 for GaAs-based cells [55], [61]. Moreover, the three exponents determined are approximately equal (2.74, 2.77, and 2.87), which is in agreement with the three independently determined threshold energies for atomic displacement, which are all $21\,\text{eV}$. The residual sum of squares is smaller for all cell parameters in

3G28 3J		V_{oc}	I_{sc}	P_{mpp}
n $approach$	C_e	0.055 ± 0.003	0.210 ± 0.025	0.192 ± 0.016
	$D_{crit,e}\,(10^9\,\frac{\text{MeV}}{\text{g}})$	1.38 ± 0.27	42.52 ± 10.01	7.26 ± 1.55
	n	2.77 ± 0.17	2.74 ± 0.06	2.87 ± 0.15
	RSS	0.0062	0.0205	0.0526
$T_{d,eff}$ $approach$	C_e	0.060 ± 0.003	0.295 ± 0.031	0.243 ± 0.020
	$D_{crit,e}\,(10^9\,\frac{\text{MeV}}{\text{g}})$	0.43 ± 0.06	16.50 ± 3.02	2.85 ± 0.54
	$T_{d,eff}$	21	21	21
	RSS	0.0034	0.0182	0.0410
	C_p	0.090 ± 0.008	0.242 ± 0.038	0.255 ± 0.018
	$D_{crit,p}\,(10^9\,\frac{\text{MeV}}{\text{g}})$	0.85 ± 0.27	11.46 ± 3.73	2.09 ± 0.43

Table 5.1 Comparison of the 3G28 3J electron fit parameters according to the NRL method where D_d is calculated by adapting the n exponent with the fit parameters through adapting $T_{d,eff}$. For the NIEL calculation with the n method, a T_d of $10\,\text{eV}$ is used. The NIEL is calculated for GaAs.

the $T_{d,eff}$ approach than in the n approach. Therefore, the degradation behavior is determined more precisely using the $T_{d,eff}$ approach. In conclusion, the NRL approach in combination with $T_{d,eff}$ was verified by analyzing a large set of 3G28 3J degradation data.

5.3 Degradation behavior of single and triple-junction 3G30 cells

With the $T_{d,eff}$ fit method being verified in the last section, in this section the degradation behavior of the three different 3G30 subcells of triple-junction cells will be investigated using this fit method. Towards that end, a degradation study is performed with 3G30 top, middle, and bottom isotype cells. The material compositions of isotype cells are the same as of the corresponding 3J cell but with only one subcell being electrically active, as discussed in 3. 3G30 is the successor cell type of the 3G28 cell type. The materials of the three junctions are the same, which is important for the NIEL calculation. The exact design changes between 3G28 and 3G30 cells are confidential and only known to the cell manufacturer. Two isotype cells and eight 3J cells per fluence are irradiated with 1 and $2\,\text{MeV}$ protons and 1 and $3\,\text{MeV}$ electrons. Each cell is only irradiated with one energy and one fluence of particles. The goal of the irradiation study of isotypes and the corresponding 3J cells is

- to determine the threshold energies for atomic displacement of the different subcell materials $Ga_{0.5}In_{0.5}P$, GaAs, and Ge.

- to determine the critical displacement damage dose, where the current-limiting subcell changes in 3J cells.
- to obtain detailed degradation data from the different isotypes and relate them to the degradation of a 3J cell.

5.3.1 Influence of subcells on open-circuit voltage

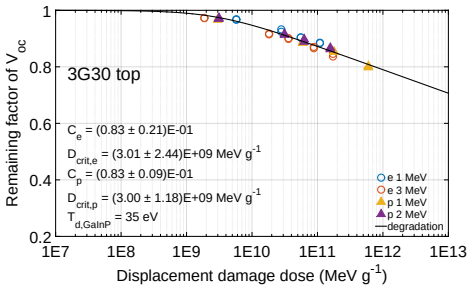

(a) Degradation of open-circuit voltage of 3G30 isotype top cells.

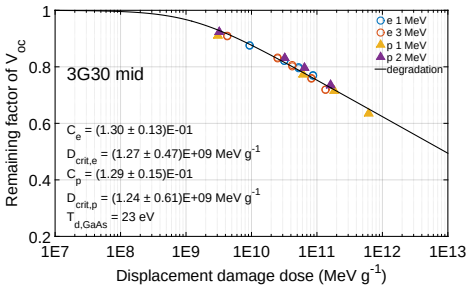

(b) Degradation of open-circuit voltage of 3G30 isotype middle cells.

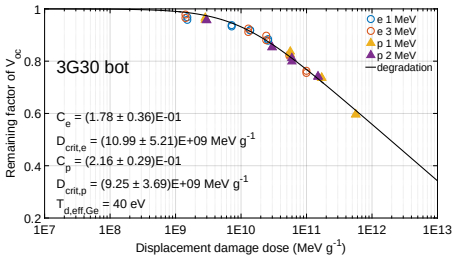

(c) Degradation of open-circuit voltage of 3G30 isotype bottom cells.

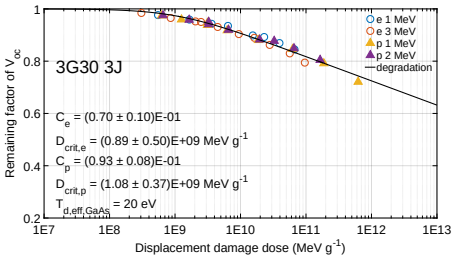

(d) Degradation of open-circuit voltage of 3G30 triple-junction cells.

Figure 5.9 Degradation characteristics of open-circuit voltage of 3G30 isotype and 3J cells.

In Figs. 5.9a-d, the degradation of the open-circuit voltage of 3G30 top, middle, bottom, and 3J cells are shown. For all doses, the voltage of top cells decreases slower than that of middle cells. The voltage of middle cells decreases slower than that of bottom cells for doses up to $1.6e9\,\frac{\text{MeV}}{\text{g}}$, which means middle cells are radiation-harder in that range. Above $1.6e9\,\frac{\text{MeV}}{\text{g}}$ it is the other way round. All images show that the data can be fitted well as a logarithmic decrease. The threshold energies $T_{d,eff}$ of the different subcells are $T_{d,eff,GaInP} = 35\,\text{eV}$, $T_{d,eff,GaAs} = 23\,\text{eV}$, and $T_{d,eff,Ge} = 40\,\text{eV}$. For GaAs and Ge, these values are close to respectively exactly the values found in recent literature of $21\,\text{eV}$ for GaAs [58] and $40\,\text{eV}$ for Ge [62]. For $Ga_{0.5}In_{0.5}P$, a comparison to the literature value cannot be made because equal values of $T_{d,eff}$ are assumed as approximation for all elements of a subcell material in this approach. The determined effective threshold energy for atomic displacement of $35\,\text{eV}$ for $Ga_{0.5}In_{0.5}P$ can be used as comparison value for future studies.

In Fig. 5.10, the degradation curves of the isotype curves are depicted as well as the sum of the isotype curves and the 3J degradation. The sum of the three isotype cell curves represents the 3J cell because individually generated subcell voltages add up in the cell stack. The middle and bottom cell voltages degrade faster than the top cell voltage. This causes also the 3J voltage to decrease faster than the top cell. The behavior of the 3J cell can be approximated well by summing up the contributions of the different isotype cells. The small difference in degradation is caused by fitting uncertainties.

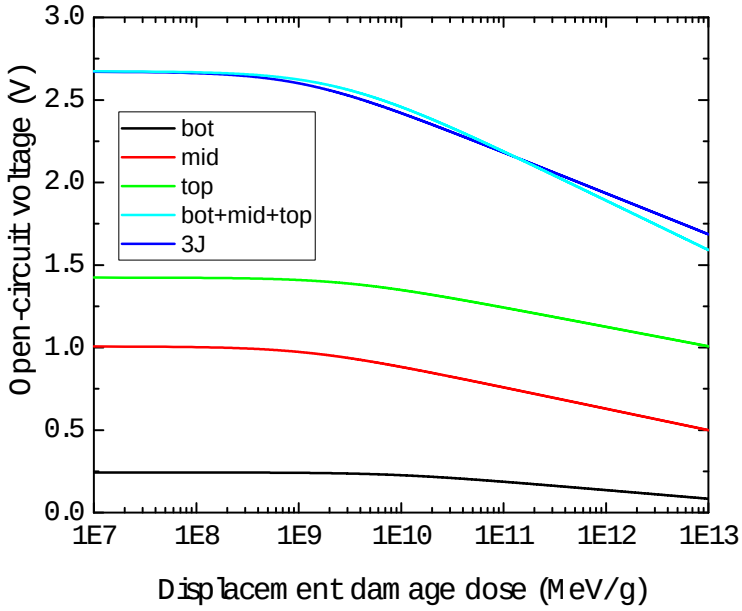

Figure 5.10 Comparison of the degradation of the open-circuit voltage of 3G30 isotype and 3J cells.

In Fig. 5.11, the NIEL curves for protons and electrons on Ge, GaAs, and $Ga_{0.5}In_{0.5}P$ are shown with the $T_{d,eff}$ values found in the degradation analysis of the V_{oc} of 3G30 isotype cells. The proton NIELs are approximately equal from $10\,$keV to $10\,$MeV for all subcell materials. This means that protons lose an equal amount of energy to displacements in all three subcell materials. For electrons, the result is different. While for $Ga_{0.5}In_{0.5}P$ and GaAs, the NIELs are approximately equal, electrons transfer less energy to displacements in Ge. This may be a real effect but it could also be explained by germanium being a single element semiconductor. As explained earlier, the $T_{d,eff}$ is just an effective threshold energy determined by analyzing the degraded solar cell parameters representing the electrically active defects in the solar cells. It is possible that in Ge displacements counter each other. While in GaAs, an As on the site of a Ga is an antisite defect, a Ge on the site of a Ge vacancy would counter the original displacement which created the Ge vacancy. As a result, the sum of displacements in

Germanium is less than expected, which leads to a higher effective threshold energy for atomic displacement. Moreover, it is possible for irradiation to induce crystal defects energetically located at the boundary of the band gap and not in the center of the band gap. Therefore, they can be electrically inactive defects.

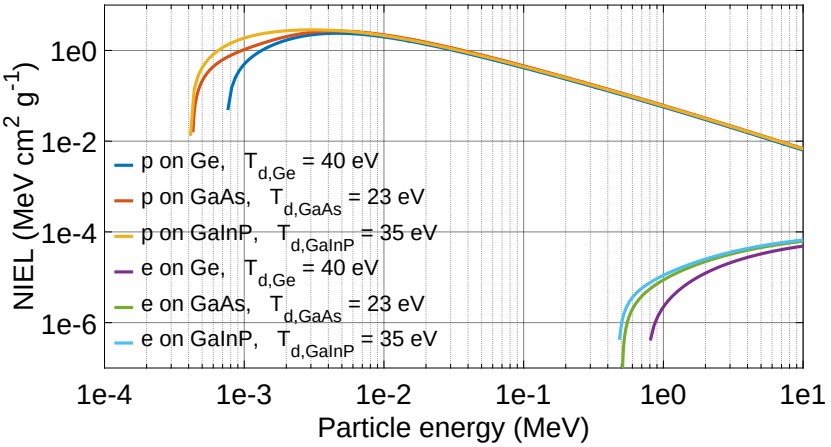

Figure 5.11 Comparison of the NIELs of $Ga_{0.5}In_{0.5}P$, GaAs and Ge.

5.3.2 Influence of subcells on short-circuit current

In Figs. 5.12a-d, the degradation of the short-circuit currents is shown. The top cell degradation begins at a higher dose than the middle cell degradation. The middle cell is clearly the weakest cell regarding irradiation hardness. The degradation of the bottom cell cannot be fitted unambiguously. The reason behind this may be that the bottom cell is not grown epitaxially. Therefore, there might be more defects in the bottom cell than in other subcells already before irradiation. Moreover, the bottom cell is doped by diffusion during expitaxial growth of a buffer layer on top of the junction, which results in a doping density more widely spread than in an epitaxially grown and doped semiconductor. Since the germanium cells generate a BOL current of $31.5\,\frac{\text{mA}}{\text{cm}^2}$, which is 76% higher than the mid cell BOL current and 84% higher than the top cell BOL current, the bottom cell is not current limiting before or after irradiation. The origin of the current behavior of the germanium cells is, however, not investigated in this thesis. It is important to note that the remaining factors in Fig. 5.12c are corrected values because luminescent coupling is taken into account. When measuring the BOL values of the short-circuit current of the bottom cells, also the middle cell material absorbs light, which partly recombines radiatively. These photons emitted from the GaAs region are partly absorbed in the germanium subcell. This leads to an increase of the measured isotype bottom cell short-circuit current compared to the bottom cell short-circuit current in a 3J cell stack where the middle cell charge carriers are extracted and cannot recombine radiatively. This effect is called luminescent coupling. To correct

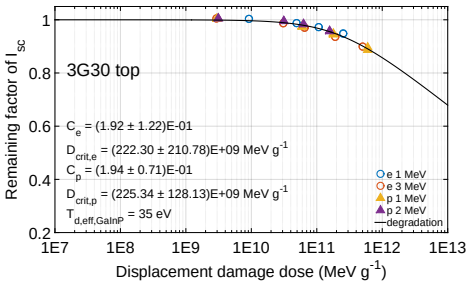

(a) Degradation of short-circuit current of 3G30 isotype top cells.

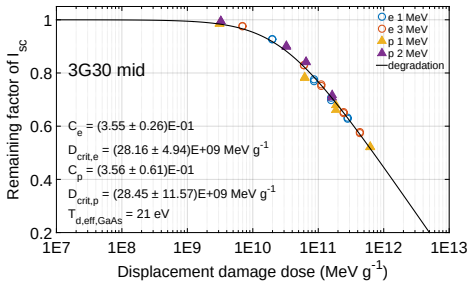

(b) Degradation of short-circuit current of 3G30 isotype middle cells.

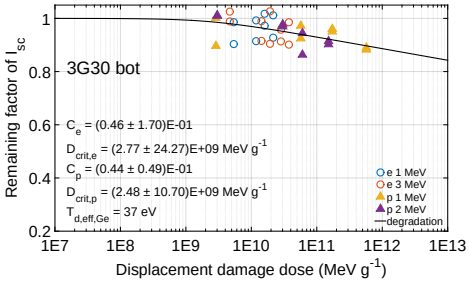

(c) Degradation of short-circuit current of 3G30 isotype bottom cells.

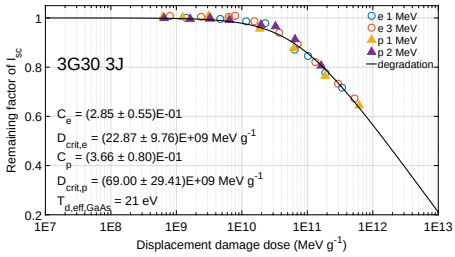

(d) Degradation of short-circuit current of 3G30 triple-junction cells.

Figure 5.12 Degradation characteristics of short-circuit current of 3G30 isotype and 3J cells.

the BOL data, EQE measurements were performed on bottom isotype cells. An example is depicted in Fig. 5.13. In red, the EQE of an isotype middle cell is shown, while in black, the EQE of an isotype bottom cell is shown. Correcting the black curve results in the green curve. The correction process is described in the following. The 'shoulder' of the black curve from approximately 600 to 900 nm originates from luminescent coupling of the bottom cell to the middle cell. To remove the shoulder and get an EQE without luminescent coupling effect (green curve), the additional current caused by luminescent coupling is substracted from the real bottom cell current by substracting the middle cell EQE normalized to the height of the shoulder from the uncorrected bottom cell EQE. The correction process is described in detail in [63]. The overall short-circuit current generated by a subcell can be computed by Eq. 5.7.

$$I_{sc} = \int_{\lambda_1}^{\lambda_2} EQE \cdot AM0 \cdot \frac{q\lambda}{hc} d\lambda \tag{5.7}$$

In this example, the difference between the I_{sc} generated in the bottom cell with and without luminescent coupling from the middle cell is $4.1\,\frac{\text{mA}}{\text{cm}^2}$. This difference is substracted for each cell from the BOL I_{sc} value measured with the solar simulator. The BOL values corrected in this way are used to compute the RF values shown in Fig. 5.12c. The current values of the particle irradiated cells need no correction because the

additional defects prevent radiative recombination in the GaAs region and therefore no artifact exists in EQE results.

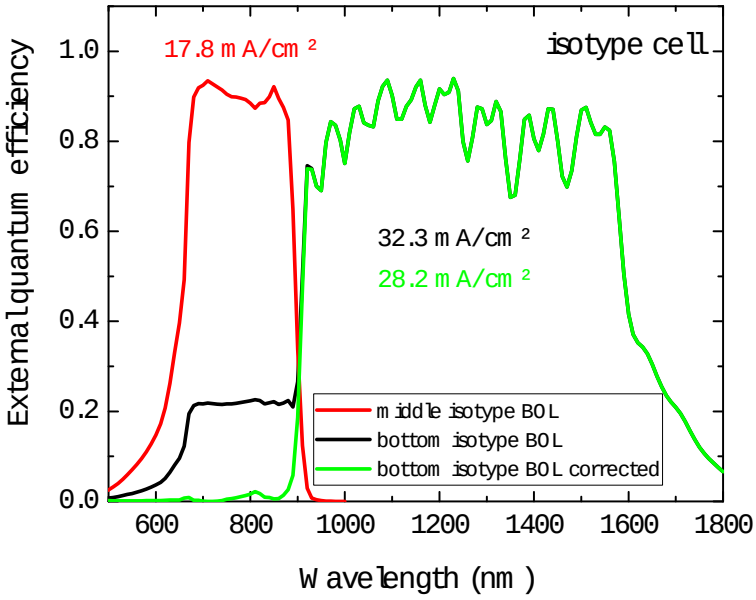

Figure 5.13 External quantum efficiency of 3G30 middle and bottom isotype cells.

The absolute degradation of all isotype cells is compared with the 3J cells in Fig. 5.14. At $17.9\,\frac{\text{mA}}{\text{cm}^2}$, the BOL value of the mid cells is higher than the top cell value of $17.1\,\frac{\text{mA}}{\text{cm}^2}$. This is the reason why at BOL up to a displacement damage dose of $1.1e10\,\frac{\text{MeV}}{\text{g}}$, the top subcell is current limiting in a 3J cell. For doses higher than $1.1e10\,\frac{\text{MeV}}{\text{g}}$, the middle cell is current limiting. The comparison shows that the short-circuit current of the 3J cell is higher than that of middle isotype cells for high doses. This is not a contradiction considering the cell internal working points of a 3J cell. While the 1J middle cell is measured at its short-circuit point of $V_{mid} = 0\,\text{V}$, the 3J cell is measured at the short-circuit point of the whole cell stack $V_{3J} = V_{top} + V_{mid} + V_{bot} = 0\,\text{V}$, but the individual subcells are not at $V_i = 0\,\text{V}$. Two conditions apply: firstly, equal current is extracted from all three subcells during measurement and secondly, the middle subcell is the radiation weakest cell. As a result of these conditions, at $V_{3J} = 0\,\text{V}$, the internal voltages V_{top} and V_{bot} are positive and V_{mid} is negative resulting in a sum of $V_{top}+V_{mid}+V_{bot} = 0\,\text{V}$. At a negative voltage of a cell, their current can lie beyond their short-circuit current. This is the case for the middle subcell during the measurement of the 3J cell, which is why the generated current is higher than the current generated by the isotype GaAs cell. The bottom cell generates BOL $31.5\,\frac{\text{mA}}{\text{cm}^2}$, which is a current almost twice as high as the other subcells. Therefore, the bottom cell is never current limiting. Due to the fact that the 3J cell is current limited by two different subcells depending on the displacement damage dose, the 3J degradation should strictly speaking

be fitted by two different degradation curves sectioned at $1.1e10\,\frac{\text{MeV}}{\text{g}}$. However, in this case the 3J data points show that the degradation behavior does not change significantly at $1.1e10\,\frac{\text{MeV}}{\text{g}}$. For other multi-junction cells with other material combinations, however, a sectioning of the degradation may be necessary at the dose where the limiting subcell changes.

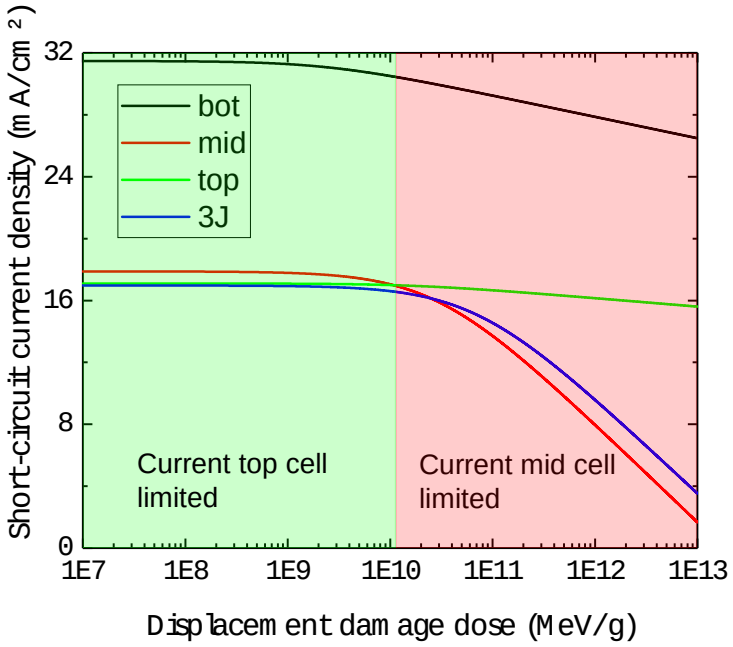

Figure 5.14 Comparison of the degradation of the short-circuit current of 3G30 isotype and 3J cells.

5.3.3 Influence of subcells on power at maximum power point

The power at maximum power point is shown in Figs. 5.15a-d. The top cell shows the least degradation compared to the other subcells. The middle cell shows the strongest degradation. It is important to note that the bottom cell data in Fig. 5.15c is not corrected for the effect of luminescent coupling. Firstly, the correction is not necessary because all charge carriers created by the middle cell of a 3J cell are extracted at the maximum power point and therefore no charge carriers are left for radiative recombination. Secondly, by EQE measurements such a correction is not possible for power because the degradation of the 3J cell results from the combination of all subcells.

All isotype cells are compared with the 3J cell in Fig. 5.16. The graph shows that the sum of the power of the subcells is higher than the power of the 3J cell. There are several reasons for this behavior. Firstly, luminescent coupling in the bottom isotype cell increases the power of the bottom isotype cell compared to the bottom subcell in a 3J cell. Contrary to a MJ cell, luminescent coupling in an isotype cell is present also

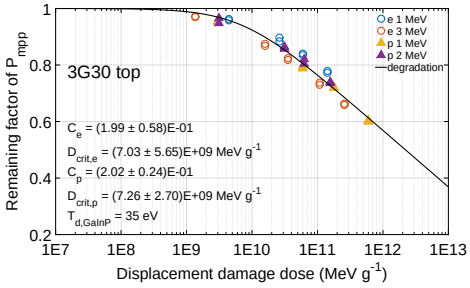

(a) Degradation of power at maximum power point of 3G30 isotype top cells.

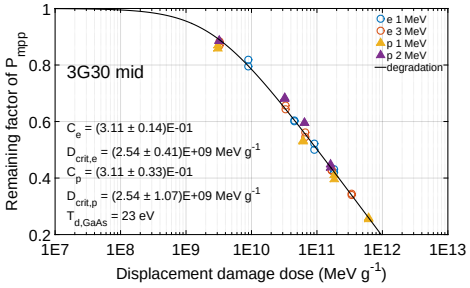

(b) Degradation of power at maximum power point of 3G30 isotype middle cells.

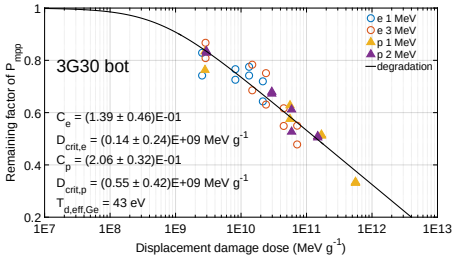

(c) Degradation of power at maximum power point of 3G30 isotype bottom cells.

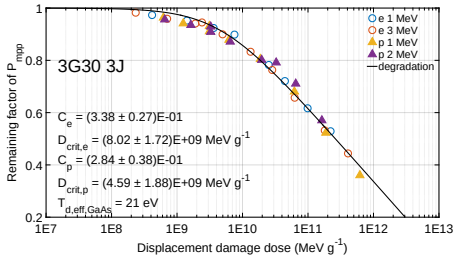

(d) Degradation of power at maximum power point of 3G30 triple-junction cells.

Figure 5.15 Degradation characteristics of power at maximum power point of 3G30 isotype and 3J cells.

at the maximum power point. Secondly, the maximum power point for each cell is at a different voltage and current. In a multi-junction cell, the current of all subcells has to be the same. Therefore, only one subcell, the subcell which creates the least current, operates at its maximum power point. The other subcells have to operate at this current and not at their respective maximum power points.

5.3.4 Analysis of subcell non-ionizing energy losses

Other than for MJ cells, the $T_{d,eff}$ resulting from the degradation analysis of single junction cells can clearly be attributed to the corresponding SJ materials. There is, however, the issue of how to include different threshold energies into NIEL calculations according to Bragg's rule. The NIELs of the single atomic species e.g. Ga and As are added up, which requires a separate $T_{d,eff}$ for each species. For this fitting procedure, the simplification of a common $T_{d,eff}$ is used which is reasonable for GaAs based upon earlier experimental evidence [64]. Threshold energies of $\sim 10\,\text{eV}$ are reported [64] for Ga or As atoms, respectively, in the GaAs lattice. The $T_{d,eff}$ of $21 - 22\,\text{eV}$ reproduced in this work matches the energy required for the formation of antisite defects in GaAs, ie. a Ga atom on an As lattice position and vice versa, very well. By molecular dynamic (MD) simulation, Mattila and Nieminen [65] found an appreciable rate of formation of this defect at an energy of the primary knock on atom of $20\,\text{eV}$. Since the irradiation

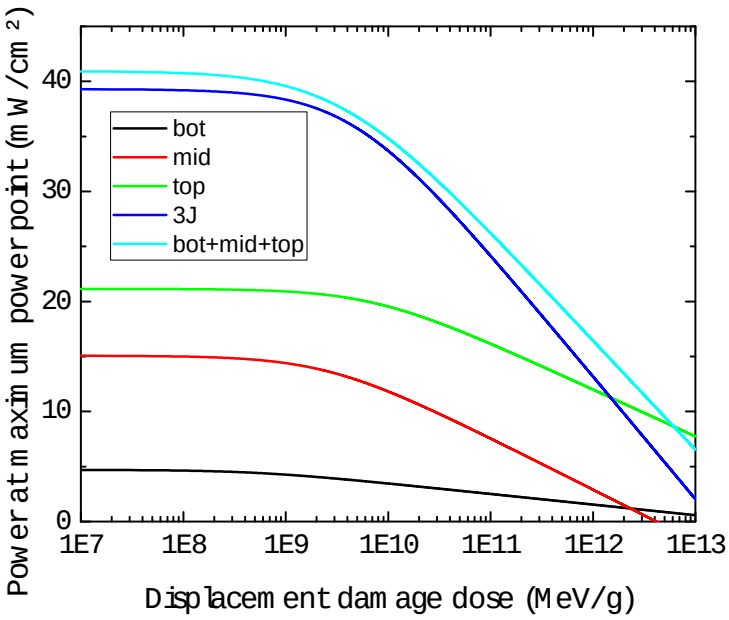

Figure 5.16 Comparison of the degradation of the power at maximum power point of 3G30 isotype and 3J cells.

of the cells is carried out at room temperature, followed by a 24 hour annealing step at $60\,^{\circ}\mathrm{C}$, there is sufficient mobility of point defects to anneal the lowest energy Frenkel defect. Therefore, the effective threshold energy for the creation of electrically active defects determined from the room temperature degradation data is higher.

In $Ga_{0.5}In_{0.5}P$, the situation is similar in that the $T_{d,eff}$ determined is considerably higher than the energy reported in the literature for the formation of Frenkel pairs in Ga of $T_{d,Ga} = 9 - 10\,\mathrm{eV}$, in In $T_{d,In} = 3 - 6.7\,\mathrm{eV}$, and $T_{d,P} = 8 - 8.7\,\mathrm{eV}$ for P [64, 66–68]. This raises some fundamental difficulties, since the lowest energy defect at the irradiation temperature has to contain more than one atomic species. Once the degradation fitting has yielded a joint threshold displacement energy, it is possible to determine different combinations of T_d for the different constituents that result in the same NIEL as a function of energy for the overall crystal. For example, in $Ga_{0.5}In_{0.5}P$, $T_{d,eff}$ of $21\,\mathrm{eV}$ for Ga, $20\,\mathrm{eV}$ for In and $45\,\mathrm{eV}$ for P would result in the same NIEL as the common threshold displacement energy of $36\,\mathrm{eV}$. In particular if the lowest energy defect does not involve one atomic species, a higher threshold displacement energy for this species results automatically. In this case, the incoming particle has to provide not only the energy to displace the primary knock on atom but also the energy for this atom to subsequently transfer its energy to one of the other species involved in the lowest energy defect. Once possible candidates for the lowest energy defects have been identified by other means, for example by molecular dynamics simulations, it is possible to determine whether they fit to the $T_{d,eff}$ determined from the degradation fitting.

It is *a priori* not obvious whether it is justified to only use the GaAs NIEL in performing the degradation fits of 3J cells. To determine whether the NIEL of the top cell material is also suited to fit the 3J cell, the degradation fit of the 3G28 cell is repeated with the NIEL of $Ga_{0.5}In_{0.5}P$. The result is shown in Fig. 5.17. The fit is approximately equal to the fit of the same data with GaAs-NIEL shown in Fig. 5.4. A $T_{d,eff}$ of $36\,\mathrm{eV}$ is obtained, which is well in line with the result obtained on top component cells in sec. 5.3. The fit of the data points works well either with $Ga_{0.5}In_{0.5}P$-NIEL or with GaAs-NIEL. The reason behind this is that the NIEL values are approximately equal. These data provide some justification as to why either the NIEL of the GaAs middle cell or the NIEL of the $Ga_{0.5}In_{0.5}P$ top cell can be used with adapted threshold energies for atomic displacement.

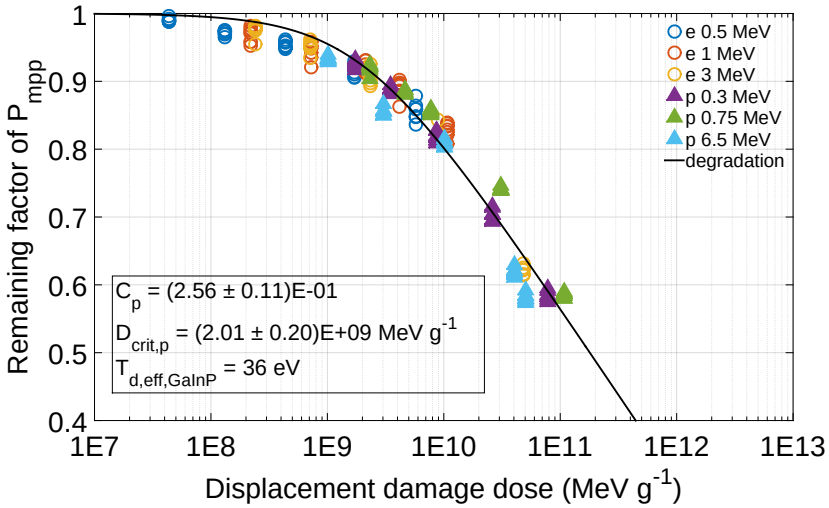

Figure 5.17 Degradation of the power at maximum power point of 3G28 3J cells by using the top cell NIEL.

5.4 Conclusion

In this section, a fitting method to analyze solar cell particle irradiation data was introduced. The method consists of a combination of the displacement damage dose method and using the threshold energy for atomic displacement as a fit parameter. It is possible to use the threshold energy for atomic displacement as a fit parameter which is only dependent on the material of the cell. This results in a collapse of the different electron energy data points. The method is described in detail and its experimental requirements and boundaries are discussed. Moreover, the use of the method for multijunction cells is discussed. The method is verified by comparing data analysis results of the D_d method with threshold energy for atomic displacement to results of the D_d method with exponent n for the same data set.

3G30 top isotype cell	V_{oc}	I_{sc}	P_{mpp}
C_e	0.083 ± 0.021	0.192 ± 0.122	0.199 ± 0.058
$D_{crit,e}\,(10^9\,\frac{\text{MeV}}{\text{g}})$	3.01 ± 2.44	222.3 ± 210.8	7.03 ± 5.65
C_p	0.083 ± 0.009	0.194 ± 0.071	0.202 ± 0.024
$D_{crit,p}\,(10^9\,\frac{\text{MeV}}{\text{g}})$	3.00 ± 1.18	225.3 ± 128.1	7.26 ± 2.70
$T_{d,eff}$	35	35	35

Table 5.2 Comparison of the 3G30 top cell fit parameters of the electrical cell parameters open-circuit voltage, short-circuit current and power at maximum power point. The fit parameters are determined with the NRL method where the D_d is calculated by adapting the $T_{d,eff}$. The NIEL was calculated based on $Ga_{0.5}In_{0.5}P$.

Furthermore, the method was used to analyze a large data set of particle irradiated solar cell data of 3J cells and its three corresponding 1J isotype cells. The results are discussed with regard to the impact of the individual subcell degradation on the 3J cell degradation. Comparisons of the 3J degradation data to the 1J degradation data are discussed and the electrical behavior of 3J cells can be reproduced well by combining the results of the three isotypes.

3G30 mid isotype cell	V_{oc}	I_{sc}	P_{mpp}
C_e	0.130 ± 0.013	0.355 ± 0.026	0.311 ± 0.014
$D_{crit,e}\,(10^9\,\frac{\text{MeV}}{\text{g}})$	1.27 ± 0.47	28.16 ± 4.94	2.54 ± 0.41
C_p	0.129 ± 0.015	0.356 ± 0.061	0.311 ± 0.033
$D_{crit,p}\,(10^9\,\frac{\text{MeV}}{\text{g}})$	1.24 ± 0.61	28.45 ± 11.57	2.54 ± 1.07
$T_{d,eff}$	23	21	23

Table 5.3 Comparison of the 3G30 mid cell fit parameters of the electrical cell parameters open-circuit voltage, short-circuit current, and power at maximum power point. The fit parameters are determined with the NRL method where the D_d is calculated by adapting the $T_{d,eff}$. The NIEL is calculated based on GaAs.

3G30 bot isotype cell	V_{oc}	I_{sc}	P_{mpp}
C_e	0.178 ± 0.036	0.046 ± 0.170	0.139 ± 0.046
$D_{crit,e}\,(10^9\,\frac{\text{MeV}}{\text{g}})$	10.99 ± 5.21	2.77 ± 24.27	0.14 ± 0.24
C_p	0.216 ± 0.029	0.044 ± 0.049	0.206 ± 0.032
$D_{crit,p}\,(10^9\,\frac{\text{MeV}}{\text{g}})$	9.25 ± 3.69	2.48 ± 10.70	0.55 ± 0.42
$T_{d,eff}$	40	37	43

Table 5.4 Comparison of the 3G30 bot cell fit parameters of the electrical cell parameters open-circuit voltage, short-circuit current and power at maximum power point. The fit parameters are determined with the NRL method where the D_d is calculated by adapting the $T_{d,eff}$. The NIEL is calculated based on Ge.

In the Tables 5.2 to 5.5, the results of the degradation analysis of the top, middle, bottom, and 3J 3G30 cell types are summarized. The threshold energy for atomic displacement found for the top cell material $Ga_{0.5}In_{0.5}P$ is $35\,\text{eV}$. For the GaAs middle cell, a threshold energy of $20 - 21\,\text{eV}$ is found, which is in agreement with [58]. The Ge bottom cell value is found to be in the range of $37 - 43\,\text{eV}$. Comparing the fit curve parameters of the electron and proton slopes C_e and C_p, it is found that the values are in good agreement to each other for the top, middle, and 3J cell. The same agreement is true for the parameters $D_{crit,e}$ and $D_{crit,p}$. This means that the cells react similarly to proton and to electron irradiation. A distinct degradation behavior of the V_{oc} of the bottom cell is found, but the I_{sc} results were ambiguous. It is shown that the BOL values of the bottom cell have to be corrected before doing the degradation analysis to compensate the effect of luminescent coupling.

3G30 3J cell	V_{oc}	I_{sc}	P_{mpp}
C_e	0.070 ± 0.010	0.285 ± 0.055	0.338 ± 0.027
$D_{crit,e}\,(10^9\,\frac{\text{MeV}}{\text{g}})$	0.89 ± 0.50	22.87 ± 9.76	8.02 ± 1.72
C_p	0.093 ± 0.008	0.366 ± 0.080	0.284 ± 0.038
$D_{crit,p}\,(10^9\,\frac{\text{MeV}}{\text{g}})$	1.08 ± 0.37	69.00 ± 29.41	4.59 ± 1.88
$T_{d,eff}$	20	21	21

Table 5.5 Comparison of the 3G30 3J cell fit parameters of the electrical cell parameters open-circuit voltage, short-circuit current, and power at maximum power point. The fit parameters are determined with the NRL method where the D_d is calculated by adapting the $T_{d,eff}$. The NIEL is calculated based on GaAs.

6 Voltage dependent photocurrent in irradiated GaAs cells

Parts of this chapter are published in [69].

6.1 Introduction

In the last chapter, photocurrents dependent on particle irradiation generated by individual subcells were investigated. In this chapter, the current generation within one individual subcell will be investigated more thoroughly. It has been established in the last chapter that in current $Ga_{0.5}In_{0.5}P/GaAs/Ge$ triple junction cells used almost exclusively in space, the GaAs middle cell is the most sensitive one in terms of radiation [70,71]. We will show that when these subcells are exposed to fluences in the range from $1-10\times10^{15}$ 1 and 3 MeV electrons/cm^2 or to $1 - 10 \times 10^{12}$ 1 MeV protons/cm^2, their photocurrent becomes voltage dependent even at room temperature. Voltage-dependent photocurrent *per se* is not a new effect. It has been observed in a-Si, a-SiGe [72] and CdTe/CdS [73] solar cells, where the dependence was attributed to field-assisted drift in the depletion region, a model developed for p-i-n solar cells. The phenomenon was also found in CuInSe/Cd(Zn)S cells where it was explained by a field-dependent interface recombination at the heterojunction interface [74]. In multi-quantum well solar cells, the voltage dependence was found to originate from carrier removal in the quasi-intrinsic region [75]. At temperatures well below room temperature, a voltage-dependent photocurrent was observed in proton-irradiated $Ga_{0.5}In_{0.5}P/GaAs/Ge$ triple junction, GaAs, and $Ga_{0.5}In_{0.5}P$ single junction cells [76].

For irradiated III-V cells at room temperature, however, this effect has never been observed before. We will show that it can be fully explained by a mechanism suggested by Liu et al. [77] in a different context: By the voltage-dependent width of the space charge region in combination with a short minority carrier diffusion length.

GaAs single junction isotype cells, 2×2 cm^2 in size, are used in the irradiation campaign. They are fully representative of the middle cell in current 30% triple junction $Ga_{0.5}In_{0.5}P/GaAs/Ge$ cells as described in chapter 3.1. The remaining subcells are included in the device as well to provide the representative optical filtering of the incident spectrum. No p-n junction is formed, however, thus the GaAs junction is the only elec-

trically active one. The n-doped emitter is approximately $100\,\text{nm}$ thick, with a doping density of $1 \times 10^{18} \frac{1}{cm^3}$. The base is p doped to $5 \times 10^{16} \frac{1}{cm^3}$ with a physical thickness of $1400\,\text{nm}$. Due to a rearside reflector, the effective optical thickness is twice as much. The samples were irradiated with different fluences of electrons and protons at TU Delft and CSNSM Orsay as shown in Table 6.1. One sample was used per fluence and particle type. No cumulative irradiation of the same sample was performed. The samples were irradiated with a flux of $1.5 \times 10^{12} \frac{e}{cm^2 s}$ for electrons and $5.7 \times 10^{10} \frac{p}{cm^2 s}$ for protons with the exception of the lowest proton fluence, which was applied at a rate of $1.9 \times 10^{9} \frac{p}{cm^2 s}$. The cell temperature was monitored and did not exceed room temperature during irradiation. To exclude any subsequent time-dependent annealing effects during measurements, all cells were exposed to an annealing regime of 48 h at 25°C and one sun AM0 illumination, followed by 24 h at 60°C in the dark. This represents the standard process in Europe for industrially used space solar cells [17].

electrons 1 MeV ϕ (cm^{-2})	electrons 3 MeV ϕ (cm^{-2})	protons 1 MeV ϕ (cm^{-2})
1e15	1e14	5e10
5e16	1e15	1e12
1e16	2e15	3e12
2e16	5e15	1e13
	1e16	

Table 6.1 Particles, energies and fluences used in irradiating the GaAs isotype cells.

6.2 Classical model of photocurrent

One of the most basic cell characterization techniques is the DIV measurement. The DIV data of the $3\,\text{MeV}$ electron-irradiated GaAs cells are shown in Fig. 6.1. The behavior of the DIV data for the 1 MeV proton as well as the 1 MeV electron irradiation are qualitatively similar. Since this applies also to the LIV, CV, and EQE data, the analysis and discussion in the following is focused exemplarily on the $3\,\text{MeV}$ electron data.

$$I = I_{01} \cdot (e^{\frac{eV}{k_B T}} - 1) + I_{02} \cdot (e^{\frac{eV}{nk_B T}} - 1) + \frac{V}{R_p} \tag{6.1}$$

To quantify the DIV data and to extract the basic cell parameters, a two diode model according to Eq. 6.1 is fitted to the measured data [78]. Recombination in the quasi-neutral n-type and p-type regions is taken into account by the current density I_{01}, and recombination in the space charge region (SCR) is quantified by I_{02}. The series resistance R_s of the cells is negligible and therefore not necessary for the data fitting.

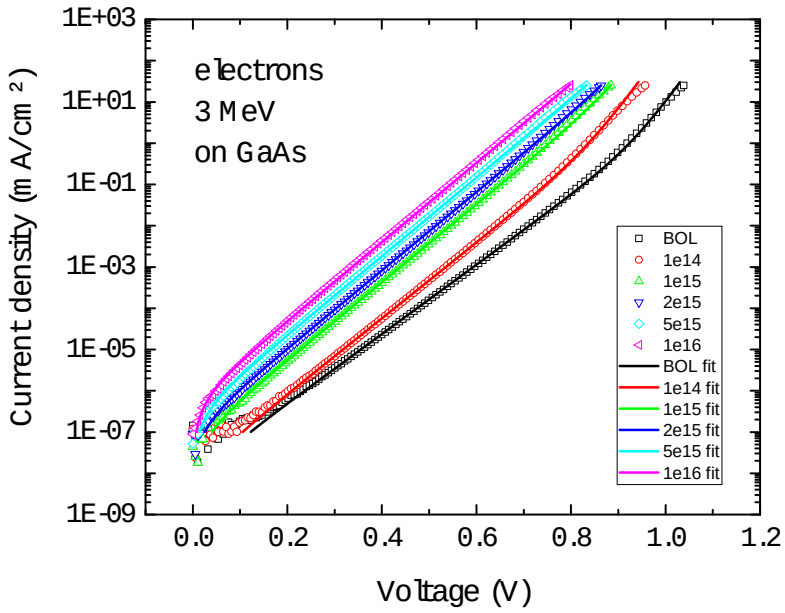

Figure 6.1 Dark current-voltage characteristics of GaAs isotype cells irradiated with 3 MeV electrons.

For a single-level recombination center in the SCR in an idealized cell, the ideality factor n equals 2. If different lifetimes of electrons and protons, a variable recombination rate throughout the SCR or a defect level which is not in the middle of the band gap are taken into account, the ideality factor n is predicted to lie between 1 and 2 [78, 79]. Therefore, the ideality factor is used as a fit parameter in the DIV data fitting. I is the measured current, V the applied voltage, k_B the Boltzmann constant, R_p the shunt resistance, and T the temperature.

The resulting fits to the measured DIV data are included in Fig. 6.1 and the fit parameters I_{01}, I_{02} and n are summarized in Table 6.2. The recombination current densities I_{01} and I_{02} increase as the irradiation fluence increases due to the creation of additional recombination centers. The ideality factor of the non irradiated cells is 2 and slightly decreases with irradiation to 1.74 for the highest fluence. Irradiation can cause different defects like vacancies, interstitials, and antisites. A cause for the change of n could be additional defects introduced through irradiation with energy levels not in the middle of the band gap as observed by Pons et al. [59]. A matter of technical difficulty has to be pointed out here: The I_{01} current dominates the total dark current from approximately 0.8 V onwards. The cells, however, are only operated up to a maximum total current of 100 mA to prevent damage to the cell, therefore the fitting of I_{01} is only possible for the non-irradiated cells and cells with low irradiation fluence. The inclusion of a shunt resistance R_p is not necessary for any of the GaAs cells.

ϕ (cm^{-2})	I_{01} ($\frac{mA}{cm^2}$)	I_{02} ($\frac{mA}{cm^2}$)	n
0	1.0e-16	1.3e-8	2.0
1e14	3.6e-15	1.2e-8	1.83
1e15	1.3e-14	7.1e-8	1.78
2e15	1.4e-14	1.3e-7	1.77
5e15	ND	2.8e-7	1.76
1e16	ND	5.9e-7	1.74

Table 6.2 Dark current-voltage fit parameters of GaAs cells after irradiation with $3\,$MeV electrons.

Recently, a deviation from the ideal two-diode model in the DIV curve was reported for electron-irradiated triple junction, $Ga_{0.5}In_{0.5}P$ and Ge cells at a temperature of $123\,$K [80]. The increase in the dark current observed under these low intensity and low temperature (LILT) conditions was attributed to tunnel assisted recombination in the space charge region [81]. Therefore, it is of interest to check whether a similar effect can be observed for the GaAs cells in this study as well.

Tunneling assisted recombination is characterized by a temperature dependence of the ideality factor $n_{tunnelrec}$ according to Eq. 6.2 [81]. The DIV curves are thus measured at various temperatures from room temperature down to $90\,$K. By fitting the data according to Eq. 6.1, the ideality factor n is derived. The results are shown in Fig. 6.2 for various temperatures. The ideality factor of the non-irradiated cell is constant at a value around 2 and begins to increase with $\frac{1}{T}$ at temperatures below $250\,$K. The irradiated cells show an onset of a tunneling current at temperatures below $180\,$K. Therefore, these results provide another confirmation that under LILT conditions tunneling assisted recombination is a contribution that has to be taken into account in modeling the DIV curve. At the same time they confirm that at room temperature the DIV fit to a classical 2 diode model is justified.

$$n_{tunnelrec} \propto \frac{1}{T} \tag{6.2}$$

The measured LIV curves are shown in Fig. 6.3. Especially for the higher fluences, a slope in the curves is visible resembling a typical shunt resistance. A shunt resistance, however, would also be visible in the DIV data and the presence of shunts was excluded there already. In order to clarify the origin of this slope, simulated LIV curves are constructed from the DIV data according to Eq. 6.3, which makes use of the fact that the shunt resistances were found negligible. I_{01}, I_{02} and n are taken from the DIV fit and the short circuit current obtained in the LIV measurement is used for the photocurrent term I_L. The simulated LIV curves have been included in Fig. 6.3 as well. In the steep part of the IV curve, the match between measured LIV and simulated

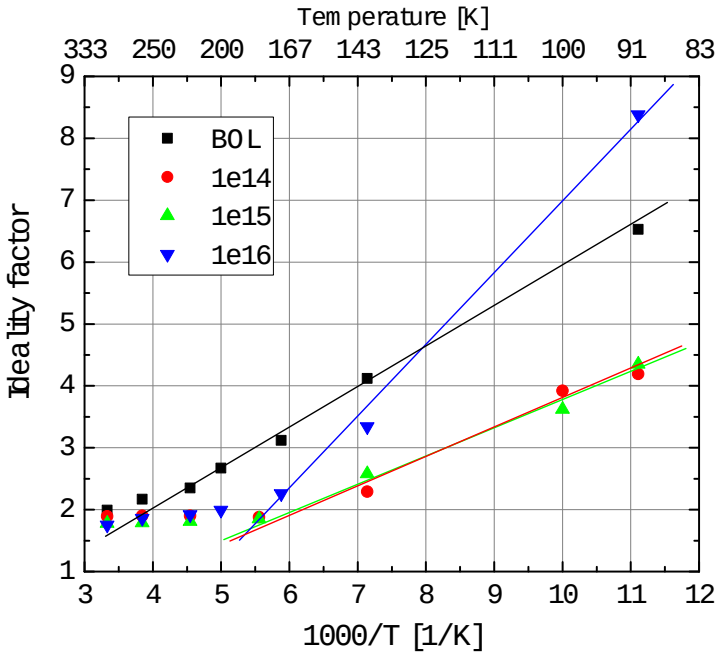

Figure 6.2 Diode ideality factor, extracted from DIV curves, as a function of temperature.

IV curve is quite good, the small deviations are due to distributed series resistance effects [82], which result in different current distributions in the illuminated and the dark state. They cannot be taken into account easily except through the use of two-dimensional numerical network modeling, which is not the focus of this work. The large deviations in the horizontal part of the curve, however, can only be explained by a voltage-dependent photocurrent. In Fig. 6.4, the difference between the measured LIV curve and the simulated LIV curve is illustrated. The voltage-dependent effect amounts to approximately 10% of the total photocurrent in case of the highest radiation fluence.

$$I = I_L - I_{01} \cdot (e^{\frac{eV}{k_B T}} - 1) - I_{02} \cdot (e^{\frac{eV}{nk_B T}} - 1) \tag{6.3}$$

6.3 Modified model of photocurrent including voltage dependence

We argue, as suggested in Ref. [77], that the reason for the voltage-dependent photocurrent is the voltage dependence of the width of the space charge region W_{SCR}. This dependence is negligible for cells in which the minority carrier diffusion length L_p in the emitter and L_n in the base is much larger than the emitter and base thickness of the cell, respectively. In this case, all electron-hole pairs, no matter if they are generated in the SCR or somewhere in the bulk, are collected. This is the case for non-irradiated cells

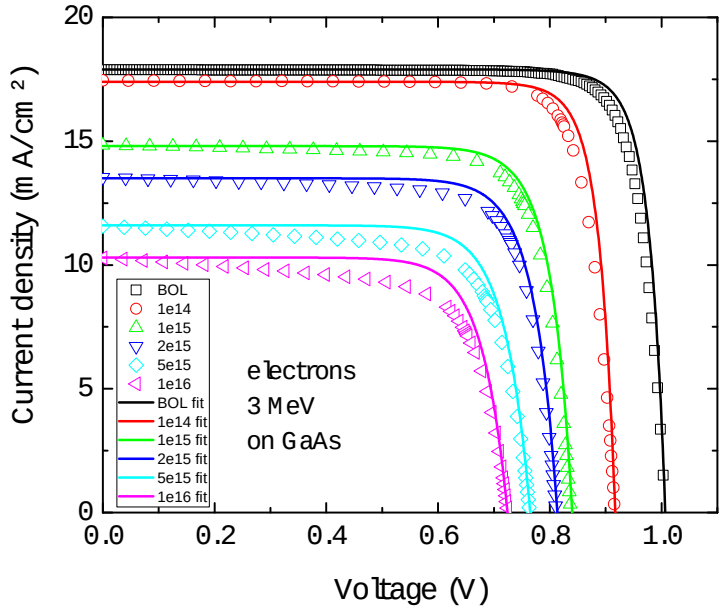

Figure 6.3 Light current-voltage characteristics of electron-irradiated GaAs cells. The curves are simulated with the parameters gained from the DIV fits and a constant photocurrent.

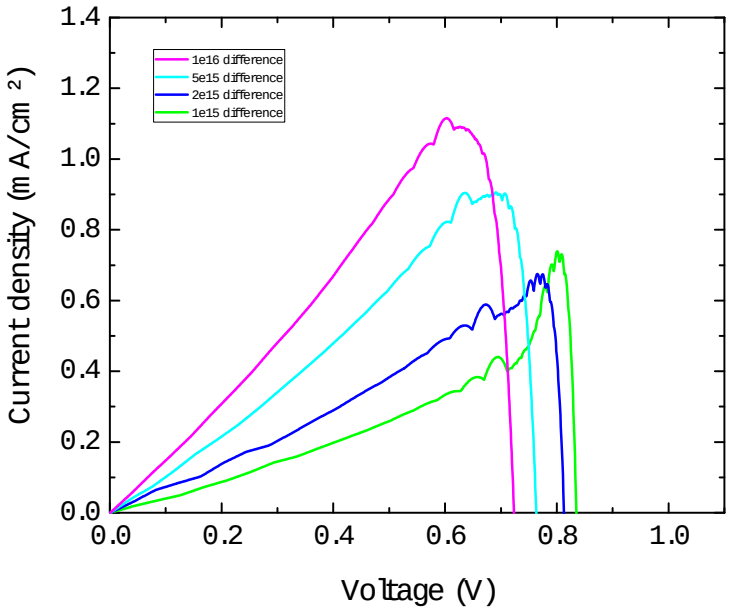

Figure 6.4 The difference in current between the simulated curve and the measurement data.

or cells which are irradiated with low fluences. This situation is illustrated graphically in Fig. 6.5a.

The effect is not negligible, however, if the diffusion length decreases so much that the sum $L_p + W_{SCR}(V) + L_n$ is smaller than the cell thickness. This is the case for irradiation with high fluences. The case of a highly irradiated cell under short circuit con-

ditions is illustrated in Fig. 6.5b. The SCR width takes on its maximum, so the volume where photocurrent is collected efficiently also reaches a maximum. The collection efficiency outside of the SCR decreases exponentially with diffusion length, independently of voltage. For operating conditions with $V > 0$ away from short circuit conditions, as illustrated in Fig. 6.5c, W_{SCR} decreases and with it the total photocurrent.

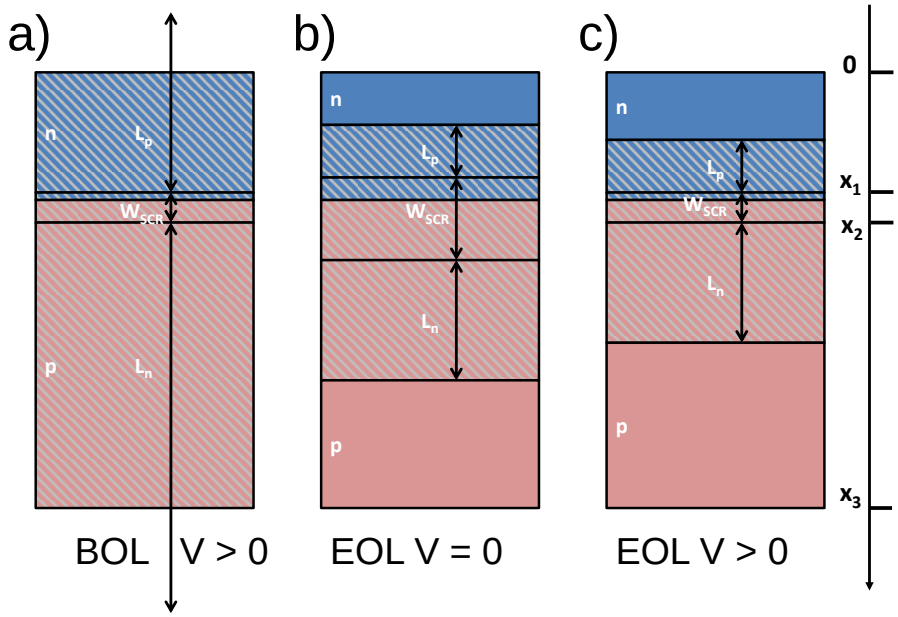

Figure 6.5 Illustration of an (a) unirradiated cell (b) an irradiated cell under short circuit conditions and (c) an irradiated cell under forward bias. The areas where photocurrent is collected efficiently are shaded.

The overall photocurrent is a sum of the currents generated in the emitter, I_p, the SCR, $I_{W_{SCR}}$, and the base, I_n. The generation rate of electron hole pairs at a distance x from the surface is given by $\alpha\Phi_0 e^{-\alpha x}$, where α is the absorption coefficient and Φ_0 the photon flux at the surface. The situation is simplified by not treating the wavelength dependence explicitly. Thus, an average absorption coefficient is used. In the isotype cells, both front and rear surfaces are effectively passivated, so recombinations at the front and rear surfaces are neglected. The individual current contributions can therefore be derived by integrating the generation rate with the probability of collecting an electron-hole pair P_{coll}:

$$I = e\Phi_0\alpha \int e^{-\alpha x} P_{coll}(x)\,\mathrm{d}x. \tag{6.4}$$

In the emitter, the collection probability depends exponentially on the distance $x - x_1$ of the location x of the electron-hole pair generation from the location x_1 of the SCR according to $P_{coll} = e^{-\frac{x_1 - x}{L_p}}$. Thus Eq. 6.4 yields

$$I_p = e\Phi_0 \frac{\alpha L_p}{\alpha L_p - 1}(e^{-\frac{x_1}{L_p}} - e^{-\alpha x_1}). \tag{6.5}$$

Due to the strong electrical field, all electron-hole pairs in the SCR are collected with $P_{coll} = 1$. Integrating Eq. 6.4 from x_1 to the boundary x_2 of the SCR yields $I_{W_{SCR}}$:

$$I_{W_{SCR}} = e\Phi_0 e^{-\alpha x_1}(1 - e^{-\alpha W_{SCR}}). \tag{6.6}$$

In the base layer, the collection probability again depends exponentially on the distance of the electron hole generation from the SCR according to $P_{coll} = e^{-\frac{x-x_2}{L_n}}$. Integrating Eq. 6.4 from x_2 to the bottom of the base layer x_3 and making use of the fact that $\alpha x_3 >> 1$ yields the current in the base I_n

$$I_n = e\Phi_0 e^{-\alpha x_1} \frac{\alpha L_n}{1 + \alpha L_n} e^{-\alpha W_{SCR}}. \tag{6.7}$$

The resulting overall photocurrent I_L is the sum of the three contributions I_p, $I_{W_{SCR}}$ and I_n. Combining Eqs. 6.5, 6.6 and 6.7 results in

$$I_L = e\Phi_0 \left(\frac{\alpha L_p}{\alpha L_p - 1}(e^{-\frac{x_1}{L_p}} - e^{-\alpha x_1}) + e^{-\alpha x_1} \left(1 - \frac{e^{-\alpha W_{SCR}}}{1 + \alpha L_n} \right) \right). \tag{6.8}$$

Due to the fact that the emitter is heavier doped than the base, the bulk of the SCR stretches into the base. Therefore, the voltage dependence of x_1 is small. It affects the respective exponential term in Eqs. 6.5, 6.6, and 6.7 by less than 1%. Therefore, it is neglected in the following and a constant emitter thickness x_1 of 100 nm is used. The only voltage dependence in Eq. 6.8 then enters through the effect of the voltage dependence of W_{SCR}. The current-voltage equation for cells under illumination can now be written as the sum of the voltage-dependent photocurrent according to Eq. 6.8 and the recombination current according to Eq. 6.1.

$$I = e\Phi_0 \left(\frac{\alpha L_p}{\alpha L_p - 1}(e^{-\frac{x_1}{L_p}} - e^{-\alpha x_1}) + e^{-\alpha x_1} \left(1 - \frac{e^{-\alpha W_{SCR}(V)}}{1 + \alpha L_n} \right) \right) - I_{01} \cdot (e^{\frac{eV}{k_B T}} - 1) - I_{02} \cdot (e^{\frac{eV}{nk_B T}} - 1) \tag{6.9}$$

The new voltage-dependent term in Eq. 6.9, $W_{SCR}(V)$, is given by

$$W_{SCR}(V) = \sqrt{\frac{2\epsilon(V_b - V)}{eN_A}} \tag{6.10}$$

approximating the junction as an abrupt n^+p-junction with a base doping density of N_A and a built-in voltage V_b [9]. ϵ denotes the permittivity of the semiconductor.

In order to calculate the LIV curves according to Eqs. 6.9 and 6.10, the unknown parameters have to be determined by separate DIV, CV, and EQE measurements. The base layer doping N_A as well as the built-in voltage V_b can be extracted from capacitance

voltage measurements. In Fig. 6.6, $1/C^2$, where C denotes the capacitance per unit area, is plotted as a function of voltage. According to Eq. 6.11, the built-in voltage can be derived from the intersection of the curve with the x axis and the doping density from the slope of the curve [9].

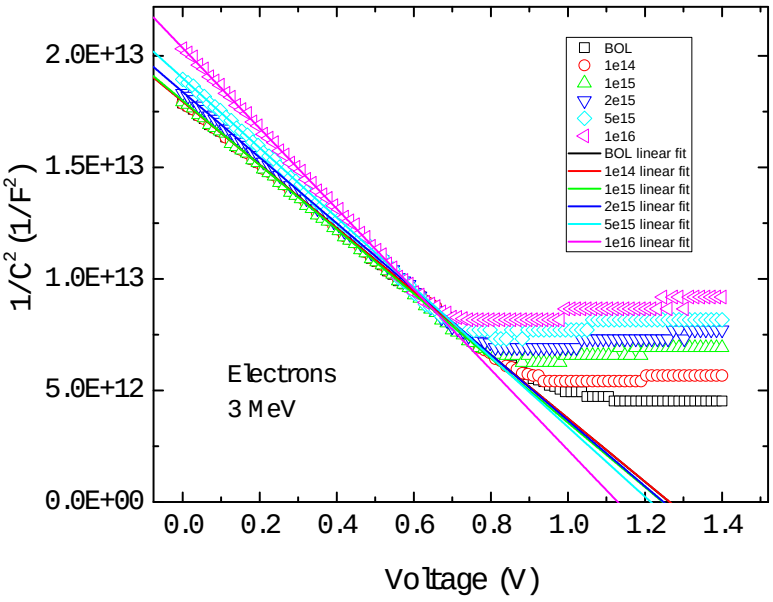

Figure 6.6 Capacitance voltage measurements of the irradiated GaAs cells.

$$\frac{1}{C^2} = \frac{2(V_b - V - \frac{2k_BT}{e})}{e\epsilon N_A} \tag{6.11}$$

The diffusion length L_p and L_n in emitter and base were determined by fitting the external quantum efficiency data of the cells [9], again neglecting recombination at surfaces. The shorter wavelength efficiency is highly sensitive to L_p. The longer wavelength efficiency is sensitive to L_n. The measured EQE and the simulated EQE are shown in Fig. 6.7. The solid lines represent the measurement data, the simulation results are shown as dashed lines. For the high irradiation data the simulated EQE fits the slope of the measured EQE quite well. The simulation of the EQE included a simulation of the rearside reflector of the cell. Without this addition, the EQE of the BOL cell and the cells irradiated with low fluences would be underestimated in the long wavelength region between 800 and $900\,\mathrm{nm}$.

Table 6.3 summarizes the parameters determined from the CV and the EQE measurements. The ideality factors n and saturation current densities are again taken from Table 6.2. A permittivity ϵ of $12.9\epsilon_0$ is used, with $\epsilon_0 = 8.85 \times 10^{-}12$ As/Vm. An average absorption coefficient of GaAs of $\alpha = 2e6\frac{1}{\mathrm{m}}$ in the wavelength range 650 - $900\,\mathrm{nm}$ is chosen. This is the relevant wavelength range in question according to Fig.

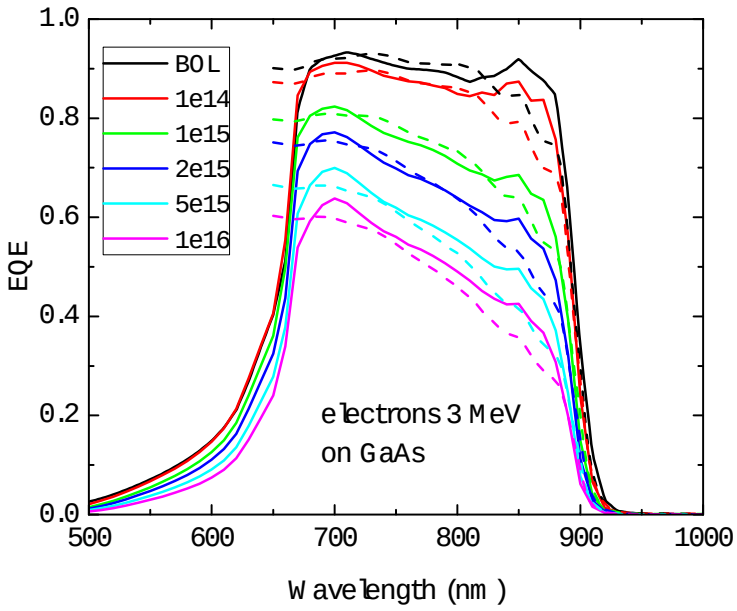

Figure 6.7 External quantum efficiency measurements of the irradiated GaAs cells.

6.7. The photon flux Φ_0 is adjusted such that Eq. 6.8 yielded in the non-irradiated case the experimentally measured short circuit current of $18\,\frac{\text{mA}}{\text{cm}^2}$ according to Fig. 6.3. This resulted in $\Phi_0 = 1.22 \times 10^{17}\text{cm}^{-2}\text{s}^{-1}$. The BOL diffusion length of $8\,\mu$m agrees well with the BOL values of $6-7\,\mu$m found in GaAs cells by Niemeyer et al. and Yamaguchi et al. [83, 84].

With these parameters, Eq. 6.9 matches the measured current-voltage curves for all electron fluences exactly without the need for any further adjustments. The simulated curves are shown in Fig. 6.8 together with the measurement data. These results confirm that a voltage-dependent photocurrent observed at room temperature in irradiated GaAs cells is due to a voltage-dependent width of the space charge region in combination with a significantly reduced minority carrier diffusion length.

ϕ (cm^{-2})	N_A ($\frac{1}{cm^3}$)	V_b (V)	L_n (μm)	L_p (μm)
0	4.8e16	1.32	8.0	0.15
1e14	4.8e16	1.31	6.0	0.11
1e15	4.7e16	1.30	1.4	0.060
2e15	4.6e16	1.30	0.85	0.050
5e15	4.4e16	1.26	0.48	0.032
1e16	3.8e16	1.18	0.33	0.020

Table 6.3 Base doping density, built-in voltage, and base and emitter diffusion length of GaAs cells after irradiation with 3 MeV electrons.

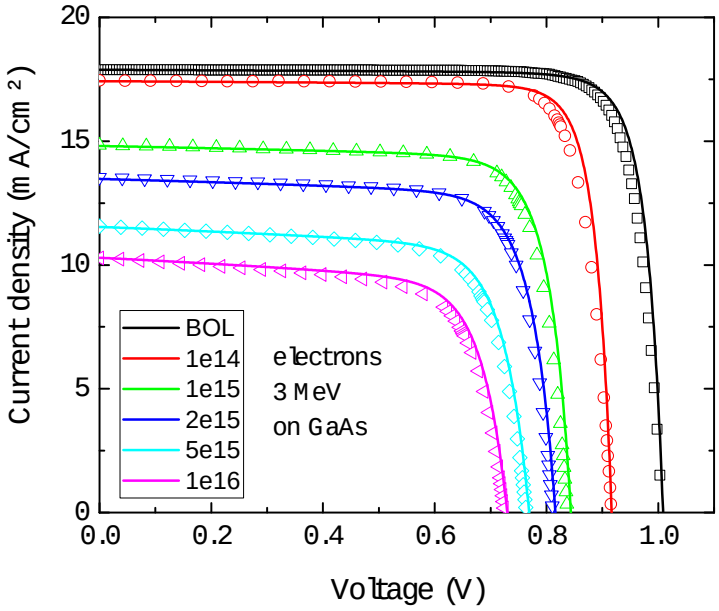

Figure 6.8 Light I-V data (open symbols) of GaAs cells irradiated with 3 MeV electrons and the calculated curves according to Eq. 6.9 (solid lines).

The same analysis is performed for the other sample groups as well, which are irradiated with electrons with an energy of 1 MeV and protons with 1 MeV energy shown in Figs. 6.9 and 6.10. Again, the observed voltage-dependent photocurrent in the LIV measurements can be reproduced by Eq. 6.9.

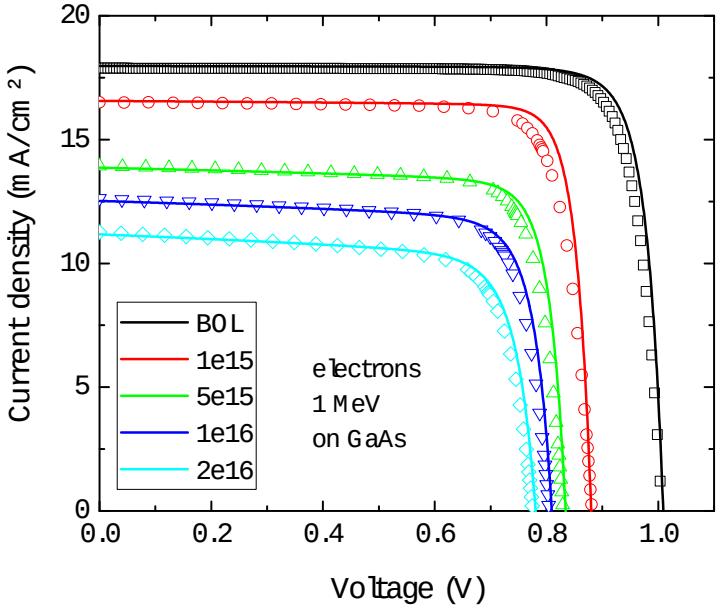

Figure 6.9 Light I-V data (open symbols) of GaAs cells irradiated with 1 MeV electrons and the calculated curves according to Eq. 6.9 (solid lines).

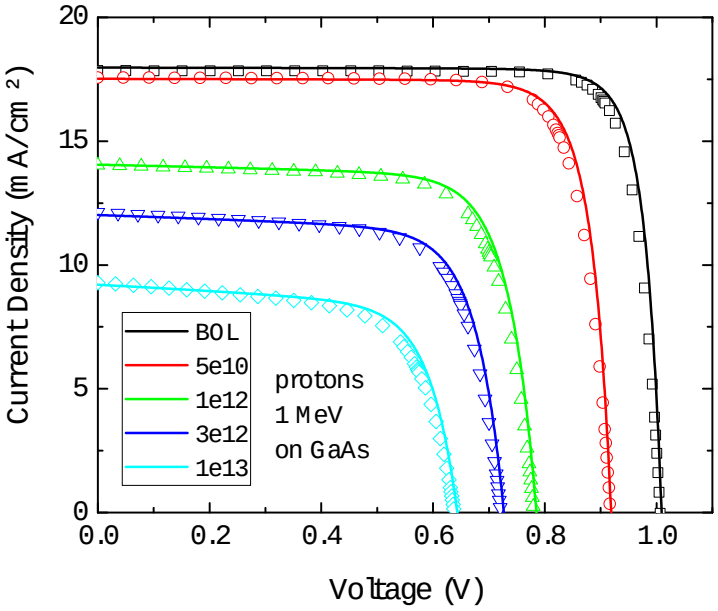

Figure 6.10 Light I-V data (open symbols) of GaAs cells irradiated with 1 MeV protons and the calculated curves according to Eq. 6.9 (solid lines).

The cell parameters obtained for these cases are summarized in Tab. 6.4.

particle	ϕ (cm^{-2})	I_{01} $(\frac{mA}{cm^2})$	I_{02} $(\frac{mA}{cm^2})$	n	N_A $(\frac{1}{cm^3})$	V_b (V)	L_n $(\mu$m)	L_p $(\mu$m)
	1e15	1.70e-14	2.44e-8	1.95	4.82e16	1.30	4.4	0.06
electrons	5e15	6.88e-14	5.96e-8	1.85	4.67e16	1.28	1.0	0.05
1 MeV	1e16	8.12e-14	1.13e-7	1.83	4.57e16	1.25	0.65	0.04
	2e16	1.31e-13	1.91e-7	1.81	4.37e16	1.23	0.42	0.03
	5e10	2.02e-15	7.37e-8	1.93	4.84e16	1.33	7.5	0.10
protons	1e12	ND	1.03e-6	1.90	4.81e16	1.32	1.0	0.06
1 MeV	3e12	ND	2.80e-6	1.90	4.60e16	1.30	0.52	0.04
	1e13	ND	9.42e-6	1.89	3.95e16	1.21	0.24	0.01

Table 6.4 Fit parameters of GaAs isotype cells irradiated with 1 MeV electrons and 1 MeV protons.

6.4 Behavior of cell parameters under irradiation

In order to analyze if and how the cell parameter degradation depends on particle type and energy, different parameters are plotted as function of the displacement damage dose (D_d). First of all, the minority carrier diffusion length in the base is plotted in Fig. 6.11. The D_d is calculated by multiplying the particle fluences with the non-ionizing

energy loss (NIEL) of protons and electrons of the respective energies. In calculating the NIEL, a threshold energy for atomic displacement of $21\,\text{eV}$ is used [36, 38, 58].

In Fig. 6.11 it is interesting to note that the proton and electron data points fall onto a single curve without the need to include an equivalency factor that scales the electron D_d to the proton D_d. Such a factor, also described as R_{ep} factor in chapter 5.2.3, is typically used in the analysis of the radiation degradation of cell parameters like open circuit voltage. Considering the fact that the short-circuit current is mainly influenced by the diffusion length, this observation, however, is in-line with the work of Baur et al. [58]. They demonstrated that in the analysis of short-circuit current radiation data, no proton to electron equivalency factor is required if the $21\,\text{eV}$ threshold energy is used in the NIEL calculation.

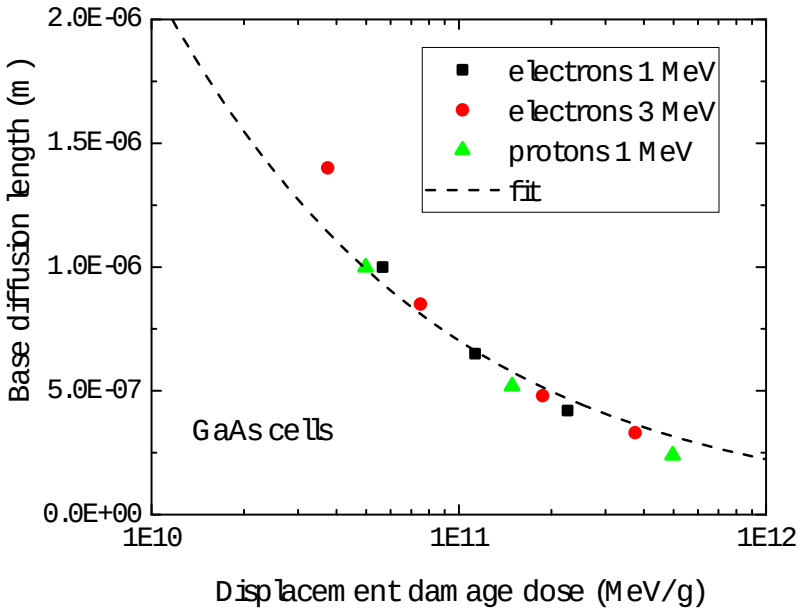

Figure 6.11 Minority carrier base diffusion length versus displacement damage for GaAs cells irradiated by 1 and $3\,\text{MeV}$ electrons and $1\,\text{MeV}$ protons.

$$\frac{1}{L_n^2} = \frac{1}{L_{n0}^2} + K_L \cdot D_d \tag{6.12}$$

The behavior of the diffusion length is approximated well by the the classical equation according to Eq. 6.12 [85], where L_{n0} denotes the diffusion length prior to irradiation and K_L the damage coefficient. The decrease in diffusion length is independent of particle type and energy, which implies that the defect types created by the different particles have an effect on the diffusion length which is only dependent on the displacement damage. The damage coefficient, which describes the degradation behavior of the base diffusion length, is $K_L = 15\,\frac{\text{g}}{\text{MeV m}^2}$. It is important to note that the damage coefficient K_L in this section cannot be directly compared to the damage coefficients in [85] because

the damage coefficient in [85] describes the degradation of base diffusion length versus fluence whereas in this section, the damage coefficient describes the degradation of base diffusion length versus displacement damage dose. A comparison of damage coefficients is possible when the unitless damage coefficients $3.2e-6$ for 150 keV protons, $1.3e-6$ for 3 MeV protons and $1.2e-6$ for 10 MeV protons published in [85] are normalized with their corresponding NIELs. By doing so, damage coefficients of $0.5-2\,\frac{\mathrm{g}}{\mathrm{MeV\ m^2}}$ result. These values are one order of magnitude smaller than the value found in this section. There are many possible origins of the difference of the damage coefficient, which are differences in doping density, doping type, impurity concentration, and cell thickness. The damage coefficient found in this section clearly describes the degradation behavior of the base diffusion length of the cell type under investigation. However, for another cell type, even if the base material is the same (GaAs), the degradation behavior can be different.

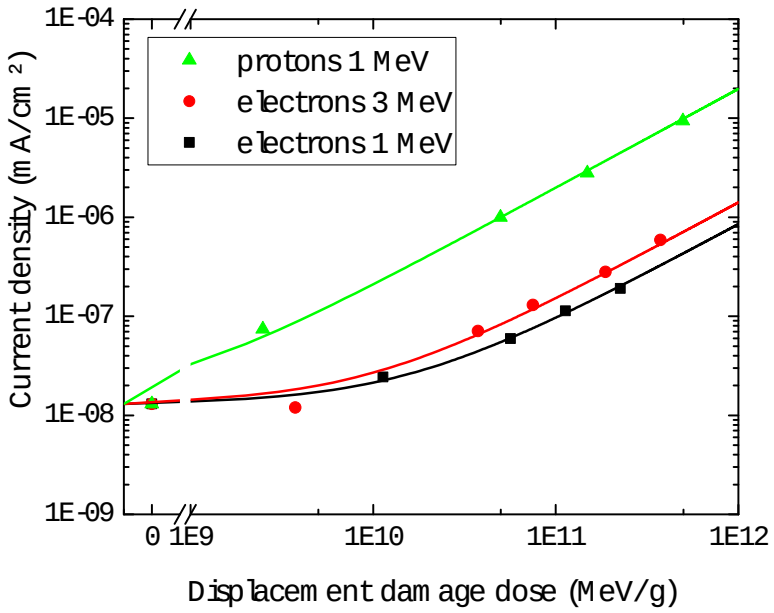

Figure 6.12 Recombination current density I_{02} versus displacement damage for GaAs cells irradiated by 1 and 3 MeV electrons and 1 MeV protons.

In Fig. 6.12, the recombination current density I_{02} is plotted against displacement damage. While the data points for 1 and 3 MeV electrons are grouped together fairly closely as expected, the proton data clearly does not collapse with the electron data. An equivalency factor of $R = 18$ would be required to match proton data and electron data. Since I_{02} is closely linked to V_{oc}, this result is in line with the finding of Baur et al. that for the open-circuit voltage V_{oc} an equivalency factor is necessary to match the proton and electron data despite an adapted NIEL value [58]. The data points in Fig. 6.12 are well described by a fit curve according to Eq. 6.13 [86]. This implies that the

recombination current density I_{02} follows a linear dependence on displacement damage. This is according to expectations, taking the theoretical dependence of I_{02} on carrier lifetime into account [86].

$$I_{02} = I_{02,BOL}\left(1 + \frac{D_d}{D_{d,0}}\right) \tag{6.13}$$

The built-in voltages and the doping densities are shown in Figs. 6.13 and 6.14. Both parameters decrease with increasing displacement damage dose due to the carrier removal effect, which is explained later in this section.

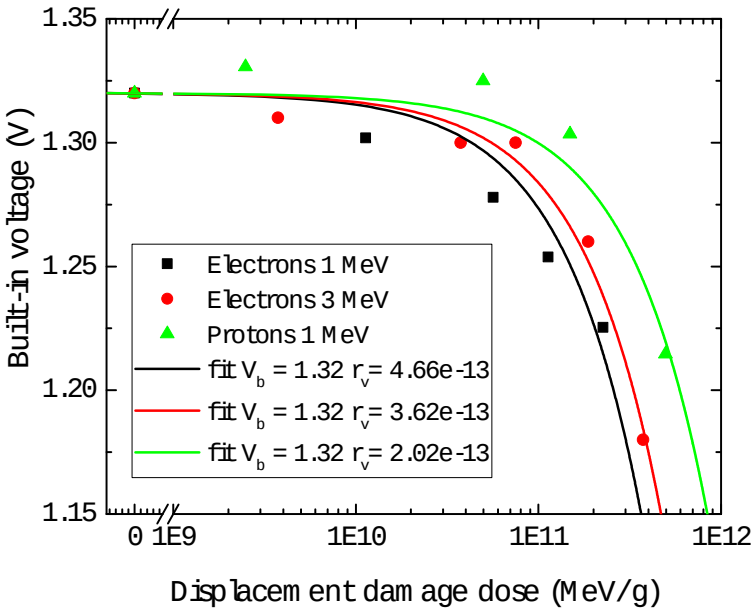

Figure 6.13 Built-in voltage V_b versus displacement damage for GaAs cells irradiated by 1 and 3 MeV electrons and 1 MeV protons.

The lines are fits to the data points using Eqs. 6.14 and 6.15 [85], where N_{A0} is the BOL doping density in units $\frac{1}{\text{cm}^3}$, R_c the carrier removal rate in units $\frac{\text{g}}{\text{MeV cm}^3}$, V_{b0} the BOL built-in voltage and K_v the built-in voltage damage coefficient in units $\frac{\text{g V}}{\text{MeV}}$. The data points in Fig. 6.13 look like they are spread over a larger area, but it has to be considered that the y axis range only covers 0.2 V. The comparison with the carrier removal rates in [85] shows that the rates of $2-3\,\frac{\text{g}}{\text{MeV cm}^3}$ found for GaAs are in the same order of magnitude as for the proton irradiated GaAs cells in [85].

Both parameters decrease with increasing displacement damage dose due to the carrier removal effect. The typical degradation mechanism in a semiconductor are defects which act as recombination centers for minority carriers. Carrier removal is a degradation mechanism which describes the reduction of majority carrier concentration in a semiconductor.

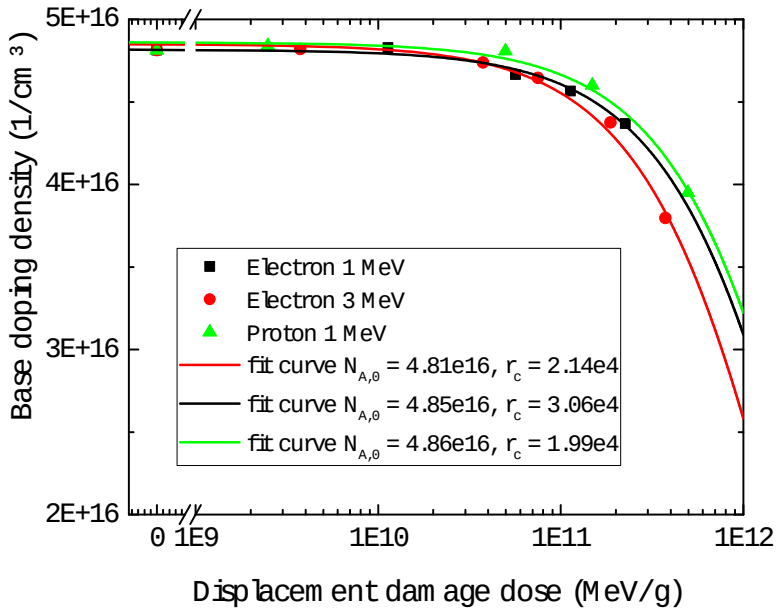

Figure 6.14 Doping density I_{02} versus displacement damage for GaAs cells irradiated by 1 and 3 MeV electrons and 1 MeV protons.

$$V_b = V_{b0} - K_v D_d \tag{6.14}$$

$$N_A = N_{A0} e^{-\frac{R_c D_d}{N_{A0}}} \tag{6.15}$$

The decrease in carrier density or effective decrease in doping density leads to a broadening of the SCR width which partly compensates the shorter minority carrier diffusion length. For instance, the I_{sc} of the cell irradiated with $1e16\ \frac{1}{cm^2}$ 3 MeV electrons is $7.60\ \frac{mA}{cm^2}$ lower than of the BOL cell. Without the decrease in doping density and built-in voltage, the decrease in short-circuit current would be $7.94\ \frac{mA}{cm^2}$. So the effect of irradiation on doping density and built-in voltage leads to a compensation of the current decrease of $0.34\ \frac{mA}{cm^2}$, which is $4.5\,\%$ of the original difference in current. The decrease of both doping density and built-in voltage is stronger for electrons than for protons in both materials, which might be caused by defects created by electrons that are more likely to remove majority carriers. At first glance, this contradicts the result of the diffusion length decrease, which is only dependent on the displacement damage and not on the particle type. However, it is a priori not clear that the same defects are responsible for recombination of electron-hole pairs and for the compensation of one kind of charge carriers (holes in the base region). Apparently, the base diffusion length is not dependent on the defect energy in the bandgap. The carrier removal is, however, dependent on the defect energy in the bandgap. The difference in electron

and proton data can be reconciled by introducing an effective displacement $D_{d,eff} = \frac{D_d}{R}$ damage dose like it is done in the NRL displacement damage dose analysis of solar cell parameters. For the proton data of the doping density and the built-in voltage, an R of approximately 2 would collapse the data points.

6.5 Conclusion

Single junction GaAs cells, representative of the middle junction in current III-V triple junction cells, were irradiated with proton and electron fluences above those encountered in typical GEO missions. Under these conditions, the short circuit current significantly degrades due to a reduction in the emitter and base minority carrier diffusion length. The field assisted carrier collection in the space charge region thus accounts for a larger fraction of the total photocurrent of the cell. Since the width of the space charge region decreases with applied external voltage, the current collected in the space charge region decreases and thus the overall photocurrent. It is important to include this effect in modeling the IV curve and not to attribute it to a shunt resistance effect, which can always be ruled out by a dark IV measurement. Tunneling currents are found to be active at low temperatures, but are excluded at room temperature. The degradation of the diffusion length is found to depend only on the displacement damage dose deposited, taking into account a T_d of 21 eV, but neither on particle type nor on particle energy. The behavior of I_{02}, in contrast, is found to depend on the particle type. These observations are in-line with the behavior of short circuit current and open circuit voltage of III-V solar cells under irradiation. It is found that the decrease of effective doping density by carrier removal partly compensates the decrease of short-circuit current by irradiation. Furthermore, the behavior of the built-in voltage and the doping density is found to be dependent on particle type.

7 Analysis of particle irradiated 4-junction cells

7.1 Introduction

Over the last decades, the efficiency of solar cells has increased continuously [87]. Beginning with silicon monojunction cells, the evolution of space cells led to GaAs monojunction cells to GaAs/Ge dualjunction and GaInP/GaAs/Ge triplejunction cells. The most recent generation of solar cells for space use are quadruple or four-junction (4J) solar cells. They will be integrated in future satellite solar panels [88]. Even 5J and 6J solar cells have been developed in the laboratory [89, 90], but 4J is the most recent state of technology regarding solar cells in series production for actual use in space. For 4J cells, already a few irradiation results have been published, but only for few fluences with 1 MeV electrons [91, 92]. The behavior of 4J cells under particle irradiation covering protons and electrons of different energies and fluences is yet to be determined.

In this chapter, the results of a 4J irradiation campaign will be presented and discussed, which was conducted to determine the behavior of 4J cells under particle irradiation. Firstly, particles, energies, and fluences, which are representative of the particle environment around Earth, are chosen for the irradiation. Details of the particle parameters used for irradiation will be presented and explained.

Secondly, the resulting degradation data of the irradiation campaign will be presented. With this data, it is possible to analyze the degradation behavior of the 4J cells. Especially the degradation of the solar cell parameters I_{sc}, V_{oc} and P_{mpp} will be shown along with a comparison between the different isotype cells and the behavior of the 4J cell.

As method for data analysis, the NRL method with variable threshold energy for atomic displacement has proven useful for 1J and 3J cells. The method needs a lot less data than the JPL method and it uses the physical parameter T_d instead of the empirical exponent n. The method, which up to now has never been applied to 4J cell degradation data, will be used and its applicability will be verified for 4J cells. Moreover, the degradation data of the four different subcells of a 4J cell will be analyzed by characterizing 1J isotype cells representative of the subcells of a 4J cell. The isotype

degradation results are compared to the 4J degradation results and discussed.

In the last section of this chapter, the mission profile of a satellite which uses electrical propulsion for its transfer to a geostationary orbit will serve as an example. Electrical propulsion is an energy-efficient way of bringing payload in its final orbit. Due to the low thrust generated by electrical propulsion, the duration of the transfer phase of a satellite is in the range of months compared to days using chemical propulsion. For the solar generator, this means two things: Firstly, energy has to be generated during the whole transfer phase. Secondly, the solar generator will be exposed to higher displacement damage doses because during the transfer phase the satellite crosses the particle-richest areas of the Van Allen belts multiple times. Therefore, it is most important to know the behavior of 4J cells under high electron and proton irradiation. In this chapter, the BOL and EOL values of the power of a solar generator will be computed for an example electric orbit raised (EOR) mission to the GEO orbit and a following 15 years on-station. The expected degradation of solar cells on an EOR + GEO mission with shielding cover glass is computed and all steps are explained in detail.

7.2 Particle environment

To determine the degradation of the 4J cells under particle irradiation, four 4J cells per fluence are irradiated with electrons and protons. To determine the impact of the four different subcells, two isotype cells per fluence representative of each subcell are irradiated and characterized. The fluences are shown in Tab. 7.1. So overall, 112 4J cells and 56 of each J1, J2, J3, and J4 isotype cells are irradiated.

All cells irradiated have a size of $2 \cdot 2\,\mathrm{cm}^2$. The reason for choosing these particles,

electrons 1 MeV ϕ (cm^{-2})	electrons 3 MeV ϕ (cm^{-2})	protons 1 MeV ϕ (cm^{-2})	protons 2 MeV ϕ (cm^{-2})	protons 5 MeV ϕ (cm^{-2})
1e14	3e13	3e10	3e10	1e11
3e14	1e14	1e11	1e11	3e11
5e14	3e14	3e11	3e11	1e12
1e15	1e15	1e12	1e12	3e12
3e15	3e15	3e12	3e12	1e13
5.5e15	6.1e15			
1e16				

Table 7.1 Particles, energies, and fluences used in irradiating the 4J multijunction and isotype cells.

energies, and fluences will be given in the following. To determine the behavior of the

cells in space, the particle environment shall be represented accurately. The biggest part of the cell degradation is caused by protons and electrons trapped in the Van Allen belts around Earth as well as by solar protons. Therefore, electrons and protons are used to irradiate the cells. Regarding the tested energies for protons, it is important to consider the range of protons in matter. If a proton's track ends inside matter, it transfers a high amount of energy to the material. This energy peak is called Bragg peak. The D_d method for analyzing degradation data is, however, only applicable if the particle penetrates all subcells and the particle's energy remains approximately constant. The range of protons in the cell stack was simulated already for 3J cells in chapter 5. There, the accepted minimum was 0.3 MeV. The overall thickness of the active subcells is not known because it is intellectual property of the cell manufacturer. The minimum energy for proton testing on 4J cells was chosen to be 1 MeV, which represents a penetration depth of approximately $10\,\mu$m in Ge, which was computed with SRIM [27]. Energies above 10 MeV play a minor role. Therefore, protons with the energies 1, 2, and 5 MeV are chosen to represent the proton-dominated inner Van Allen belt, which will be crossed several times by the satellite during the EOR phase. For electrons, the lower energy limit is set by the fact that below approximately 0.3 MeV, the NIEL is negligible and electrons cannot cause displacement damage. Therefore, the energies 1 MeV and 3 MeV are chosen as test energies. It is important to test at least two electron energies to find out the proper threshold energy for atomic displacement by fitting the electron data [38]. The NIEL is most sensitive on T_d for low electron energies, which is why these energies were chosen. The fluences of the all particles and energies are chosen so that the resulting displacement damage dose lies between $1e9$ and $1e11\,\frac{\text{MeV}}{\text{g}}$, which is the representative displacement damage dose range for current space missions of 200 days EOR phase and a subsequent phase of 15 years in orbit.

7.3 Degradation behavior of single and quadruple-junction cells

The analysis of the data is conducted using the NRL method as introduced in chapter 5. The threshold energy for atomic displacement is determined for the 4J cell materials. The remaining factors of electrical parameters are plotted against the displacement damage dose.

7.3.1 open-circuit voltage

The open-circuit voltage is an electrical parameter of a multi-junction solar cell, which adds up for all subcells in a cell stack. Therefore, the sum of the open-circuit voltages of the single-junction cells can be directly compared with the open-circuit voltage of

the 4J stack. In Fig. 7.1, the RFs of the V_{oc} of the four isotype cells J1 (AlInGaP), J2 (AlInGaAs), J3 (InGaAs), and J4 (Ge) are shown. The degradation data points are shown along with the fit curves resulting from the analysis in Fig. 7.1. The fit parameters are shown in the corresponding inset. As can be clearly observed, the data

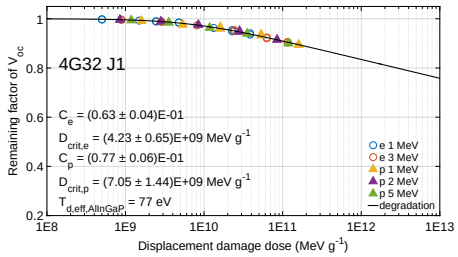

(a) Degradation of open-circuit voltage of 4G32 isotype J1 cells.

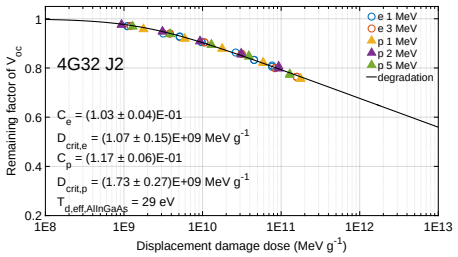

(b) Degradation of open-circuit voltage of 4G32 isotype J2 cells.

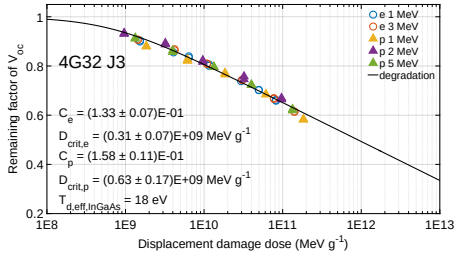

(c) Degradation of open-circuit voltage of 4G32 isotype J3 cells.

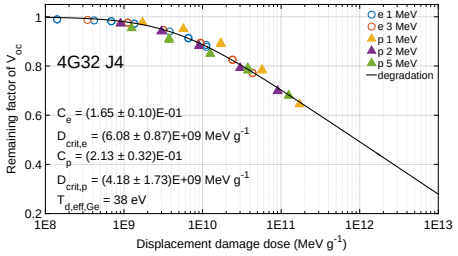

(d) Degradation of open-circuit voltage of 4G32 isotype J4 cells.

Figure 7.1 Degradation characteristics of open-circuit voltage of 4G32 isotype cells.

points of all electron and all proton energy data points collapse onto a single curve for each of the four isotype cells. This serves as a first verification that the displacement damage dose method using the threshold energy for atomic displacement can be applied to the single junction cells of a 4J cell. In Fig. 7.1a, J1 is shown, which degrades to app. $90\,\%$ for the highest D_d. J2 degrades to app. $75\,\%$, J3 to below $60\,\%$ and J4 to app. $65\,\%$. In terms of V_{oc}, J3 relatively degrades the most of all four isotypes.

Comparing the slopes C_p of the different isotype degradation curves, a clear tendency for a steeper slope can be observed. Starting from 0.077 for J1, 0.117 for J2 and 0.158 for J3, the steepest slope is determined for J4 with 0.213. Compared with the isotypes of a 3J cell, the same behavior is observed from top to bottom isotype cells. The radiation hardness of a cell is dependent on the atomic composition of a subcell. Since both J1 and J2 include the element Al, which is not part of J3 and J4, it is possible that Al in a solar cell is responsible for increased radiation hardness. Al has a T_d of $50\,\text{eV}$, which is indeed a lot higher than the threshold energies of the other elements of the subcells. This means that more energy is required to displace an Al atom [66].

In the fitting process, effective threshold energies for atomic displacement are determined, which are 77 eV for J1, 29 eV for J2, 18 eV for J3 and 38 eV for J4. With 18 eV, the threshold energy of J3, shown in Fig. 7.1c, is close to the value 21 eV of the GaAs middle cell of a 3J cell. Since J3 mostly consists of Ga and As as well, the same As_{Ga} or Ga_{As} antisite defect may be mainly responsible for the recombination of electron-hole pairs. The In content of J3 may be responsible for the difference that was found in the threshold energy. The determined values 18 eV of J3 and 38 eV of J4 match well with the determined values for the GaAs subcell of a 3J cell with 21 eV and the Ge subcell of a 3J with 40 eV. This indicates that using the NRL method together with $T_{d,eff}$ for analyzing MJ cells results in reliable results.

The threshold energy for atomic displacement of J1 is found to be 77 eV, which is large compared to values of the single elements Al, Ga, In or P, which are 50, 9-10, 3-6.7, and $8 - 8.7$ eV [64, 66–68]. The energies of the single elements represent Frenkel-pairs. A Frenkel-pair is the simplest case of a defect and is created by displacing one atom, which then leaves a vacancy behind on its original lattice location. The dislocated atom eventually rests on an interstitial position. A T_d value of 77 eV indicates that much energy is needed to create effective defects in this isotype cell. The threshold energy is most likely not linked to a Frenkel-pair but to a defect consisting of more than one atom, maybe even different atom species. This kind of defect, where more than one atom is involved, was already found in the case of the 21 eV defect of the GaAs middle subcell of a 3J cell. There, an antisite defect consisting of a Ga and an As displacement was found to be the most likely candidate to explain the threshold energy. Furthermore, the situation of the J1 $T_{d,eff}$ determined is similar to that found for the 3J top cell. Already for the GaInP top cell, a threshold energy was found (35 eV) which is higher than that of each of its elements Ga, In, and P. The elemental composition of J1 is similar to a 3J GaInP top cell but with additional Al, which leads to the conclusion that Al is responsible for additional radiation hardness. Molecular dynamics simulation or DLTS could provide more insight into this topic, but this is not part of this thesis.

The NIELs resulting from the four determined subcell-specific $T_{d,eff}$s for full energy spectrum of protons and electrons are depicted in Fig. 7.2. For protons of more than 30 keV, the NIELs are approximately identical. For electrons, the NIELs differ quite significantly. The topmost curve of the electron NIELs shows the NIEL of J3. In this graph, we can see clearly that the non-ionizing energy loss of electrons up to 10 MeV is largest in J3.

Following the analysis of 3J cells, the NIEL of the least radiation hard subcell, which is J3, is used to fit the multi-junction 4J cell. The result is depicted in Fig. 7.3. Although four different subcells with four different degradation behaviors contribute to the the open-circuit voltage of the 4J cell, the data points collapse onto a single curve. This is

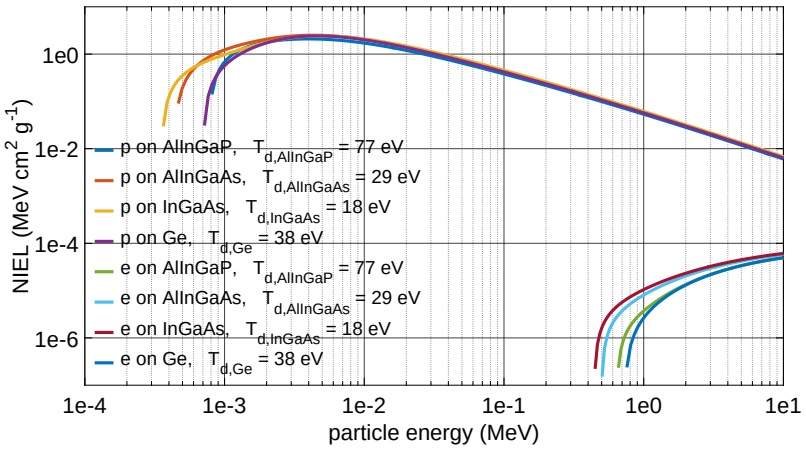

Figure 7.2 NIEL of the effective threshold energies for atomic displacement determined from the degradation of the V_{oc} of 4G32 isotype cells.

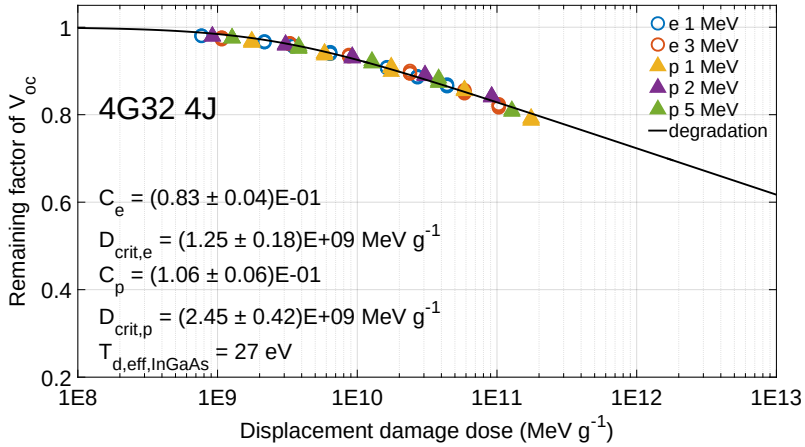

Figure 7.3 Degradation characteristics of open-circuit voltage of 4G32 4J cells.

a verification that the displacement damage dose method using $T_{d,eff}$ can be applied to 4J cells.

The threshold energy of 27 eV, however, does not match the threshold energy 18 eV of the J3 isotypes. This behavior is different than with GaAs cells and 3J cells, which can both be fitted with an effective threshold energy of 21 eV. The reason for this different behavior is that all subcells contribute to the open-circuit voltage of an MJ cell, which is the sum of its contributions. So a priori, the behavior of the V_{oc} of one subcell does not match with the behavior of the V_{oc} of the whole multi-junction cell. This is the case for the 4J cell and its subcells. In 3J cells, the situation is different because the mid cell is one of three subcells and influences the behavior of the 3J cell more profoundly (the voltage contribution of mid to 3J cell is approximately double the voltage contribution of J3 to 4J) than J3 influences the 4J cell.

To determine the individual contributions of the different subcells, firstly it is checked how well the isotypes match the behavior of the 4J cell. Towards this end, the absolute

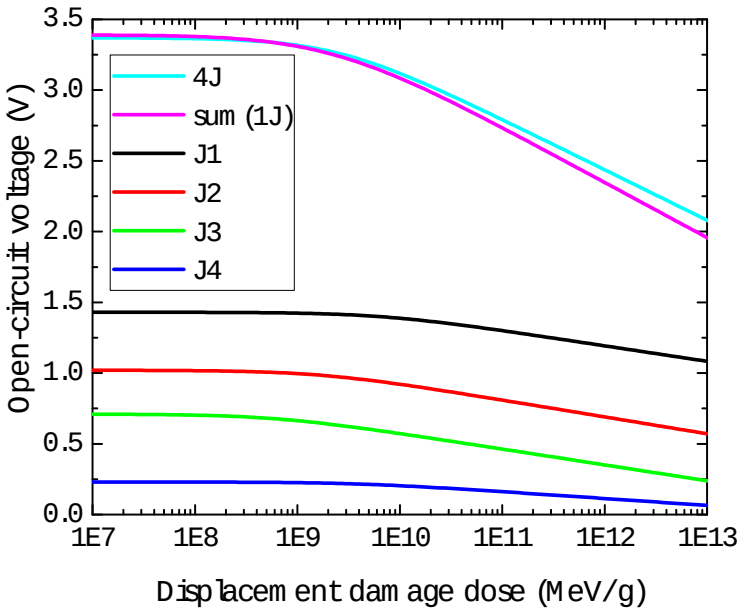

Figure 7.4 Comparison of the absolute degradation of the open-circuit voltage of 4G32 isotypes, the sum of the four isotypes and the 4J cell.

degradation curves are compared. In Fig. 7.4, the absolute degradation curves are plotted, which consist of the relative degradation curves determined in this section multiplied with their respective absolute BOL value. The sum of the V_{oc}s of the 1J cells matches the 4J cell with a difference smaller than $67\,\mathrm{mV}$ or $2.5\,\%$ up to a dose of $2e11\frac{MeV}{g}$. This is the highest dose applied to the cells in this study. The curve beyond this dose is extrapolated, which is most likely responsible for the increasing difference of the curves. A typical mission dose of $1e10\,\frac{\mathrm{MeV}}{\mathrm{g}}$ results in a degradation of V_{oc} of the 4J cell to $92.5\,\%$ or $3.119\,\mathrm{V}$. The remaining factors of the isotype cells are $97.1\,\%$ for J1, $90.3\,\%$ for J2, $80.7\,\%$ for J3 and $88.8\,\%$ for J4, which sums up to an absolute voltage of $3.086\,\mathrm{V}$, which is a difference of $1.5\,\%$ to the 4J value and within measurement tolerance. In conclusion, the irradiated 4J cells are characterized well and behave equal to irradiated isotype cells. The magnitude of degradation of each individual subcell can clearly be determined.

7.3.2 short-circuit current

Since the current of a multi-junction cell is determined by the subcell with the least current, it is desired that all subcells of a multijunction cell generate a similar current not only BOL but also under irradiation. The short-circuit current of the four different isotypes after particle irradiation is determined in this section and shown in Fig. 7.5. In Fig. 7.5a, the data points and corresponding fit curve for the I_{sc} of J1 is shown. The current of J1 degrades only to app. $90\,\%$ of its BOL value at the highest tested D_d,

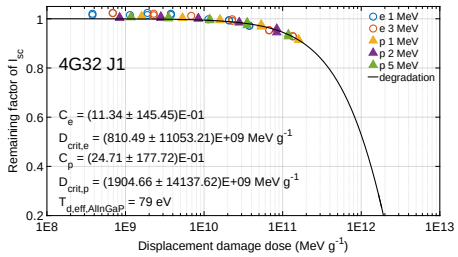

(a) Degradation of short-circuit current of 4G32 isotype J1 cells.

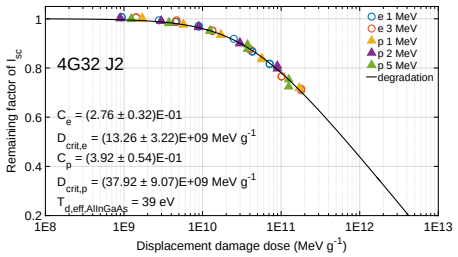

(b) Degradation of short-circuit current of 4G32 isotype J2 cells.

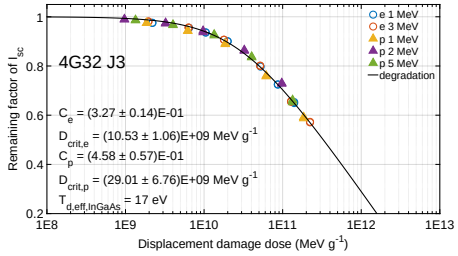

(c) Degradation of short-circuit current of 4G32 isotype J3 cells.

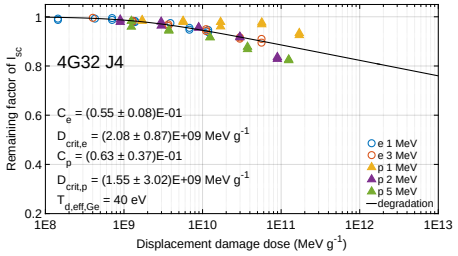

(d) Degradation of short-circuit current of 4G32 isotype J4 cells.

Figure 7.5 Degradation characteristics of short-circuit current of 4G32 isotype cells.

which is more radiation hard than J2 with app. $70\,\%$, J3 with app. $60\,\%$, and J4 with $80 - 90\,\%$. The electron data points as well as the proton data points collapse well to a single curve which describes the degradation behavior of the I_{sc} of an AlGaInP cell well. The fit parameters are given in the inset. Through the analysis of I_{sc}, 79, 39, 17, and $40\,$eV were determined as threshold energies for J1, J2, J3, and J4. Each of these energies does not differ more than $2\,$eV from the value found in the analysis of V_{oc}.

Regarding J4, the proton data points at higher fluences, especially the $1\,$MeV proton data, do not collapse well with the other energies. Since $1\,$MeV is the lowest of the tested proton energies and J4 is the isotype cell which lies deepest from the surface of the cell, the non-linear rise of energy transfer from the proton to the lattice atoms at the end of the proton tracks might partly have happened in the active region of the cell. The D_d method is, however, only applicable if the energy of the particles remains approximately constant. Whether the $1\,$MeV Bragg peak lies in the active volume of J4 or not cannot be determined clearly because the exact thicknesses of the subcells are not known. If the Bragg peak lies in J4, a stronger degradation is expected than of the other energies, which is obviously not the case. Moreover, Fig. 7.1d shows a collapse of the proton $1\,$MeV data in the V_{oc} case. Consequently, it is unlikely that the Bragg peak lies in J4. It is unclear why the current of J4 isotypes irradiated with $1\,$MeV protons degrades less than when irradiated with 2 and $5\,$MeV protons.

The threshold energy of J4 is found to be $40\,$eV. This value is not only similar to the value found for the V_{oc} degradation of J4, but also to the value found for the Ge subcell

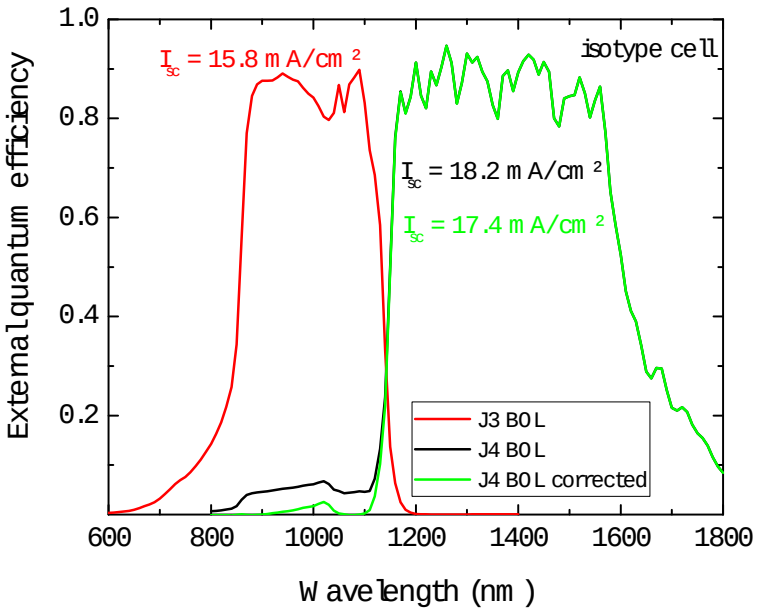

Figure 7.6 External quantum efficiency of a J3 isotype cell, a J4 isotype cell as measured and the corrected EQE of J4 without the current induced by luminescent coupling of J3.

of a 3J cell. This is a first verification that a $T_{d,eff}$ of around $40\,\text{eV}$ can be allocated to one or more radiation-induced defect types in germanium, independent of the cell stack surrounding the Ge subcell. It is important to note that in order to get the BOL value of I_{sc} of J4 which originates solely from J4, a correction is necessary. A certain ratio of the photons absorbed in the J3 region of the J4 isotype cell recombine generating new photons with an energy of the direct bandgap of GaInAs. From these photons, which are emitted in all directions in the cell material, again a certain amount is absorbed in the germanium of J4 which leads to an increased current value. This effect is called luminescent coupling and was already investigated in 3J cells in chapter 5 and in [63]. The effect on the short-circuit current of J4 is quantified by EQE measurements shown in Fig. 7.6. In this figure, the EQE of a BOL J3 is shown along with the EQE of a BOL J4.

Using the correction equation of [63] effectively results in a subtraction of the additionally generated current in J4, which is caused by luminescent coupling of J3 to J4. The EQE curves are integrated with the AM0 spectrum to get the resulting I_{sc}. The luminescent coupling is responsible for an additional short-circuit current in J4 of $\Delta I_{sc} = 0.78\frac{mA}{cm^2}$ in this example cell, which is less than for 3J cells, where $\Delta I_{sc} = 4.1\frac{mA}{cm^2}$. The reason for this could be a higher intrinsic defect density and consequently a lower radiative recombination in J3 due to the growth of this subcell on a metamorphic layer. The respective current value was subtracted from the BOL value of the I_{sc} of J4 cells for all proton energies. In all irradiated cells used in this thesis, also called EOL cells,

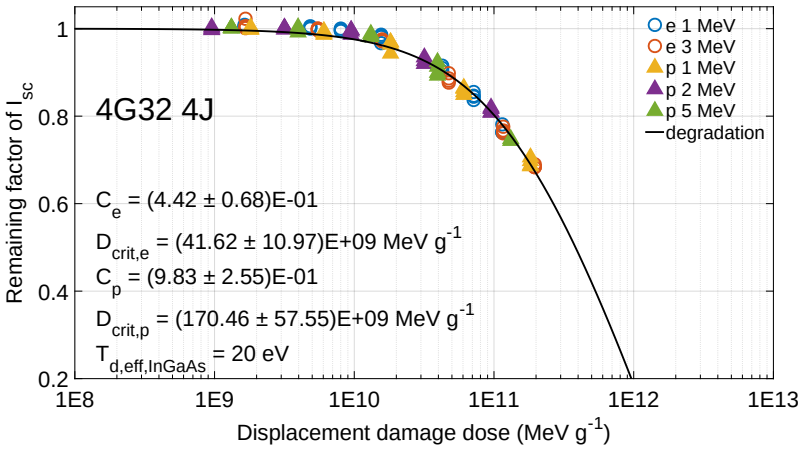

Figure 7.7 Degradation characteristics of short-circuit current of 4G32 4J cells.

this correction is not necessary because radiative recombination is reduced drastically due to the enhanced amount of SRH-defects. It is important to note that the RF data points in Fig. 7.5d include this correction process. To compare the degradation of the isotype cells to the 4J cell, the 4J cell is analyzed using the $T_{d,eff}$ of J3, since this is the cell mostly responsible for the I_{sc} degradation. The result is shown in Fig. 7.7. The data points again collapse well on a single curve. The $T_{d,eff}$ results in $20\,\text{eV}$, which agrees well with the $T_{d,eff}$ of $18\,\text{eV}$ of J3. The absolute values of the I_{sc} degradation curves of the 1J cells and the 4J cells is depicted in Fig. 7.8. The curves are shown up to a dose of $2e11\frac{\text{MeV}}{\text{g}}$ because up to this dose, data points exist and the curves are no extrapolation. The current of J1 is the smallest current of all isotype cells from a dose of $1e7$ to $1e10\,\frac{MeV}{g}$. Therefore, up to a dose of $1e10\,\frac{MeV}{g}$ which approximately corresponds to an equivalent $1\,\text{MeV}$ electron fluence of $1e15\,\frac{e}{cm^2}$, J1 is current limiting for the 4J cell. In the same dose range from $1e7$ to $1e10\,\frac{MeV}{g}$, the current of J2 and J3 is approximately equal. However, above $1e10\,\frac{MeV}{g}$, J3 degrades stronger than J2 and the 4J cell is limited in its current generation by J3. The current of J4 is bigger than that of all other cells and therefore never current limiting.
This degradation comparison shows possibilities for future cell improvements: For BOL use, the 4J cell current can be increased by increasing the J1 current. For use in particle environment, the current of J3 should be increased or in other words, J3 should be made more radiation hard. Following that, the current of J2, which is close to the J3 current, should be increased as well towards higher radiation hardness.

At a D_d of app. $1e10\,\frac{MeV}{g}$, the current-limitation of the 4J cell changes. So the 4J degradation curve should basically be a compound curve of the J1 and the J3 degradation. As we see in Fig. 7.8, that is not exactly the case from $1e10\,\frac{MeV}{g}$ onwards. Although the current of the 4J cell and J1 resp. J3 match within a band of approximately $10\,\%$, the degradation behavior of the 4J cell and especially J3 above $1e10\,\frac{MeV}{g}$

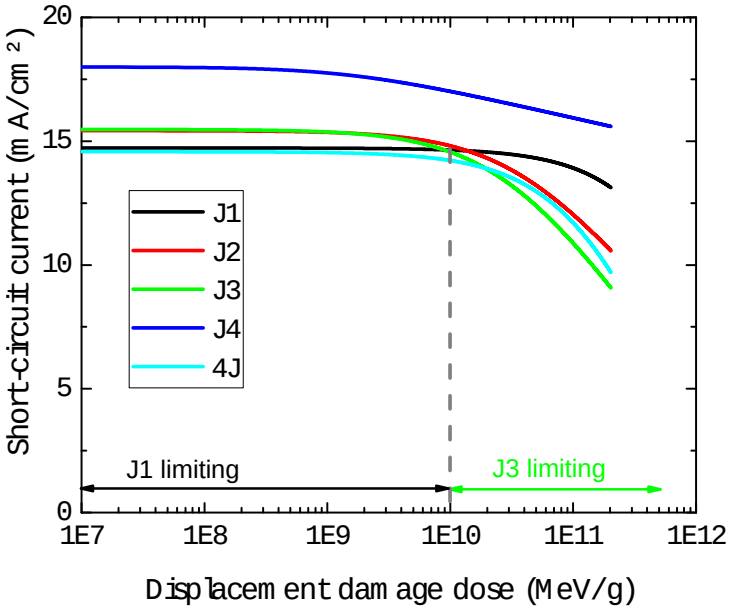

Figure 7.8 Comparison of the absolute degradation of the short-circuit current of 4G32 isotypes and the 4J cell.

is not quite the same. The 4J cell shows a steeper slope and therefore degrades faster. The origin of this effect is not clear. Since the curve is based on data points with a maximum of $2e11\,\frac{MeV}{g}$, it is possible that the uncertainty of the fit based on the limited data is the origin of the different slopes. Comparing the slopes of the J3 fit with $C_{J3} = 0.458 \pm 0.057$ and of the 4J fit with $C_{4J} = 0.983 \pm 0.255$, it is shown that the fit uncertainty cannot fully explain the slope difference. Another difference which could be responsible for the current difference of the current-limiting 1J cell and a 4J cell is the operating point. At short-circuit current, the overall cell voltage is $V = 0$. For a SJ cell, the situation is clear and the I_{sc} is measured at $V_{1J} = 0$. For an MJ cell, the situation is different. Since at BOL, a 4J cell is current limited by the J1 subcell, it also means that at short-circuit, the J1 subcell of the 4J cell is operated at a negative voltage. This situation is depicted in Fig. 7.9a. In Fig. 7.9a, the current-voltage characteristics of four different isotype cells are shown under AM0 illumination. Under the assumption that the isotypes represent the subcells of a 4J cell well, the short-circuit current of a 4J cell, which is the least current of the isotypes, is marked. For these four specific subcells, the value is $14.8\,\frac{\text{mA}}{\text{cm}^2}$. This current is marked by a dashed line. At short-circuit, the sum of the voltages of the subcells is zero. Due to the fact that the subcells, which are not current-limiting, are operated at positive voltages of $V_{J2} = 0.96\,\text{V}$, $V_{J3} = 0.56\,\text{V}$, and $V_{J4} = 0.21\,\text{V}$, J1 is operated at a voltage which can be calculated by $V_{J1} = -(V_{J2} + V_{J3} + V_{J4}) = -1.63\,\text{V}$.

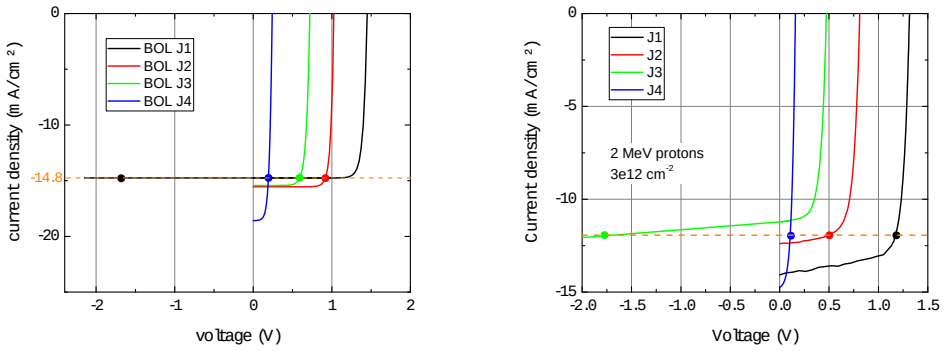

(a) 4G32 isotypes at BOL.

(b) 4G32 isotypes at EOL.

Figure 7.9 Current-voltage characteristics of 4G32 isotypes at BOL and EOL ($= 3e12\frac{1}{\text{cm}^2}$ 2 MeV protons, which is app. a dose of $1e11\frac{\text{MeV}}{\text{g}}$). The negative branch is extrapolated because an LIV curve is not measurable in the negative voltage range. The big dots show the operating point of the four isotypes under the assumption that the isotypes are subcells in a 4J cell stack.

For the EOL case, an irradiation of $3e12\frac{1}{\text{cm}^2}$ 2 MeV protons is chosen, which equals a dose of approximately $1e11\frac{\text{MeV}}{\text{g}}$. The IV-characteristics of the same four isotype cells, but now irradiated, is shown in 7.9b. The LIV curve of J3 is linearly extrapolated on the negative voltage range using the slope at $V = 0$. The extrapolation is necessary because with the experimental setup it is not possible to measure a LIV curve at negative voltage. The linear extrapolation can be justified as follows. As shown in chapter 6, the slope in the photocurrent originates from the voltage dependence of the space charge region in combination with a low minority carrier diffusion length. For negative voltages, the SCR is further broadened and the slope of the LIV curve continues. The short-circuit current in the EOL case is limited by J3 but not equal to the I_{sc} of J3, which would be the current value at V $= 0$. So the degradation of the subcells also leads to a slope in the current branch of the curves, which is horizontal in the BOL case. The I_{sc} of J3 is $11.2\,\frac{\text{mA}}{\text{cm}^2}$, but the I_{sc} of the 4J cell at the same irradiation is $11.8\,\frac{\text{mA}}{\text{cm}^2}$. The $11.8\,\frac{\text{mA}}{\text{cm}^2}$ are indicated by the orange dashed line in Fig. 7.9b. So the difference of the voltage-dependent photocurrent and the position of the operating points of the subcells in a 4J cell is the reason why a 4J cell can have a higher short-circuit current than any of its subcells at the same irradiation level. This could be the reason why the short-circuit current of the J3 limited 4J cell is higher than the short-circuit current of a J3 isotype cell as depicted in Fig. 7.8 from app. $D_d = 2e10\,\frac{\text{MeV}}{\text{g}}$ to $3e11\,\frac{\text{MeV}}{\text{g}}$. There is also quantitative agreement: At $D_d = 1e11\,\frac{\text{MeV}}{\text{g}}$, the I_{sc} for 4J cells is also $0.6\,\frac{\text{mA}}{\text{cm}^2}$ higher than for the J3 cells.

In conclusion, it was found that the short-circuit currents of J1 matches the value of the 4J cell shown from a D_d of $1e7$ to $1e10\,\frac{\text{MeV}}{\text{g}}$ in Fig. 7.8. For higher doses, the current values of the J3 limited 4J cell are higher than of the J3 isotype cell. The reason for this

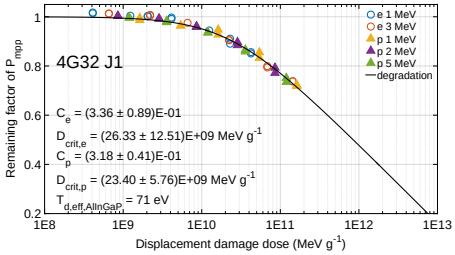

(a) Degradation of power at maximum power point of 4G32 isotype J1 cells.

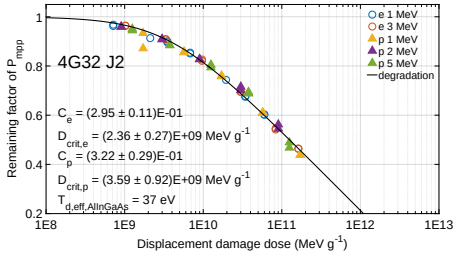

(b) Degradation of power at maximum power point of 4G32 isotype J2 cells.

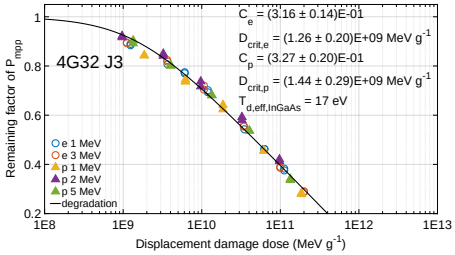

(c) Degradation of power at maximum power point of 4G32 isotype J3 cells.

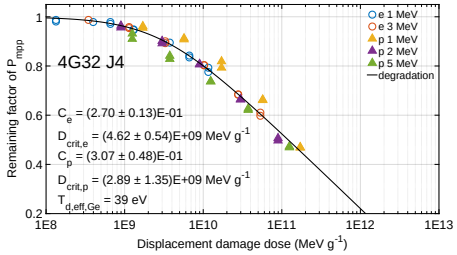

(d) Degradation of power at maximum power point of 4G32 isotype J4 cells.

Figure 7.10 Degradation characteristics of power at maximum power point of 4G32 isotype cells.

is that a J3 cell in a 4J cell stack is operated at a different voltage than a J3 isotype cell at short-circuit condition. In combination with a voltage-dependent photocurrent of irradiated cells, this leads to a shift of the operating point in the cellstack which is responsible for the J3 cell to generate a higher short-circuit current in a 4J cell than in an isotype cell. In other words, in the isotype cell, short-circuit means that $V_{J3} = 0\,\mathrm{V}$. In the 4J cell, short-circuit implies that $V_{4J} = 0\,\mathrm{V}$ and $V_{J3} = -1.76\,\mathrm{V}$. It is important to note that the degradation of the current of a 4J cell can only be approximated by the degradation of the respective current-limiting subcell. As depicted in Fig. 7.7, the data points reveal that the degradation of the 4J cell does not significantly change its slope at any dose. Therefore, the fit of the 4J cell with a single fit curve is possible. In another multi-junction cell technology with i.e. two current-limiting subcells with a very different behavior, it may be necessary to fit the multi-junction degradation data with not a single but two different curves as a stepwise defined function. For the use in space, it is important to note that a cover glass is typically put on top of the cells to reduce particle degradation. Another effect of a cover glass is, however, that the transmission can change dependent of the wavelength. This wavelength dependence can lead to a shift of the specific displacement damage dose where the current limiting cell changes.

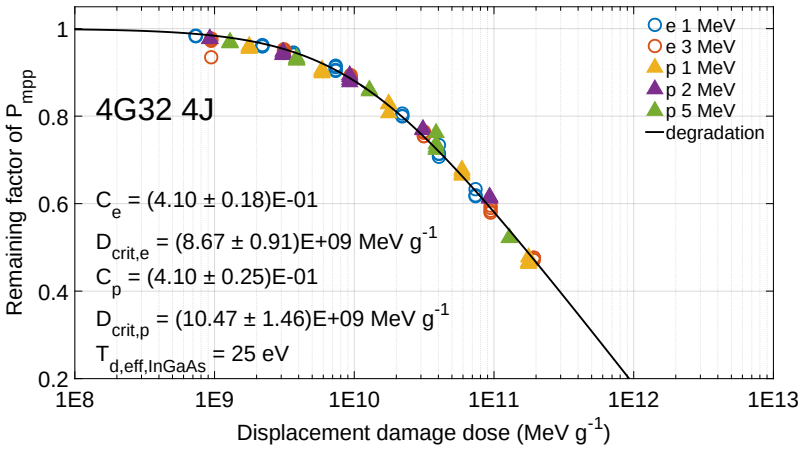

Figure 7.11 Degradation characteristics of power at maximum power point of 4G32 4J cells.

7.3.3 power at maximum power point

The power at maximum point of 1J and 4J cells will be analyzed and compared in this section. The power of the four different isotypes is depicted in Fig. 7.10a-d. The maximum power of J1 cells decreases to about $70\,\%$ of its original value for a dose of app. $2e11\,\frac{MeV}{g}$. The respective RF at this dose of J2 is $45\,\%$, of J3 $30\,\%$ and of J4 also $45\,\%$. The proton data points of the J4 cell in Fig. 7.10d do not completely collapse onto the fit curve. This spread of proton data agrees with similar findings related to the short-circuit current depicted in Fig. 7.5d. Since the power is the product of current and voltage, the spread of the power proton data can be attributed to the contribution of the current. The effective threshold energies for atomic displacement are $71\,$eV for J1, $37\,$eV for J2, $17\,$eV for J3 and $39\,$eV for J4. These values agree well with the values found for V_{oc} and I_{sc} and further confirm the validity of the fitting method. The data and fit curve for the power of 4J cells is shown in Fig. 7.11. The 4J cell decreases to approximately $45\,\%$ of its original value at $2e11\,\frac{MeV}{g}$.

To get a deeper insight into the contributions of the different subcells to the overall power of the 4J cell, the power of each subcell is plotted versus D_d in Fig. 7.12 along with the sum of the subcell powers and the 4J cell power. The power of the 4J cell is smaller than the added power of the isotype cells. This effect is marginal at a dose of $D_d = 1e10\frac{\text{MeV}}{\text{g}}$, but up to $2.5\,\frac{\text{mW}}{\text{cm}^2}$ at BOL and at $D_d = 1e11\frac{\text{MeV}}{\text{g}}$. The reason is not the voltage because from Fig. 7.4, we know that the sum of voltages of isotype cells matches the voltage of a 4J cell well. The origin of this difference is that the maximum power is at a different current for each subcell and also dependent on and changing with irradiation. Within a 4J cell, the subcells are connected in series and therefore forced to work at an equal current level, which means that a priori only one subcell can be operated at its maximum power point. All other subcells are not operated at their respective maximum power points and therefore in a 4J cell the maximum power cannot

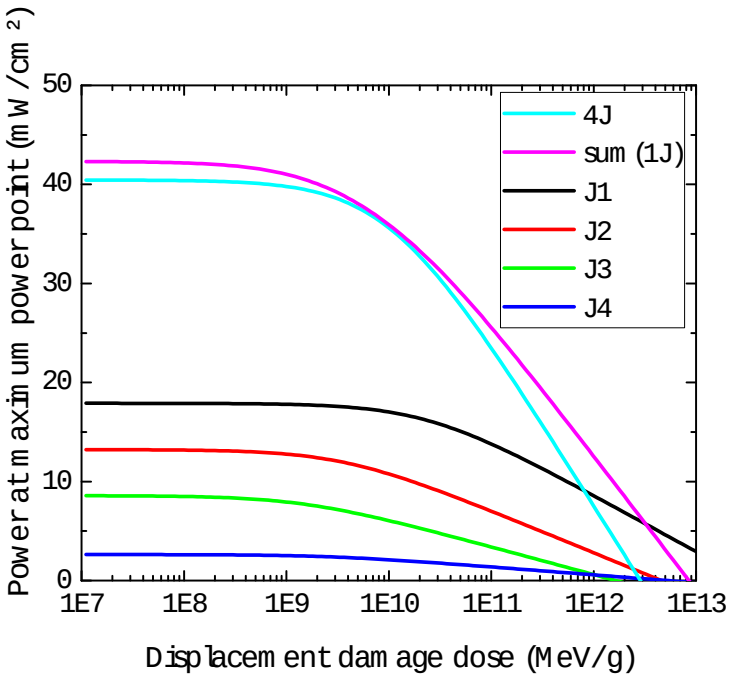

Figure 7.12 Comparison of the absolute degradation of the power at maximum power point of 4G32 isotypes and the 4J cell.

be as high as the summed up power at maximum power point of corresponding isotype cells. For clarification, the case of an equal operating point in a 4J cell is depicted in Fig. 7.9a. In this figure, it can also be seen that each isotype cell has its own maximum power point and most importantly its own current value at maximum power point. Due to the change of the maximum power points of the subcells with irradiation it is possible that at a certain irradiation level, two or more subcells have the same maximum power point current. Such an irradiation level is found at $D_d = 1e10\frac{\text{MeV}}{\text{g}}$, which is why the power at maximum power point of the 4J cell matches the summed up powers at maximum power points of the isotype cells.
In summary, the degradation behavior of the open-circuit voltage, the short-circuit current, and the power at maximum power point of the four isotype cells and the 4J cell of the 4G32 cell type were analyzed, compared, and discussed. In the next section, the degradation analysis of the 4J cell will be utilized.

7.4 Degradation of shielded 4-junction cells on an electric orbit raising mission

In this section, the 4J degradation analysis is used to determine the degradation of a cover glass shielded solar cell. To compute the effect of shielding, a particle environment

of a specific mission is chosen. The steps towards achieving this goal are described in the following.

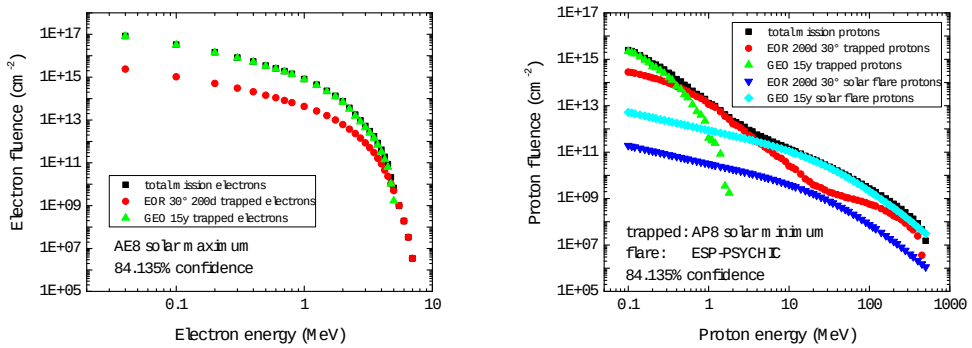

(a) Trapped electron environment

(b) Trapped and solar flare proton environment

Figure 7.13 Particle environment for 200 days of electric orbit raising and 15 years in geostationary orbit.

The chosen mission consists of a satellite, which is raised to its final geostationary orbit (GEO) by electric orbit raising (EOR) [93]. Electric orbit raising implies that after the satellite is deployed from the launch vehicle in a highly elliptical orbit, ion thrusters are used to transfer the satellite to the geostationary orbit. Ion thrusters make use of xenon atoms, which are ionized, electrically accelerated, and ejected to gain thrust. This transfer method is more mass efficient than chemical propulsion due to the higher specific impulse of the Xe ions. In this way, the payload mass of a satellite can be maximized. The disadvantage of EOR is that the transfer to the final orbit takes more time than a transfer by chemical propulsion. During transfer, the satellite slowly increases its perigee and therefore also slowly crosses the electron and the proton Van Allen belts. The central regions of the belts have to be passed, which causes a significant amount of displacement damage dose to the solar cells. The long GEO on-station phase takes place in the outer area of the outer electron belt. The displacement damage doses as well as particle fluences during EOR and GEO add up to the total mission values.

First of all, the particle environment which the solar cells will be exposed to during the mission is computed. For the computation, Spenvis is used [20]. Spenvis is the space environment information system of ESA. It is a useful tool and data base for many calculations regarding space environment. For the mission, a realistic EOR and GEO are chosen. The EOR mission phase is approximated by ten isochronous segments followed by the GEO mission phase. For the EOR phase, it is assumed that the starting orbit is $300\,\mathrm{x}35786\,\mathrm{km}$ with an inclination of $30\,^\circ$. The initial inclination depends on the launch site. At $0\,^\circ$ inclination, irradiation is at its maximum. Each of the ten EOR

segments shall be twenty days long. The overall transfer time sums up to 200 days. The perigee shall increase linearly from 300 to 35786 km. The apogee shall increase linearly from 35786 km to 55000 km at day 100 and then decrease again linearly to 35786 km. During the whole EOR transfer time, the inclination shall decrease linearly. These assumptions are a good approximation to realistic mission parameters [94]. The final GEO orbit is a circular orbit at 35786 km with $0\,^\circ$ inclination. The on-station time shall be 15 years. The values are given in Tab. 7.2.

segment	duration	perigee average km	apogee average km	inclination average °
1	20d	2074	37707	28.5
2	20d	5623	41550	25.5
3	20d	9172	45393	22.5
4	20d	12720	49236	19.5
5	20d	16269	53079	16.5
6	20d	19817	53079	13.5
7	20d	23366	49236	10.5
8	20d	26915	45393	7.5
9	20d	30463	41550	4.5
10	20d	34012	37707	1.5
11	15y	35786	35786	0

Table 7.2 Data of EOR orbit broken down in ten segments and GEO phase. The given EOR values are the average values computed for each segment phase.

The electron environment the solar cells are exposed to consists of electrons from the outer electron Van Allen belt during the GEO phase and from the outer and inner electron belts from the EOR phase. As environmental model, the standard model AE8 for solar maximum conditions is chosen with a confidence level of $84.135\,\%$, which means that the probability that the predicted fluence will not be exceeded is $84.135\,\%$. In Fig. 7.13a), the total fluence of electrons vs electron energy for a 200 day EOR phase is shown as well as for a 15 year GEO phase. The total electron fluence is dominated by the 15 year GEO phase electrons trapped in the outer Van Allen belt for electron energies up to app. 5 MeV. Above that energy, it is dominated by the EOR phase because the flux of high energy electrons is low in the outer area of the electron belt, which is where the GEO orbit is located.

For protons two different sources are important. There are protons trapped in a belt and also solar flare protons directly coming from the sun. The proton environment is computed with Spenvis using the standard models AP8 with solar minimum conditions for the protons trapped in the belt and ESP-PSYCHIC for the solar flare protons with a

confidence level of $84.135\,\%$. The proton environment is shown in Fig. 7.13b. The total proton mission fluence is dominated for energies from 0.1 MeV up to 0.4 MeV by trapped protons of the GEO phase. For energies from 0.4 MeV up to 4 MeV, trapped protons of the EOR phase determine the total fluence. Solar flare protons do not play a significant role up to 4 MeV because flare protons show low fluences for low energies compared to trapped protons. The reason for the trapped proton fluence during the 200-days-long EOR phase being higher than during the 15-year-long GEO phase between 0.4 and 4 MeV can be explained as follows: The proton Van Allen belt extension is restricted, i.e. 10 MeV protons are trapped in the belt only up to a height of app. 16000 km above Earth. For lower energetic protons, the maximum height extends further. This leads to the trapped proton fluence between 0.4 MeV and 4 MeV being dominated by the EOR phase where the solar cells directly transit the center of the proton belt, where also relatively low proton energies show high fluences. The inclination of the EOR orbits was chosen to minimize the EOR proton fluence. The EOR proton fluence would be even higher if the orbit had an inclination of $0\,^\circ$ because then the EOR orbit would lie in plane of the proton belt, which is the equatorial plane. For energies above 4 MeV, the total fluence is dominated by solar flare protons in the GEO phase. Flare protons from the EOR phase play only a minor role because the GEO phase is app. 27 times longer than the EOR.

To reduce the deteriorating effect of particle irradiation on solar cells, the cells are

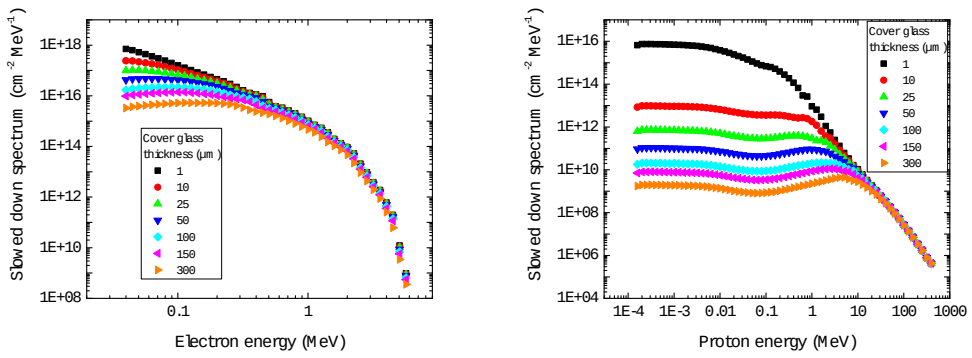

(a) Slowed down electron spectrum (b) Slowed down proton spectrum

Figure 7.14 Differential fluxes of (a) electron environment behind coverglass and (b) proton environment behind cover glass, also called slowed down spectra.

covered with protective borosilicate glass, so-called cover glasses [94]. It is stabilized against degradation in transmission by Ge doping. The top of the glass, which is attached to the solar cell with transparent silicone adhesive, is covered by anti-reflective coating. The cover glass and the cover glass adhesive cause wavelength-dependent absorption of photons. This absorption can change dependent on irradiation level. Due to the wavelength dependence of the absorption, not only the cell current decreases,

but also the current limiting subcell can change or the dose at which the limiting cell changes. This effect is typically small for 4J cells compared to the total cell degradation. It is, however, important to note that the calculations in this section are made under the assumption that there is no photon absorption caused by the cover glass, but only particle slowing resp. absorption, in other words shielding of the solar cell from energetic protons and electrons. The cover glass absorbs low energetic protons and decreases the kinetic energy of electrons and protons with energy high enough to transit the glass. In order to determine the effect of the particle environment to the solar cell, the absorption resp. reduction of energy by the different layers above and below the solar cell have to be taken into account. All shielding materials and thicknesses can be converted into equivalent cover glass thickness, which simplifies the calculation. Therefore, different cover glass thicknesses were included in the computation of the particle environment behind cover glass, the so-called slowed down spectrum (SDS). The lowest possible thickness in the software is $1\,\mu$m, therefore $1\,\mu$m and not $0\,\mu$m is the lowest value in the graph. The SDS is computed using the software SCREAM [47, 49] with the particle environments shown in Fig. 7.13.
The resulting SDS of electrons and protons are shown in Figs. 7.14a) and b). The differential fluence of low-energetic electrons decreases most in the low energy range. The cover glass is mostly effective for electron energies below approximately $0.5\,$MeV. At $0.5\,$MeV, the differential fluence is reduced by i.e. a $1\,\mu$m cover glass compared to a $100\,\mu$m cover glass from $5.6e15$ to $3.1e15\,\text{MeV}^{-1}\text{cm}^{-2}$, which is a reduction of $45\,\%$. The NIEL below an electron energy of app. $0.5\,$MeV is too low to cause displacements, see. Fig. 7.2, and therefore electrons below this energy range can be neglected resp. have a NIEL value close to $0\,\frac{\text{MeV cm}^2}{g}$ and therefore do not contribute to the total displacement damage computed with Eq. 7.1.

The shielding of the solar cells from protons is most effective below proton energies of approximately $10\,$MeV. As shown in Fig. 7.14b), cover glasses can reduce the differential fluence of protons by up to seven orders of magnitude. Since the NIEL of protons increases with lower energy down to a maximum of app. $5\,$keV, the reduction of differential proton fluence in this energy range exponentially reduces the displacement damage dose to the cell.
It is important to note that low-energetic protons incoming from space can be absorbed completely by the cover glass depending on their energy and the cover glass thickness and therefore cannot cause displacements. Nevertheless, a proton spectrum of continuous energies down to $0\,$eV will reach the solar cell behind the cover glass. The reason for this is that the continuous spectrum of protons energetic enough to transit the cover glass is decelerated by the glass and therefore reaches the solar cell with decreased energy.

The D_d caused by the SDS to the cell is computed using Eq. 7.1 and is shown in Fig. 7.15.

$$D_d = \int SDS(E) \times NIEL(E) dE \tag{7.1}$$

It is important to note that the so far computed electron D_d and the proton D_d cannot directly be summed up to get the total D_d. The summation has to follow the same rules as the proton and electron data were treated determining the characteristic degradation curve to obtain correct values. This means that the electron $D_{d,e}$ is converted into an equivalent proton dose $D_{d,e,eff}$ and then summed up with the proton dose $D_{d,p}$ as described in chapter 5.The D_d of electrons is converted into effective proton damage using the parameters of the fitting of the power at maximum power point of the 4J cell as shown in Fig. 7.11. For different cover glass thicknesses, different displacement

Glass thickness μm	$D_{d,p}$ $\frac{MeV}{g}$	$D_{d,e,eff}$ $\frac{MeV}{g}$	$D_{d,sum}$ $\frac{MeV}{g}$	RF P_{mpp}
1	2.54e14	6.92e9	2.54e14	0
10	8.99e11	6.65e9	9.05e11	0.21
25	9.65e10	6.27e9	1.03e11	0.57
50	2.13e10	5.76e9	2.70e10	0.77
100	5.39e9	5.00e9	1.04e10	0.87
150	2.66e9	4.42e9	7.07e9	0.9
300	9.13e8	3.21e9	4.12e9	0.93

Table 7.3 Displacement damage caused to a solar cell by protons and electrons after cover glass shielding of different thicknesses and infinite rear side shielding and corresponding remaining factors of power at maximum power point.

damage doses result. The displacement damages caused by electrons and protons after shielding is shown in Fig. 7.15. The D_d caused by electrons to a solar cell with a $1\,\mu$m cover glass compared to a $100\,\mu$m cover glass is reduced by $29\,\%$, with a $300\,\mu$m cover glass even by $55\,\%$. For protons, the situation is different: For low shielding thicknesses, the D_d caused by protons to solar cells is up to app. $1e4$ times higher than the one caused by electrons. On the other hand, cover glass shielding also has a much stronger effect on D_d caused by protons than on D_d caused by electrons. Behind a $100\,\mu$m cover glass, the D_d is reduced by five orders of magnitude and with $1e10\,\frac{\text{MeV}}{\text{g}}$ approximately equal to the electron D_d. For a cover glass thickness of $300\,\mu$m, the D_d is reduced by altogether five orders of magnitude compared to $1\,\mu$m shielding. The high proton D_d clearly results from the EOR phase. For solar cells in space and especially for solar cells with high proton irradiation as caused during EOR, cover glass is essential to reduce displacement damage. The displacement damages caused by electrons and protons as well as their sum is shown in Tab. 7.3. The displacement damage sum of effective electrons and protons after shielding of different thicknesses can be used to predict the

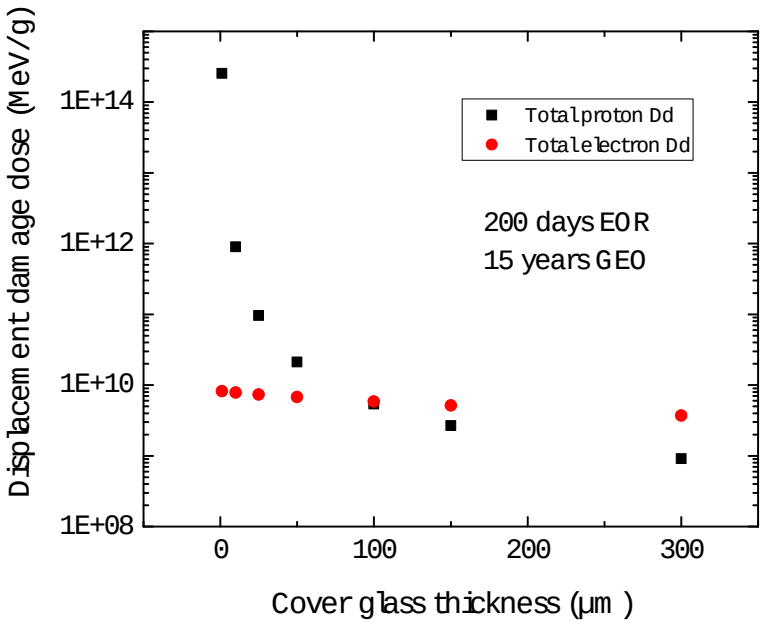

Figure 7.15 Total mission displacement damage dose for different cover glass thicknesses.

degradation of the power of a solar cell under irradiation as depicted in Fig. 7.16. To determine the influence of the total D_d on the power at maximum power point, the P_{mpp} degradation curve determined in Fig. 7.11 is used. The result is shown in Fig. 7.16. The total doses of the three cover glass thicknesses 50, 100, and $300\,\mu$m were computed and highlighted .The resulting remaining factor of the P_{mpp} of a 4G32 solar cell are determined to be 0.77, 0.87, and 0.93. These remaining factors result for different cover glass thicknesses after a 200 day long EOR phase through the Van Allen belts and a 15 year long GEO phase.

The biggest uncertainty in this calculation is the actual particle environment of the mission because only a limited data set of the particle environment around Earth is available and furthermore the Van Allen belts are not static but can change in time. Another uncertainty is the uncertainty of the determined cell degradation curve.

7.5 Conclusion

The degradation behavior of 4J and 1J isotypes was analyzed and compared. The degradation behavior of the open-circuit voltage was discussed for all isotype cells and it was found that the sum of the open-circuit voltages agree well with the open-circuit voltage of the 4J cell for all irradiation doses. For J3 and J4, similar threshold energies were found as for their comparable counterparts of the 3J cell, the middle, and the bottom cell. For J2 and especially for J1, high values of threshold energies for atomic displacement were found which has its origin most likely in the element aluminum

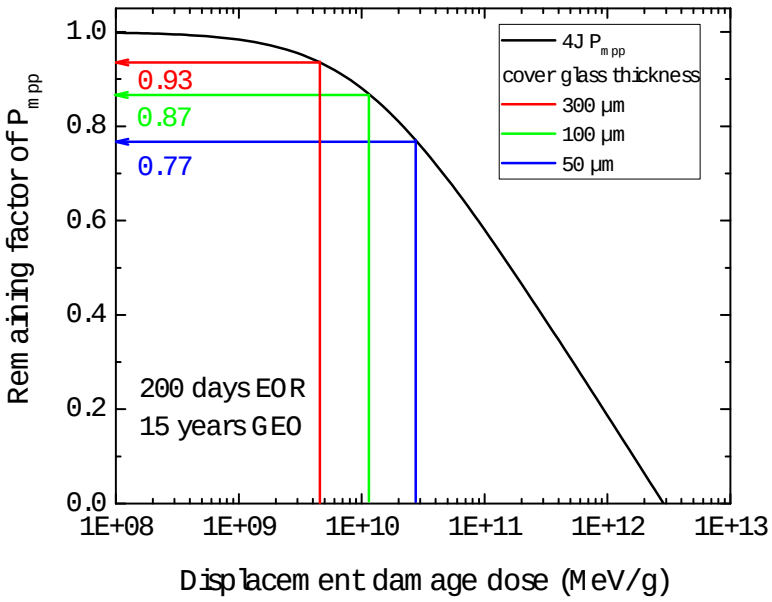

Figure 7.16 Remaining factor of 4G32 solar cells for power at maximum power point after EOR and 15 year GEO phase for different cover glass thicknesses.

and its high threshold energy for atomic displacement. The analysis of the short-circuit current was performed including the correction of the BOL current values for luminescent coupling between J3 and J4. The comparison of isotype and 4J cells revealed that the current limitation of the 4J cell changes from J1 to J3 at app. $D_d = 1e10 \frac{\text{MeV}}{\text{g}}$. Furthermore, it was found that in a dose range where the 4J cell is J3 limited, it generates a higher current than the J3 isotype cell in the same dose range. The origin of this difference was found to be different operating points of the J3 cell in a 4J cell stack and a J3 isotype cell at short-circuit state in combination with voltage-dependent photocurrent of irradiated cells. The power at maximum power point is higher in sum for the 1J cells than for the 4J cells. The origin of this difference was found to be the different maximum power points of each subcell or isotype cell. Finally, the degradation of power of a shielded 4J cell was investigated. It was assumed that the 4J cell was transferred by EOR to the GEO orbit. The particle environments for these two mission segments were computed as well as the environments behind different cover glass shielding thicknesses. It was found that in the whole energy range the total electron dose was dominated by the electrons trapped in the Van Allen belt, which is where the GEO orbit is located. The proton environment was dominated up to app. $4\,\text{MeV}$ by protons trapped in the belt. They damaged the solar cell during the EOR phase. Above $4\,\text{MeV}$, the total proton environment was dominated by solar flare protons during the GEO phase. The displacement damage dose to the solar cell by electrons and by protons was analyzed separately and it was found that at approximately $100\,\mu\text{m}$ equivalent cover

glass thickness, the amount of damage caused by electrons was equal to the amount of damage caused by protons. The total degradation of the power at maximum power point was analyzed for different cover glass thicknesses on this mission. It was found that the power at maximum power point degrades to app. $87\,\%$ with $100\,\mu$m cover glass. With the analysis showing different degradations for different cover glass thicknesses, a trade-off between energy and mass of a solar generator can be made.

8 Characterization of subcells of particle irradiated multi-junction cells

8.1 Introduction

So far it was necessary to use isotype cells to do a subcell radiation characterization of MJ cells. Now a method is introduced which allows to extract the SJ data from MJ stacks. In order to fully characterize an MJ cell, the current-voltage behavior of the individual subcells shall be characterized in detail. This is not trivial because an MJ cell has only two terminals located at the top and bottom of the cell stack and the individual subcells are not directly accessible. There are methods to gain access to the subcells: One method to determine the subcell voltages and subcell parameters of MJ cells is described by Rau et al. [95] using the electroluminescence spectrum. The EL spectrum of each subcell has to be measured along with high precision EQE measurements [96, 97]. Instead of the EL spectrum, also the PL spectrum can be analyzed as described by Alonso et al. [98]. Both methods have limitations. For indirect semiconductors such as germanium or silicon as well as for semiconductors containing a high density of defects such as for particle irradiated solar cells, there is limited radiative recombination and therefore the EL and PL signals are too weak to be used to determine the MJ subcell behavior.

Therefore, a different method is used for analyzing particle irradiated subcells of MJ cells. For characterizing V_{oc} of BOL and irradiated MJ cells, the method using pulsed laser light is applied, which was first described using BOL 3J cells in [99]. In [100–102], the pulsed laser method is applied to 3J and 4J cells. The results of BOL cells generated using pulsed lasers were compared to the results generated using the EL-V_{oc} method and it was shown that the methods provide identical results. It is even possible to compute the subcell capacitance using the rise time of the voltage [103].
The advantage of the pulsed laser method is that also the V_{oc} of irradiated subcells is accessible. For this reason, pulsed lasers are used in the following to characterize 3J and 4J cells irradiated with high doses of electrons and protons. It shall be verified that

it is possible to determine the V_{oc} of the subcells using pulsed lasers for highly irradiated solar cells with fluences up to $2e16\frac{1}{\text{cm}^2}$ 1 MeV electrons. Additionally, the dark current-voltage characteristics of the subcells shall be determined, which are otherwise inaccessible in MJ cells.

The applicability of the pulsed laser method to determine the correct subcell behavior as well as the results themselves are verified in two ways. Firstly, the photocurrent-V_{oc} curves of the individual subcells of a 4J cell are compared with the individual DIV curves of equally irradiated isotype cells.
Secondly, the individual subcell photocurrent-V_{oc} curves from both irradiated 3J and 4J cells are fitted. The resulting fit parameters are used to simulate the corresponding 3J resp. 4J cell in SPICE [104] resulting in a simulated DIV curve of the whole respective MJ cell. This DIV curve simulated by the subcell parameters gained from the $I_{ph} - V_{oc}$ curves is then compared to the actually measured DIV curve of the 4J cell. The results are shown in the following.

8.2 Subcell voltage determination with pulsed lasers

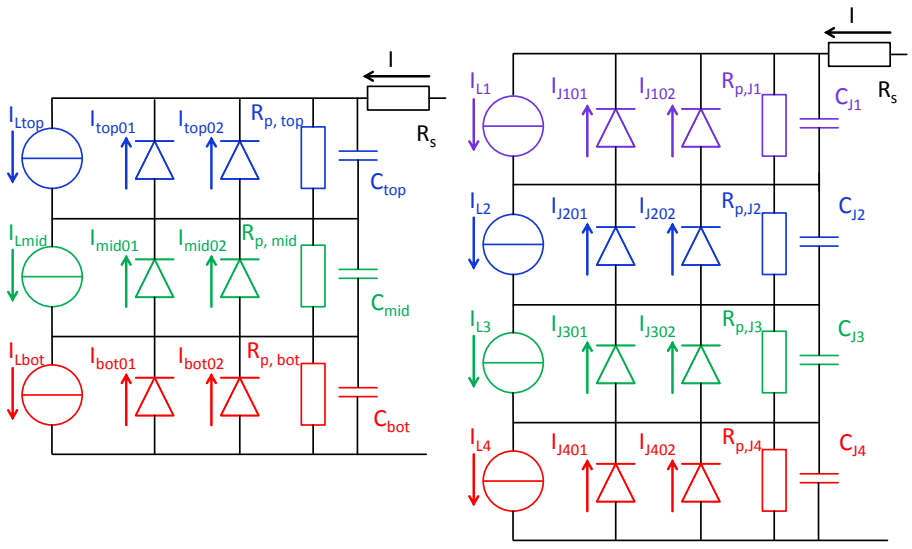

(a) 3J cell (b) 4J cell

Figure 8.1 Equivalent circuit of (a) a 3J and (b) a 4J cell consisting of a current source, two diodes representing recombination in the neutral and in the space charge region, a shunt resistance, and a capacitance per subcell as well as an overall series resistance.

The principle of the measurement of V_{oc} is based on the fact that each pn-junction exhibits a capacitance associated with the space charge region. Taking the capacitance

of a subcell into account, the equivalent circuit of a solar cell consists of a current source, a diode representing recombination in the neutral regions, a diode representing recombination in the SCR, a parallel resistance representing shunts in the cell, a capacitance and a series resistance. An equivalent circuit diagram of a 3J and a 4J cell is shown in Fig. 8.1a) and b). The subcell equivalent circuits include the capacitances C_{J1} to C_{J4}, resp. C_{top} to C_{bot}. These capacitances can be charged by laser pulses which

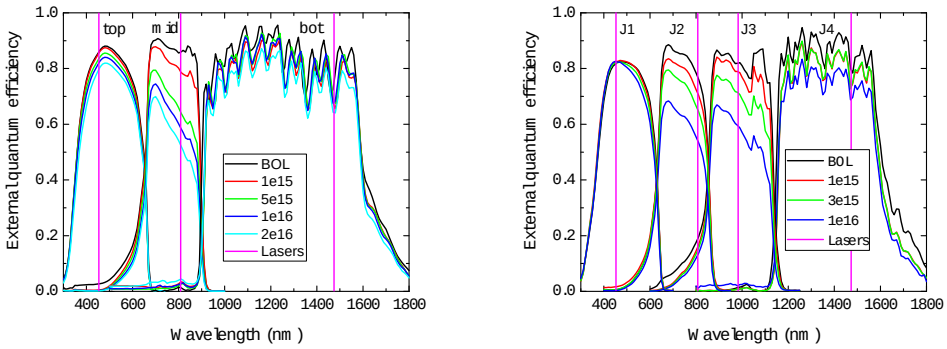

(a) 3J cells (b) 4J cells

Figure 8.2 EQE of (a) 3J and (b) 4J cells BOL and irradiated with different fluences of 1 MeV electrons together with the wavelengths of the lasers used to generate electron-hole pairs in the individual subcells.

are fully absorbed in the respective junctions. The charging of a junction capacitance by laser illumination takes place on a much shorter timescale than the charging of the non-illuminated junction capacitances, which is the reason why an individual subcell voltage can be measured. For the characterization of the V_{oc} of the subcells of MJ cells, three resp. four lasers are used. The lasers have wavelengths of 450 nm, which is absorbed in the top cell resp. J1, 803 nm, which is absorbed in the mid cell resp. J2, 975 nm, which is absorbed in J3 and not used for 3J characterization and 1470 nm, which is absorbed in the bot cell resp. J4. The wavelengths are shown in Fig. 8.2 as straight lines together with the EQEs of BOL and electron irradiated 3J (a) and 4J (b) cells. The wavelengths are chosen in a way that each laser is absorbed in a specific subcell. To illuminate the solar cell homogeneously, the laser beams are widened and homogenized by optics. Further details have been summarized in chapter 3.

Starting with illuminating a 4J cell homogeneously with a 1470 nm laser pulse which is fully absorbed in the junction J4, the voltage measured at the top and bottom terminals of the MJ cell is depicted in Fig. 8.3. The laser is switched on at $t = 0.25$ ms and the V_{oc} instantly rises at that moment because the charging of C_{J4} takes place in the time range of the rise time of the laser which amounts to microseconds. A small measurement current can flow through the 4J cell because of the other three junction capacitances C_{J1}-C_{J3} which are not fully charged at this moment. In the millisec-

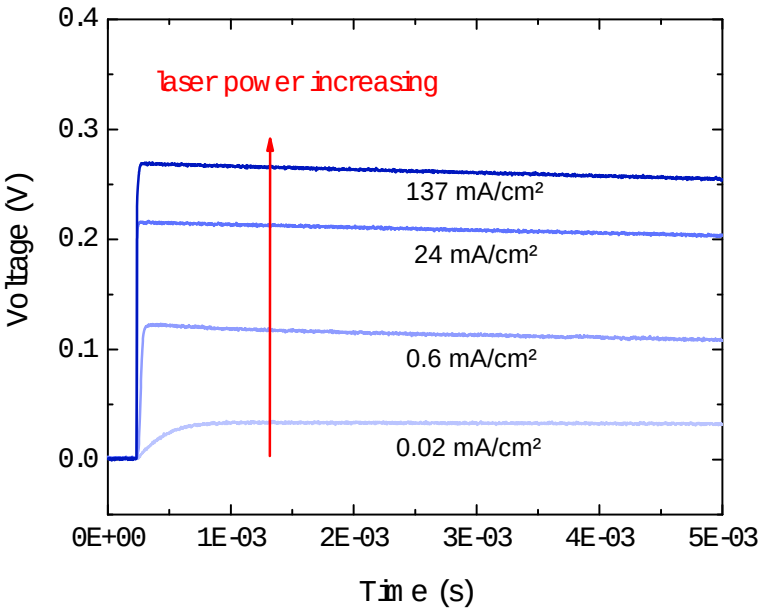

Figure 8.3 Voltage measured at the terminals of a 4J cell while pulses of a $1470\,\mathrm{nm}$ laser with different powers are illuminating the cell.

onds after $t = 0.25\,\mathrm{ms}$ the voltage decreases slowly because the charging of the other junctions C_{J1} - C_{J3} takes place. The voltage logging device has an internal resistance of $1\,\mathrm{M\Omega}$ to prevent discharging over the measurement device itself in this time range. The illumination intensity of the laser can be modified by changing the laser power. Larger illumination intensities correspond to larger voltages resp. photocurrents generated, which is important for measuring subcell characteristics over a wider range of voltages resp. photocurrents. In Fig. 8.3, the results of three laser pulses with different intensities are shown.

For the subcells J3 to J1, the measurement is complicated by luminescent coupling. If a 4J cell is irradiated with homogeneous light of i.e. $975\,\mathrm{nm}$, the measured voltage consists of the voltage generated in J3, which is where the light is absorbed, as well as a small amount of voltage generated in J4 due to luminescent recombination of electron-hole pairs in J3. The same effect occurs for J2 and J1 affecting cells with smaller bandgap. To avoid the effect of luminescent coupling from J3 to J4, the $1470\,\mathrm{nm}$ laser is switched on with maximum power shortly before illuminating the 4J cell with different powers of $975\,\mathrm{nm}$ pulses. By doing so, luminescent coupling from J3 to J4 still happens, but the additionally generated voltage by the additional light is negligible because the voltage generated by a solar cell is logarithmically dependent on the incoming photon flux. In Fig. 8.4, the continuation of the voltage measurement of Fig. 8.3 is depicted. Firstly, $1470\,\mathrm{nm}$ pulses of different powers subsequently irradiate the cell and the voltage is measured, which is represented by the blue lines. For the measurement of the voltage

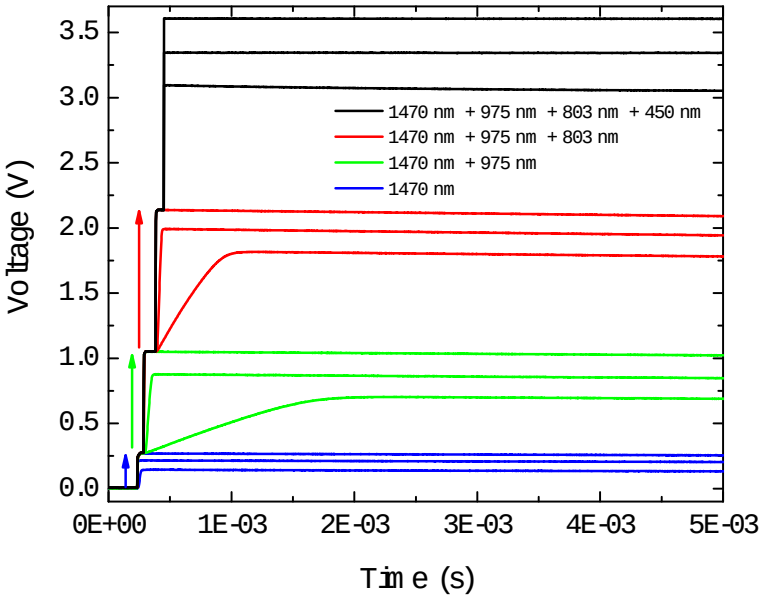

Figure 8.4 Voltage measured at the terminals of a 4J cell while pulses of different lasers with different powers are illuminating the cell cumulatively.

of J3, first the $1470\,\text{nm}$ was switched on at its maximum power and after $5\,\mu\text{s}$, the $975\,\text{nm}$ laser pulse was switched on with relatively small power, which resulted in the undermost green curve. The $975\,\text{nm}$ power is so low that it takes approximately $2\,\text{ms}$ to charge the capacitance of J3 C_{J3} and the voltage plateau is reached. Then both lasers are turned off. The same procedure is repeated always with a maximum power $1470\,\text{nm}$ pulse and a $975\,\text{nm}$ pulse of different powers $5\,\mu\text{s}$ later until the maximum power of the $975\,\text{nm}$ laser is reached. To measure the voltage generated by J2, firstly the $1470\,\text{nm}$ laser and secondly the $975\,\text{nm}$ laser are switched on with maximum power. Thirdly, the $803\,\text{nm}$ laser is subsequently switched on with different powers. The same procedure is performed to determine the J1 voltage with all four lasers switched on one after another. Different laser powers are used to generate different voltages. To keep the graph clear and well-ordered, only three curves per subcell are shown in Fig. 8.4. To acquire more data points, approximately ten different laser intensities are used per subcell. For the lowest laser intensities shown in Fig. 8.4, charging curves are measured before the voltage plateaus are reached. The reason for that is that the illumination is so low that the charging time of the subcell is within the time range of the laser pulse. In the curves depicted, the voltage plateau is still reached. For even lower illumination levels, the voltage plateau cannot be reached within the time of the pulse and no reliable voltage determination is possible. Therefore, a minimum level of illumination is needed using the pulsed laser method.

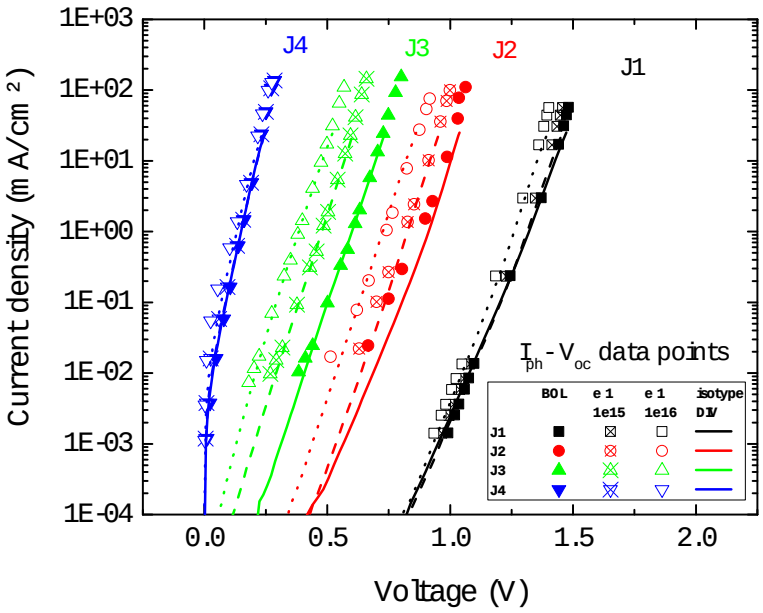

Figure 8.5 I_{ph}-V_{oc} data points of subcells of 3 4J cells: BOL, $1e15\,\frac{1}{\text{cm}^2}$ and $1e16\,\frac{1}{\text{cm}^2}$ 1 MeV electrons. The curves show the DIV curves of 12 isotype cells.

8.3 Subcell dark current-voltage characteristics determination

To determine the photocurrents corresponding to the so determined voltages, the experimental approach described in [99] is used. One condition has to be fulfilled: For the measurement of the generated current of a subcell of an MJ cell, all other subcells have to generate at least or more than the amount of current generated by the subcell under test. In other words, the subcell under test has to be the current limiting subcell. This would be the requirement if luminescent coupling (LC) was non-existing. Due to the existence of LC in our BOL cells, the requirement is more strict: Considering LC, for all subcells under test but J1, the requirement is that the current generated by the subcells not under test should not be higher but equivalent to the current of the subcell under test. The reason behind this will be described in the following. For the measurement of the photocurrent of J1, J2-J4 are illuminated with their respective lasers at maximum laser power. Then J1 can be illuminated with different laser powers and is always the current limiting cell up to a certain J1 laser power. For the determination of the photocurrent of J2, J3 and J4 are illuminated again with maximum laser power of the respective lasers. An illumination of J1 with maximum power is possible but would falsify the measurement due to luminescent coupling from J1 to J2. To determine the correct photocurrent generated in J2 at a certain laser power of the J2 laser ($803\,\text{nm}$), the J1 laser is switched on starting at a high illumination power. Decreasing the J1

laser power while measuring the external photocurrent I_{ph} will result in a constant I_{ph} as long as J2 is current limiting. While continuing the decrease of the J1 laser power, the current I_{ph} will start to decrease at a certain power level of the J1 laser. This is the point where the subcells J1 and J2 generate the same amount of current and are therefore current-matched. Due to the extraction of all the current generated in J1, no more radiative recombination takes place in J1 and therefore no luminescent coupling from J1 to J2. The photocurrent measured is the photocurrent generated from the J2 laser in J2. The same procedure is applied to determine the photocurrents of J3 and J4. As a result, the photocurrents of all subcells are determined. The current and voltage data points of the subcells of BOL 4J cells and 4J cells irradiated with $1e15\,\frac{1}{\mathrm{cm}^2}$ and $1e16\,\frac{1}{\mathrm{cm}^2}$ 1 MeV electrons are shown in Fig. 8.5. The filled datapoints originate from a BOL 4J cell, the crossed and the empty datapoints from two irradiated 4J cells. These data points represent the DIV curves without resistive influence of the subcells which are otherwise not accessible to measurement.

To verify the I_{ph}-V_{oc} data gained with the pulsed laser method for BOL and irradiated 4J cells, the determined data points are compared with measured DIV curves of 4J isotype cells representative of the 4J subcells and equivalently particle irradiated. The DIV data of the isotype cells is shown as straight, dashed, and dotted lines in Fig. 8.5. Note again that the lines in Fig. 8.5 are not fits to the determined data points, but separately measured data of isotype cells. The data from the isotype cells and from the 4J cells of BOL J1 and irradiated J1 fits well. The data points and DIV curves of J2 do fit well above a current density of approximately $1\,\frac{\mathrm{mA}}{\mathrm{cm}^2}$. Below this limit, the data points show a higher shunt resistance than the data lines. Considering that the data points show no resistive influence, it is possible that this difference originates rather from an intrinsically higher shunt resistance of the 4J cells than of the J2 isotype cells. For J3 and J4, the results again fit well together. In conclusion, it is verified that the not directly accessible DIV curves of the subcells of BOL and electron irradiated 4J cells are accessible with the pulsed laser method.

8.4 SPICE simulation of 3- and 4-junction cells

Now that the method of determining $I_{ph} - V_{oc}$ or DIV curves without resistive influence of subcells has been introduced, these curves shall be determined on a larger scale on 3J and 4J cells BOL and irradiated with protons and electrons. The resulting $I_{ph} - V_{oc}$ data of 3J cells is shown as data points in Fig. 8.6a) resp. b) for cells irradiated with 1 MeV electrons resp. protons.

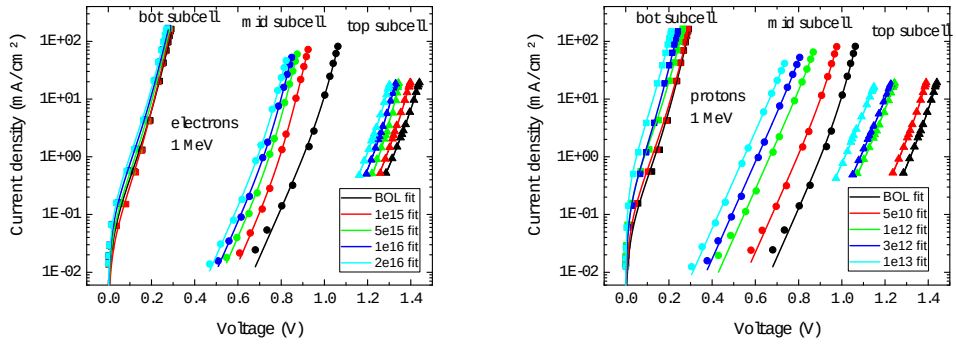

(a) (b)

Figure 8.6 I_{ph}-V_{oc} data points of subcells of 3J cells BOL and irradiated with (a) 1 MeV electrons resp. (b) 1 MeV protons. The lines are fit curves using the simplified 2-diode-model Eq. 8.1.

The curves in the Figure are fits to the data points using the simplified two-diode model Eq. 8.1.

$$I = I_{01}(\exp \frac{eV}{k_B T} - 1) + I_{02}(\exp \frac{eV}{2k_B T} - 1) \tag{8.1}$$

The curves fit the determined data points well. Only for the middle cell curves, the data points are slightly above the fit curves, which is an indication that these cells have a non-infinite shunt resistance. As a result of the fit, the parameters I_{01} and I_{02} are determined.

In Fig. 8.7a) resp. b), the results of the $I_{ph} - V_{oc}$ data of 4J cells are shown for cells irradiated with 1 MeV electrons resp. protons. For the 4J cells, again, the curves fit the

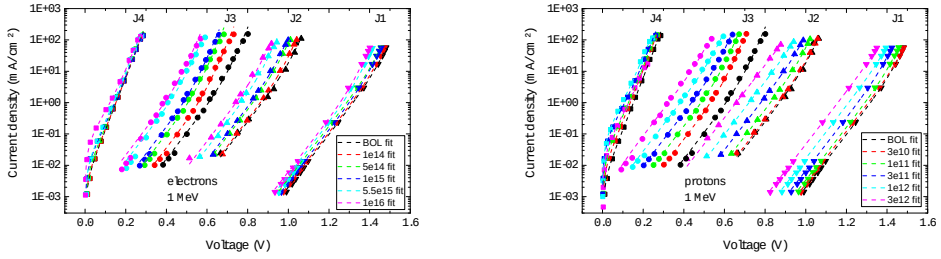

(a) (b)

Figure 8.7 I_{ph}-V_{oc} data points of subcells of 4J cells BOL and irradiated with (a) 1 MeV electrons resp. (b) 1 MeV protons. The lines are fit curves using the simplified 2-diode-model Eq. 8.1.

data well and the parameters I_{01} and I_{02} are determined.

To verify the resulting subcell curves, the determined recombination current densities I_{01} and I_{02} of the subcells of irradiated 3J and 4J cells are used as input data in the

program SPICE to simulate DIV curves of the resp. MJ cell. The equivalent circuit of the 3J resp. 4J cell used for the DIV curve simulation is depicted in Fig. 8.8.

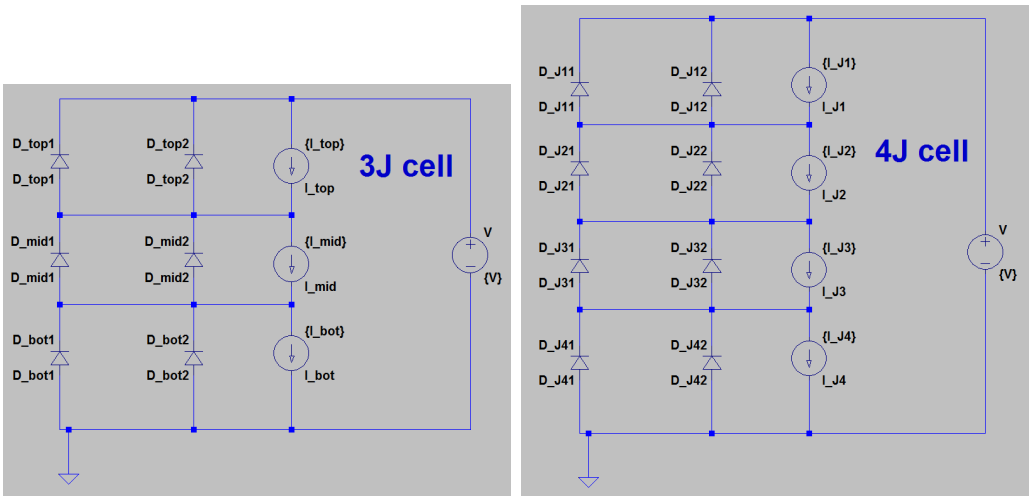

(a) 3J cell (b) 4J cell

Figure 8.8 Simplified equivalent circuits of (a) a 3J and (b) a 4J cell.

As in the simplified two-diode model, the subcells of the multijunction cells consist of a current source and two diodes representing recombination in the SCR (I_{02}) and recombination in the neutral region (I_{01}).

The resulting simulated DIV curves of the BOL and irradiated 3J cells are shown in Fig. 8.9a) and b) for irradiation with electrons resp. protons. The lines represent the curves generated by the SPICE simulation using the parameters I_{01} and I_{02} determined by the fit of the I_{ph}-V_{oc} data points. The data points are the DIV data of the 3J cells simply measured with a Keithley source meter. The SPICE curves match well with the data points from the maximum measured data points down to a current density of approximately $10^{-5}\ \frac{\text{mA}}{\text{cm}^2}$. Then the simulation begins to diverge from the measured data points. This divergency is caused by a low shunt resistance present in the MJ cell. This low shunt resistance was not noticed within the measurement of the subcells because it is not detectable with the pulsed laser measurement method.

The results of the 4J cell simulation are shown in Fig. 8.10a) and b) for irradiation with electrons resp. protons.

Also for 4J cells, the SPICE curves match well with the data points from the maximum measured data points.

8.5 Conclusion

In this chapter, a method for determination of subcell open-circuit voltages, subcell current recombination densities, and subcell DIV curves was applied using pulsed lasers.

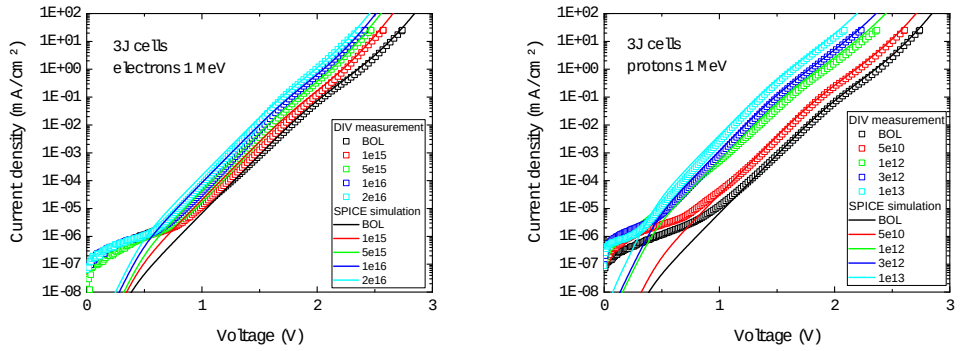

(a) 1 MeV electron irradiation (b) 1 MeV proton irradiation

Figure 8.9 Comparison of data points representing the dark current-voltage characteristics of 3J cells BOL and irradiated with (a) electrons resp. (b) protons and data curves representing the SPICE simulation of the 3J cell dark current-voltage characteristics. As input parameters for the SPICE simulation, the recombination current densities I_{01} and I_{02} determined by the pulsed laser method are used.

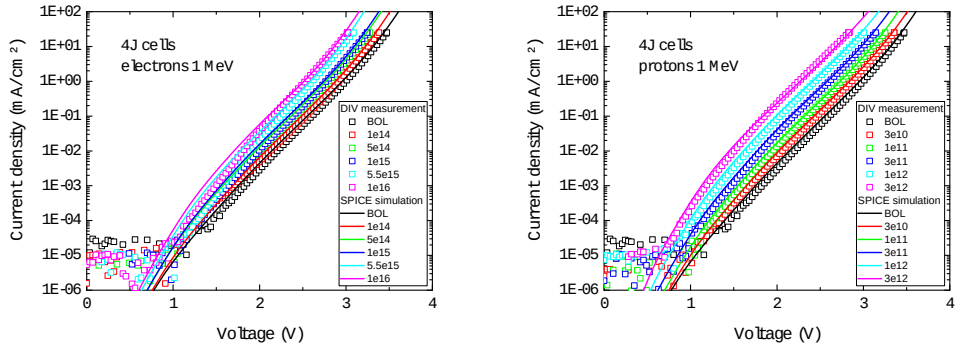

(a) 1 MeV electron irradiation (b) 1 MeV proton irradiation

Figure 8.10 Comparison of data points representing the dark current-voltage characteristics of 4J cells BOL and irradiated with (a) electrons resp. (b) protons and data curves representing the SPICE simulation of the 3J cell dark current-voltage characteristics. As input parameters for the SPICE simulation, the recombination current densities I_{01} and I_{02} determined by the pulsed laser method are used.

The method was found suitable for BOL, electron, and proton irradiated 3J and 4J cells. It was applied to 4J cells for the first time. The results match the ones obtained for isotype cells.

9 Summary and Outlook

9.1 Summary

Within the framework of this thesis, several hundred 3J, 4J, and isotype 1J cells were irradiated with protons and electrons to study their degradation behavior. The cells were characterized electrically before and after irradiation.

1) An adapted solar cell degradation data analysis method based on the displacement damage dose method with variable threshold energy for atomic displacement was developed. To apply the analysis method, a program was written in Matlab code to compute the NIEL for different threshold energies for atomic displacement. It was found that the adapted solar cell degradation data analysis described above results in a collapse of the degradation data points of different electron energies when the appropriate threshold energy for atomic displacement is used in the NIEL calculation. This is different to the so far used D_d method, which needed an additionally introduced exponent to bring the electron degradation data to a collapse. This exponent is obsolete when this method is used. It was found that the threshold energy for atomic displacement is dependent on the semiconductor material and the lowest energy defect type introduced by the particles.

2) The threshold energies for atomic displacement were found for all subcells of the used 3J and 4J cells, which allows insight into the dominating kind of defects generated using only standard electrical characterization.

3) An unexpected result of this work was the finding of a voltage-dependent photocurrent generated by particle irradiated GaAs cells. At begin of life, their photocurrent is constant and not voltage dependent. With increasing particle irradiation, the photocurrent becomes increasingly dependent on voltage. The origin for this behavior was found in the voltage dependence of the space-charge region of the cell in combination with a very low minority charge carrier lifetime. By lowering the minority charge carrier lifetime by irradiation, the photocurrent generated in the space-charge region gets more dominant compared to the photocurrent generated outside of the SCR. Since the width of the space-charge region is voltage-dependent, the overall photocurrent, which is partly generated in the SCR, becomes voltage dependent as well.

4) The displacement damage dose method is applicable for the analysis of the degradation data of 4J cells. This is especially important since 4J cells will be implemented in

future electric orbit raising missions in space. During the electric transfer to the final satellite orbit, the particle damage is increased considerably compared to a chemical transfer. We furthermore report on the full characterization of 4J cells with electrons and protons within the expected damage range of such missions. The expected damage of such a mission was computed within this thesis as an example using the 4J cell characterization in combination with the tool SPENVIS, which offers particle flux data of the space around Earth. Finally, the damage on solar cells was computed dependent on the thickness of cover glasses, which are used for the shielding of solar cells in space. 5) Within this work, it was shown that it is possible to extract the subcell open-circuit voltages and the subcell dark current-voltage characteristics from 3J and 4J cells. This was possible using an experimental setup with high power lasers whose wavelengths were chosen so that they were absorbed in one subcell only. Contrary to cells with a low defect density, known subcell characterization methods, which make use of the EL or PL spectrum, are not applicable for irradiated cells due to the weak radiative recombination in irradiated solar cells. Therefore, this new method using pulsed lasers is especially useful for characterizing the subcells of irradiated multi-junction solar cells.

9.2 Outlook

For future generations of thin-film solar cells, the displacement damage dose method including a variable threshold energy for atomic displacement can be applied for degradation data analysis. It provides a reliable way to determine the cell type degradation albeit requiring a minimum amount of test data.
The 4J cell degradation behavior determined in this thesis can be used to predict the degradation of these cells in space. The first cells of this kind will reach space on a commercial satellite in 2022. A degradation analysis according to the same procedure used for 4J cells in this thesis can be applied to all kinds of future cell generations when there is at least a minimum amount of degradation data from particle accelerator tests and particle data from the orbit(s) of interest.
The experimental setup for subcell investigation with pulsed lasers can be used to determine subcell properties of other cells. The only constraint is that the wavelength of the lasers have to fit the bandgap of the subcells. If that is not the case for other cells of interest, the laser setup can be extended with additional lasers.

Some topics were not within the frame of this thesis, but could nevertheless be of interest for future research.

Molecular dynamics simulations can be used to simulate what kind of defects are generated during particle irradiation. This simulation result could be compared to experimental data. The experimental data could be generated by testing the irradiated

solar cells with deep-level transient spectroscopy. This would give insight into the properties of the present electrically active defects.

The solar cells could be annealed at different temperatures to obtain information about the self-healing process of different defects in different materials at different temperatures. On the one hand, this data is of course useful to learn about the physical properties of the defects. On the other hand, it could also have technical relevance for missions to the sun or to Mercury where solar cells are operated at temperatures of up to 175°C.

In this thesis, the degradation of solar cells under proton and electron irradiation was determined because these are the most prominent particle types in space. To gain insight into the behavior of solar cells under other kinds of particle irradiation, cells could be irradiated with particles such as neutrons, alpha particles, or muons. These particles are also present in space but in a very low density compared to protons and electrons. Nevertheless, it would be interesting what kinds of defects are generated by these particles and if the cell degradation can be simulated and analyzed by the same methods as proton and electron irradiation or if the methods have to be adapted.

Annex

NIEL for a 1-element material

```
function NIEL1(particle,lattice,Ed)

%x,y boxes
Eparvec=logspace(-4,4,300); %Energy vector in MeV
NIEL1mat = zeros(2,size(Eparvec,2)); %solution matrix

%calculation
 for i = 1:size(Eparvec,2)
    Epar = Eparvec(i);
    %write in the solution matrix
    NIEL1mat(1,i) = Epar;
    NIEL1mat(2,i) = NIEL(Epar,particle,lattice,Ed);
 end

%plot
    loglog(NIEL1mat(1,1:end),NIEL1mat(2,1:end),'LineWidth',5,
       'DisplayName',sprintf('␣%s␣on␣%s,␣␣␣T_{d,%s}␣=␣%.0f␣eV
       ',particle,lattice,lattice,Ed));

font = 'Arial';
fontsizelegend = 18;
fontsizelabel = 38;

set(gca,'FontSize',fontsizelabel,'xscale','log'); %tick label
    fontsize
set(gcf, 'Position', get(0,'Screensize')); % Maximize figure.
xlabel({'particle␣energy␣(MeV)'},'FontSize',fontsizelabel,'
   FontWeight','bold','FontName',font)
```

```
ylabel({'NIEL␣(MeV␣cm^2␣g^{-1})'},'FontSize',fontsizelabel,'
   FontWeight','bold','FontName',font)
lh = legend('-DynamicLegend','Location','southwest'); %to get
    legend from displayname
set(lh, 'Box', 'off','Fontname',font,'FontSize',
   fontsizelegend);
axis([1e-1 1e1 1e-7 1e-4])

%grid
grid on;
xt = log10(get(gca,'XTick')); %for xticks 1e8 instead of 10^8
set(gca,'XTickLabel',sprintfc('1e%i',xt(1):xt(2)-xt(1):xt(
   numel(xt)))); %for xticks 1e8 instead of 10^8
yt = log10(get(gca,'YTick')); %for xticks 1e8 instead of 10^8
set(gca,'YTickLabel',sprintfc('1e%i',yt(1):yt(2)-yt(1):yt(
   numel(yt)))); %for yticks 1e8 instead of 10^8
ax = gca;
ax.GridAlpha = 0.75;
ax.MinorGridAlpha = 0.75;
end
```

NIEL for a 2-element material

```
function NIEL2(particle,lattice1,ratio1,Ed1,lattice2,ratio2,
   Ed2)

%constants
Aga=69.723;
Aas=74.92160;
Ain=114.818;
Aph=30.973761998;
Age=72.630;
Asi=28.084;
Aal=26.9815385;
An=14.00643;
Acd=112.411;
Ate=127.6;
```

```
%x,y boxes
switch particle
    case 'p'
        Eparvec=logspace(-4,4,1000); %Energy vector in MeV
    case 'e'
        Eparvec=logspace(-0.8,4,1000); %Energy vector in MeV
    otherwise
        Eparvec=logspace(-4,4,1000); %Energy vector in MeV
end
NIEL2mat = zeros(2,size(Eparvec,2)); %solution matrix

%calculation
 for i = 1:size(Eparvec,2)
    Epar = Eparvec(i);
    %write in the solution matrix
    NIEL2mat(1,i) = Epar;
    NIEL2mat(2,i) = 1/(ratio1*Al1+ratio2*Al2)*(Al1*ratio1*
       NIEL(Epar,particle,
                lattice1,Ed1)+Al2*ratio2*NIEL(Epar,particle,
                   lattice2,Ed2));
 end

%plot
font = 'Arial';
fontsizelegend = 27;
fontsizelabel = 45;
loglog(NIEL2mat(1,1:end),NIEL2mat(2,1:end),'LineWidth',5,'
   DisplayName',
sprintf('␣%s␣on␣%s%s,␣␣␣T_{d,%s%s}␣=␣%.0f␣eV',particle,
   lattice1,lattice2,
lattice1,lattice2,Ed1));
set(gca,'FontSize',fontsizelabel,'xscale','log','XTick'
   ,[10^-4 10^-3 10^-2
 10^-1 10^0 10^1],'YTick',[10^-7 10^-5 10^-3 10^-1 10^1]); %
    tick label
fontsize
set(gcf, 'Position', get(0,'Screensize')); % Maximize figure.
xlabel({'Particle␣energy␣(MeV)'},'FontSize',fontsizelabel,'
   FontName',font,
'Color','black')
```

```
ylabel({'NIEL␣(MeV␣cm^2␣g^{-1})'},'FontSize',fontsizelabel,'
   FontName',font,
'Color','black')
lh = legend('-DynamicLegend','Location','southwest'); %to get
    legend from
displayname
set(lh, 'Box', 'off','Fontname',font,'FontSize',
   fontsizelegend);
axis([1e-4 1e1 1e-7 1e1])

%grid
grid on;
xt = log10(get(gca,'XTick')); %for xticks 1e8 instead of 10^8
set(gca,'XTickLabel',sprintfc('1E%i',xt(1):xt(2)-xt(1):xt(
   numel(xt))),
'XColor','black','GridAlpha',0.5); %for xticks 1e8 instead of
    10^8
yt = log10(get(gca,'YTick')); %for xticks 1e8 instead of 10^8
set(gca,'YTickLabel',sprintfc('1E%i',yt(1):yt(2)-yt(1):yt(
   numel(yt))),
'YColor','black'); %for yticks 1e8 instead of 10^8
```

NIEL for a 3-element material

```
function NIEL3(particle,lattice1,ratio1,Ed1,lattice2,ratio2,
   Ed2,lattice3,ratio3,Ed3)

%constants
Aga=69.723;
Aas=74.92160;
Ain=114.818;
Aph=30.973761998;
Age=72.630;
Asi=28.084;
Aal=26.9815385;
An=14.00643;

%x,y boxes
```

```
switch particle
    case 'p'
        Eparvec=logspace(-4,4,300); %Energy vector in MeV
    case 'e'
        Eparvec=logspace(-1,4,300); %Energy vector in MeV
    otherwise
        Eparvec=logspace(-4,4,300); %Energy vector in MeV
end
NIEL3mat = zeros(2,size(Eparvec,2)); %solution matrix

%calculation
 for i = 1:size(Eparvec,2)
    Epar = Eparvec(i);
    %write in the solution matrix
    NIEL3mat(1,i) = Epar;
    NIEL3mat(2,i) = 1/(ratio1*Al1+ratio2*Al2+ratio3*Al3)*(Al1
       *ratio1*NIEL(Epar,particle,lattice1,Ed1)+Al2*ratio2*
       NIEL(Epar,particle,lattice2,Ed2)+Al3*ratio3*NIEL(Epar,
       particle,lattice3,Ed3));
 end

%plot
font = 'Arial';
fontsizelegend = 35;
fontsizelabel = 45;

loglog(NIEL3mat(1,1:end),NIEL3mat(2,1:end),'LineWidth',5,'
   DisplayName',sprintf('␣%s␣on␣%s%s%s,␣␣␣T_{d,%s%s%s}␣=␣%.0f
   ␣eV',particle,lattice1,lattice2,lattice3,lattice1,lattice2
   ,lattice3,Ed1));

set(gca,'FontSize',fontsizelabel,'xscale','log','XTick'
   ,[10^-4 10^-3 10^-2 10^-1 10^0 10^1],'YTick',[10^-6 10^-4
   10^-2 10^0]); %tick label fontsize
set(gcf, 'Position', get(0,'Screensize')); % Maximize figure.
xlabel({'Particle␣energy␣(MeV)'},'FontSize',fontsizelabel,'
   FontName',font,'Color','black')
ylabel({'NIEL␣(MeV␣cm^2␣g^{-1})'},'FontSize',fontsizelabel,'
   FontName',font,'Color','black')
lh = legend('-DynamicLegend','Location','southwest'); %to get
    legend from displayname
```

```
set(lh, 'Box', 'off','Fontname',font,'FontSize',
   fontsizelegend);
axis([1e-4 1e1 1e-7 1e1])

%grid
grid on;
xt = log10(get(gca,'XTick')); %for xticks 1e8 instead of 10^8
set(gca,'XTickLabel',sprintfc('1e%i',xt(1):xt(2)-xt(1):xt(
   numel(xt))),'XColor','black','GridAlpha',0.5); %for xticks
    1e8 instead of 10^8
yt = log10(get(gca,'YTick')); %for xticks 1e8 instead of 10^8
set(gca,'YTickLabel',sprintfc('1e%i',yt(1):yt(2)-yt(1):yt(
   numel(yt))),'YColor','black'); %for yticks 1e8 instead of
   10^8
```

NIEL for a 4-element material

```
function NIEL4(particle,lattice1,ratio1,Ed1,lattice2,ratio2,
   Ed2,lattice3,ratio3,Ed3,lattice4,ratio4,Ed4)

%constants
Aga=69.723;
Aas=74.92160;
Ain=114.818;
Aph=30.973761998;
Age=72.630;
Asi=28.084;
Aal=26.9815385;
An=14.00643;
Acu=63.546;
Ase=78.96;
Acd=112.411;
Ate=127.6;

%x,y boxes
switch particle
    case 'p'
        Eparvec=logspace(-4,4,300); %Energy vector in MeV
```

```
    case 'e'
        Eparvec=logspace(-1,4,300); %Energy vector in MeV
    otherwise
        Eparvec=logspace(-4,4,300); %Energy vector in MeV
end
NIEL4mat = zeros(2,size(Eparvec,2)); %solution matrix

%calculation
 for i = 1:size(Eparvec,2)
    Epar = Eparvec(i);
    %write in the solution matrix
    NIEL4mat(1,i) = Epar;
    NIEL4mat(2,i) = 1/(ratio1*Al1+ratio2*Al2+ratio3*Al3+
       ratio4*Al4)*(Al1*ratio1*NIEL(Epar,particle,lattice1,
       Ed1)+Al2*ratio2*NIEL(Epar,particle,lattice2,Ed2)+Al3*
       ratio3*NIEL(Epar,particle,lattice3,Ed3)+Al4*ratio4*
       NIEL(Epar,particle,lattice4,Ed4));
 end

%plot
font = 'Arial';
fontsizelegend = 35;
fontsizelabel = 45;

loglog(NIEL4mat(1,1:end),NIEL4mat(2,1:end),'LineWidth',5,'
   DisplayName',sprintf('␣%s␣on␣%s%s%s%s,␣␣␣T_{d,%s%s%s%s}␣=␣
   %.0f␣eV',particle,lattice1,lattice2,lattice3,lattice4,
   lattice1,lattice2,lattice3,lattice4,Ed1));

set(gca,'FontSize',fontsizelabel,'xscale','log','XTick'
   ,[10^-4 10^-3 10^-2 10^-1 10^0 10^1],'YTick',[10^-6 10^-4
   10^-2 10^0]); %tick label fontsize
set(gcf, 'Position', get(0,'Screensize')); % Maximize figure.
xlabel({'Particle␣energy␣(MeV)'},'FontSize',fontsizelabel,'
   FontName',font,'Color','black')
ylabel({'NIEL␣(MeV␣cm^2␣g^{-1})'},'FontSize',fontsizelabel,'
   FontName',font,'Color','black')
lh = legend('-DynamicLegend','Location','southwest'); %to get
    legend from displayname
set(lh, 'Box', 'off','Fontname',font,'FontSize',
   fontsizelegend);
```

```
axis([1e-4 1e1 1e-7 1e1])

%grid
grid on;
xt = log10(get(gca,'XTick')); %for xticks 1e8 instead of 10^8
set(gca,'XTickLabel',sprintfc('1e%i',xt(1):xt(2)-xt(1):xt(
   numel(xt))),'XColor','black','GridAlpha',0.5); %for xticks
    1e8 instead of 10^8
yt = log10(get(gca,'YTick')); %for xticks 1e8 instead of 10^8
set(gca,'YTickLabel',sprintfc('1e%i',yt(1):yt(2)-yt(1):yt(
   numel(yt))),'YColor','black'); %for yticks 1e8 instead of
   10^8
```

NIEL

```
function [NIELvalue]=NIEL(Epar,particle,lattice,Ed)

%constants
NA=6.02214129e23; %(mol^(-1))
%e, p, alpha
Ze=1;
Ae=5.4857990946e-4;
Zp=1;
Ap=1.007276466812;
Zalpha=2;
Aalpha=3.7273;
%elements
Zga=31;
Aga=69.723;
Zas=33;
Aas=74.92160;
Zin=49;
Ain=114.818;
Zph=15;
Aph=30.973761998;
Zge=32;
Age=72.630;
Zsi=14;
```

```
Asi=28.084;
Zal=13;
Aal=26.9815385;
Zn=7;
An=14.00643;
Zcu=29;
Acu=63.546;
Zse=34;
Ase=78.96;
Zcd=48;
Acd=112.411;
Zte=52;
Ate=127.6;

Ed = Ed * 1e-6; %unit conversion eV to MeV

%lattice and particle selection
switch lattice
        case 'Ga'
        Zl=Zga;
        Al=Aga;
        case 'As'
        Zl=Zas;
        Al=Aas;
        case 'In'
        Zl=Zin;
        Al=Ain;
        case 'P'
        Zl=Zph;
        Al=Aph;
        case 'Ge'
        Zl=Zge;
        Al=Age;
        case 'Si'
        Zl=Zsi;
        Al=Asi;
        case 'Al'
        Zl=Zal;
        Al=Aal;
        case 'N'
        Zl=Zn;
```

```
        Al=An;
        case 'Cu'
        Zl=Zcu;
        Al=Acu;
        case 'Se'
        Zl=Zse;
        Al=Ase;
        case 'Cd'
        Zl=Zcd;
        Al=Acd;
        case 'Te'
        Zl=Zte;
        Al=Ate;
        otherwise
        error('Lattice not recognized. ''Ga'', ''As'', ''In''
           , ''P'', ''Ge'', ''Si'', ''Al'', ''N'', ''Cu'', ''
           Se'', ''Cd'', ''Te'' possible')
end

switch particle
    case 'e'
        Zpar = Ze;
        Apar = Ae;
        integrand = @(E,Epar) E .* L(E,Zpar,Zl,Apar,Al) .*
           CSMott(Al,Apar,E,Epar,Zl,Zpar);
    case 'p WM'
        Zpar = Zp;
        Apar = Ap;
        integrand = @(E,Epar) E .* L(E,Zpar,Zl,Apar,Al) .*
           CSWM(Al,Apar,E,Epar,Zl,Zpar);
    case 'p ZBL'
        Zpar = Zp;
        Apar = Ap;
        integrand = @(E,Epar) E .* L(E,Zpar,Zl,Apar,Al) .*
           CSZBL(Al,Apar,E,Epar,Zl,Zpar);
end

NIELvalue = NA/Al * integral(@(E) integrand(E,Epar),Ed,Emax(
   Epar,Apar,Al));

end
```

Maximum transferred energy

```
function [Emaxvalue] = Emax(Epar,Apar,Al)
%maximum energy transfer relativistic in MeV

Eu0=931.494333558; %931.49 = 1e-6 * uc^2/e [MeV]
%Emaxvalue = 4*Epar*Apar*Al/(Apar+Al)^2; %classical
Emaxvalue = 2*Epar*(Epar + 2*Apar*Eu0)*((1+Apar/Al)^2*Eu0*Al
   +2*Epar)^(-1);

end
```

Lindhard partition function

```
function [Lvalue] = L(E,Zpar,Zl,Apar,Al)
%calculating the Lindhard partition function or 'damage␣
   efficiency'

eps = 1e6*E*Al*(30.724*Zpar*Zl*(Zpar.^(2/3)+Zl.^(2/3)).^(1/2)
   *(Apar+Al)).^(-1); %1e6 because E is in MeV but formula
   takes E(eV); @(E,Zpar,Apar,Zl,Al)
g =  eps + 0.40244*eps.^(3/4) + 3.4008*eps.^(1/6); % @(eps)
kL = 0.0793*Zpar.^(2/3)*Zl.^(1/2)*(Al+Apar).^(3/2)*((Zl
   .^(2/3)+Zpar.^(2/3)).^(3/4)*Apar.^(3/2)*Al.^(1/2)).^(-1);
   % @(Zpar,Apar,Zl,Al)
Lvalue = 1.*(1+kL*g).^(-1);

end
```

Mott scattering cross section

```
function [CSMottvalue] = CSMott(Al,Apar,E,Epar,Zl,Zpar)
% Mott-McKinley-Feshbach formula for elctron coulombic
   interactions

a0=5.2917721092e-9; %(cm)
me=9.1093897e-31;
re=2.8179403267e-13; %(cm) classical electron radius
u=1.6605402e-27; %kg
c=299792458; %m/s
e=1.60217733e-19; %As
hquer=1.05457266e-34; %Js
eps0=8.85418781762e-12; %As/Vm
alpha=7.2973525698e-3; % fine structure constant = 1/137

Epar0 = Apar * u * c^2 * 1e-6/e;
gamma = (Epar + Epar0) / Epar0;
beta = sqrt(1-1/gamma^2);

Em = Emax(Epar,Apar,Al);

CSMottvalue = 1e6*pi*Zl^2*re^2*gamma^(-2)*beta^(-4)*(1-beta*(
   beta-pi*Zl*alpha)*E/Em-pi*Zl*beta*alpha*sqrt(E/Em))*Em.*E
   .^(-2);

end
```

Ziegler-Biersack-Littmark scattering cross section

```
function [CSZBLvalue] = CSZBL(Al,Apar,E,Epar,Zl,Zpar)

a0=5.2917721092e-9; %(cm)
a=1.1383; %ZBL universal potential fitting coefficients
b=0.01321;
c=0.21226;
d=0.19593;
```

```
eps = 32.53e3*Al*Epar*(Zpar*Zl*(Apar+Al)*(Zpar^(0.23)+Zl
   ^(0.23)))^(-1); %dimensionless ZBL reduced energy; Epar in
    paper in keV, here in MeV
aU = 0.8854 * a0 * (Zpar^(0.23)+Zl^(0.23))^(-1); %ZBL
   universal screening lenth

x = eps.*(E./Emax(Epar,Apar,Al)).^(1/2); % dimensionless
   collision parameter
A = 1+a*x;
B = x+b*x.^c+d*x.^(1/2);
f = log(A)./(2.*B) + a.*x./(2.*A.*B) - x.*log(A).*(1+b.*c.*x
   .^(c-1)+(d./(2.*x)).^(1/2))./(2.*B.^2);

CSZBLvalue =  pi/2 * aU^2 * sqrt(Emax(Epar,Apar,Al))/eps * f/
   E.^(3/2)  ; %(cm^2)

end
```

Wentzel-Molière scattering cross section

```
function [CSWMvalue] = CSWM(Al,Apar,E,Epar,Zl,Zpar)
% calculating the cross section for protons like Wentzel
   Moliere

u=1.6605402e-27; %kg
a0=5.2917721092e-11; %(m)
c=299792458; %m/s
e=1.60217733e-19; %As
hquer=1.05457266e-34; %Js
eps0=8.85418781762e-12; %As/Vm
alpha=7.2973525698e-3; % fine structure constant = 1/137

Epar0 = 1e-6*Apar*u*c^2/e; %MeV
El0 = 1e-6*Al*u*c^2/e; %MeV
Ecm = sqrt(Epar0^2+El0^2+2*El0*Epar); %MeV
gamma = (Epar+Epar0)/Epar0; %unitless
beta = sqrt(1-1/gamma^2); %unitless
mur = (1e-6*u^2*c^2/e)*Al*Apar/Ecm; %kg
```

```
aTF = 0.885 * a0 / Zl^(1/3); %m
p1cm = gamma * mur * beta * c; %kg m/s
    Emur = mur * c^2 * gamma; %J
As = (hquer/(2*p1cm*aTF))^2*(1.13+3.767*(alpha*Zl/beta)^2); %
   unitless
ppar = gamma * Apar * u * beta * c; %kg m/s
q = (1e-6*c/e)* 2 * ppar .* sqrt(E./Emax(Epar,Apar,Al)); %
   relativistic momentum transfer
RN = Al^(0.27)/155; % [MeV]
F = (1+(q.*RN).^2/12).^(-2)+1/Zl; %form factor

CSWMvalue =  (1e2/(4*pi*eps0))^2*(Emur * Zpar * Zl * e^2 / (c
    * p1cm)^2)^2 * F * pi * Emax(Epar,Apar,Al).*(Emax(Epar,
   Apar,Al)*As+E).^(-2); %cm^2/MeV

end
```

List of Figures

List of Tables

Bibliography

[1] M. Becquerel, Sur la propriete qua la lumiere de rendre des corps phosphorescents,Compte rendus, seance du lundi **11** (1839).

[2] W. Shockley, The Theory of p-n Junctions in Semiconductors and p-n Junction Transistors,Bell System Technical Journal **28**, 435–489 (1949).

[3] D. M. Chapin, C. Fuller, and G. Pearson, A new silicon p-n junction photocell for converting solar radiation into electrical power,Journal of Applied Physics **25**, 676–677 (1954).

[4] Best Research-Cell Efficiencies,`https://www.nrel.gov/pv/assets/pdfs/best-research-cell-efficiencies-rev210726.pdf`. Accessed: 2021-10-15.

[5] B. Dunbar, A Short History of Earth's Radiation Belts,`https://www.nasa.gov/mission_pages/rbsp/science/rbsp-history.html`. Accessed: 2019-10-02.

[6] J. A. Van Allen, The geomagnetically trapped corpuscular radiation,Journal of Geophysical Research **64**, 1683–1689 (1959).

[7] S. Vernov and A. Chudakov, Investigations of cosmic radiation and of the terrestrial corpuscular radiation by means of rockets and satellites,Physics-Uspekhi **3**, 230–250 (1960).

[8] B. Dunbar, NASA: Radiation belts with satellites,`https://www.nasa.gov/mission_pages/sunearth/news/gallery/20130228-radiationbelts.html`. Accessed: 2022-03-17.

[9] S. M. Sze and K. K. Ng, *Physics of semiconductor devices,* (John wiley & sons, 2006).

[10] F. A. Lindholm, J. G. Fossum, and E. L. Burgess, Application of the superposition principle to solar-cell analysis,IEEE transactions on electron devices **26**, 165–171 (1979).

[11] R. Hoheisel, Charakterisierung und Optimierung von hocheffizienten III-V Weltraumsolarzellen,Ph.D. thesis, Universität Konstanz, Dr. Hut Verlag München (2011).

[12] P. Würfel, *Physik der Solarzellen,* (Spektrum, Akad. Verlag, 2000).

[13] G. Kinchin and R. Pease, The displacement of atoms in solids by radiation,Reports on progress in physics **18**, 1 (1955).

[14] M. Norgett, M. Robinson, and I. Torrens, A proposed method of calculating displacement dose rates,Nuclear engineering and design **33**, 50–54 (1975).

[15] B. Anspaugh, *GaAs solar cell radiation handbook,* (Jet Propulsion Laboratory, 1996).

[16] W. Guter, F. Dunzer, L. Ebel, K. Hillerich, W. Köstler, T. Kubera, M. Meusel, B. Postels, and C. Wächter, Space Solar Cells–3G30 and Next Generation Radiation Hard Products,in "E3S Web of Conferences," , vol. 16 (EDP Sciences, 2017), vol. 16, p. 03005.

[17] European Cooperation for Space Standardization, *Photovoltaic assemblies and components, Vol. ECSS-E-20-08C,*.

[18] E. Rapp, V. Pichetto, C. Elisabelar, C. Baur, D. Bausch, and M. Jeunet, Casolba: Balloon Calibration of Solar Cells,in "E3S Web of Conferences," , vol. 16 (EDP Sciences, 2017), vol. 16, p. 02001.

[19] O. Homburg, T. Mitra, and L. Aschke, Overview: Process-optimized beam transformers and their impact on high-power laser applications,in "Laser Resonators and Beam Control XII," , vol. 7579 (International Society for Optics and Photonics, 2010), vol. 7579, p. 75790.

[20] D. Heynderickx, B. Quaghebeur, E. Speelman, and E. Daly, ESA's Space Environment Information System (SPENVIS)-A WWW interface to models of the space environment and its effects,in "38th Aerospace Sciences Meeting and Exhibit," (2000), p. 371.

[21] S. R. Messenger, E. A. Burke, M. A. Xapsos, G. P. Summers, R. J. Walters, I. Jun, and T. Jordan, NIEL for heavy ions: An analytical approach,IEEE Transactions on Nuclear Science **50**, 1919–1923 (2003).

[22] A. Akkerman and J. Barak, New partition factor calculations for evaluating the damage of low energy ions in silicon,IEEE transactions on nuclear science **53**, 3667–3674 (2006).

[23] C. Leroy and P.-G. Rancoita, *Principles of radiation interaction in matter and detection,* (World Scientific, 2011).

[24] J. Lindhard, V. Nielsen, M. Scharff, and P. Thomsen, Integral equations governing radiation effects,Mat. Fys. Medd. Dan. Vid. Selsk **33**, 1–42 (1963).

[25] I. Jun, Effects of secondary particles on the total dose and the displacement damage in space proton environments,IEEE Transactions on Nuclear science **48**, 162–175 (2001).

[26] F. Seitz, Displacement of atoms during irradiation,Solid State Physics. **2**, 307–442 (1956).

[27] J. Ziegler, J. Biersack, and U. Littmark, The stopping Power and Ranges of Ions in Matter,The Stopping and Range of Ions in Solids **1** (1985). Accessed: 2016-01-19.

[28] S. R. Messenger, E. A. Burke, M. A. Xapsos, G. P. Summers, and R. J. Walters, The Simulation of damage tracks in silicon,IEEE Transactions on Nuclear Science **51**, 2846–2850 (2004).

[29] G. Wentzel, Zwei Bemerkungen über die Zerstreuung korpuskularer Strahlen als Beugungserscheinung,Zeitschrift f. Physik **40**, 590–593 (1926).

[30] M. Boschini, C. Consolandi, M. Gervasi, S. Giani, D. Grandi, V. Ivanchenko, and P. Rancoita, Geant4-based application development for NIEL calculation in the Space Radiation Environment,in "Astroparticle, Particle And Space Physics, Detectors And Medical Physics Applications," (World Scientific, 2010), pp. 698–708.

[31] M. Boschini, C. Consolandi, M. Gervasi, S. Giani, D. Grandi, V. Ivanchenko, S. Pensotti, P. Rancoita, and M. Tacconi, Nuclear and non-ionizing energy-loss for Coulomb scattered particles from low energy up to relativistic regime in space radiation environment,in "Cosmic Rays for Particle and Astroparticle Physics," (World Scientific, 2011), pp. 9–23.

[32] H. Bethe, Moliere's theory of multiple scattering,Physical review **89**, 1256 (1953).

[33] A. Butkevich, R. Kokoulin, G. Matushko, and S. Mikheyev, Comments on multiple scattering of high-energy muons in thick layers,Nuclear Instruments and Methods in Physics Research Section A: Accelerators, Spectrometers, Detectors and Associated Equipment **488**, 282–294 (2002).

[34] W. Bragg and R. Kleeman, On the a Particles of Radium, and Their Loss of Range in Passing Through Various Atoms and Molecules,Philos. Mag. & J. Sci pp. 318–340 (1905).

[35] I. Jun, W. Kim, and R. Evans, Electron nonionizing energy loss for device applications,IEEE Transactions on nuclear science **56**, 3229–3235 (2009).

[36] C. Baur, M. Gervasi, P. Nieminen, S. Pensotti, P. Rancoita, and M. Tacconi, NIEL dose dependence for solar cells irradiated with electrons and protons,in "ASTROPARTICLE, PARTICLE, SPACE PHYSICS AND DETECTORS FOR PHYSICS APPLICATIONS: Proceedings of the 14th ICATPP Conference," (World Scientific, 2014), pp. 692–707.

[37] G. P. Summers, E. A. Burke, P. Shapiro, S. R. Messenger, and R. J. Walters, Damage correlations in semiconductors exposed to gamma, electron and proton radiations,IEEE Transactions on Nuclear Science **40**, 1372–1379 (1993).

[38] M. Salzberger, C. Nömayr, P. Lugli, S. R. Messenger, and C. G. Zimmermann, Degradation fitting of irradiated solar cells using variable threshold energy for atomic displacement,Progress in Photovoltaics: Research and Applications **25**, 773–781 (2017).

[39] H. Tada, J. Carter Jr, B. Anspaugh, and R. Downing, *Solar cell radiation handbook,* (Jet Propulsion Laboratory, 1982).

[40] B. Anspaugh and R. Downing, *Radiation effects in silicon and gallium arsenide solar cells using isotropic and normally incident radiation,* (Jet Propulsion Laboratory, 1984).

[41] G. P. Summers, R. Walters, M. Xapsos, E. Burke, S. Messenger, P. Shapiro, and R. Statler, A new approach to damage prediction for solar cells exposed to different radiations,in "Photovoltaic Energy Conversion, 1994., Conference Record of the Twenty Fourth. IEEE Photovoltaic Specialists Conference-1994, 1994 IEEE First World Conference on," , vol. 2 (IEEE, 1994), vol. 2, pp. 2068–2075.

[42] G. P. Summers, E. A. Burke, and M. A. Xapsos, Displacement damage analogs to ionizing radiation effects,Radiation Measurements **24**, 1–8 (1995).

[43] S. Messenger, M. Xapsos, E. Burke, R. Walters, and G. Summers, Proton displacement damage and ionizing dose for shielded devices in space,IEEE Transactions on Nuclear Science **44**, 2169–2173 (1997).

[44] T. Morton, R. Chock, K. Long, S. Bailey, S. Messenger, R. Walters, and G. Summers, Use of displacement damage dose in an engineering model of GaAs solar

cell radiation damage,Progress in Photovoltaics: Research and Applications **8**, 339–343 (2000).

[45] S. Messenger, E. Burke, G. Summers, M. Xapsos, R. Walters, E. Jackson, and B. Weaver, Nonionizing energy loss (NIEL) for heavy ions,IEEE Transactions on Nuclear Science **46**, 1595–1602 (1999).

[46] S. R. Messenger, G. Summers, E. Burke, R. Walters, and M. Xapsos, Modeling solar cell degradation in space: A comparison of the NRL displacement damage dose and the JPL equivalent fluence approaches,Progress in Photovoltaics: Research and Applications **9**, 103–121 (2001).

[47] S. Messenger, E. Jackson, J. Warner, and R. Walters, SCREAM: A new code for solar cell degradation prediction using the displacement damage dose approach,in "Photovoltaic Specialists Conference (PVSC), 2010 35th IEEE," (IEEE, 2010), pp. 001106–001111.

[48] S. R. Messenger, E. M. Jackson, J. H. Warner, R. J. Walters, T. E. Cayton, Y. Chen, R. W. Friedel, R. M. Kippen, and B. Reed, Correlation of telemetered solar array data with particle detector data on GPS spacecraft,IEEE Transactions on Nuclear Science **58**, 3118–3125 (2011).

[49] S. R. Messenger, E. A. Jackson, J. H. Warner, and R. J. Walters, Advancements to SCREAM: Multiple spectrum input and ShielDDDose options,in "Photovoltaic Specialists Conference (PVSC), 2012 38th IEEE," (IEEE, 2012), pp. 003281–003286.

[50] G. Chanteperdix, C. Baur, S. Taylor, M. Meusel, L. Guillaume, and C. Theroude, Aging Effects Modelling For The New Generation Of GaAs/Ge Cells,in "9th European Space Power Conference," , vol. 690 (2011), vol. 690.

[51] C. Inguimbert and R. Gigante, NEMO: a code to compute NIEL of Protons, Neutrons, Electrons and Heavy Ions,in "2005 8th European Conference on Radiation and Its Effects on Components and Systems," (IEEE, 2005), pp. PG2–1.

[52] G. Summers, E. Burke, D. Chrisey, M. Nastasi, and J. Tesmer, Effect of particle-induced displacements on the critical temperature of $YBa_2Cu_3O_7$-δ,Applied physics letters **55**, 1469–1471 (1989).

[53] J. Grimshaw and P. Banbury, The displacement energy in GaAs,Proceedings of the Physical Society **84**, 151 (1964).

[54] A. Meulenberg, C. Dozier, W. Anderson, S. Mittleman, M. Zugich, and C. Caefer, Dosimetry and total dose radiation testing of GaAs devices,IEEE Transactions on Nuclear Science **34**, 1745–1750 (1987).

[55] J. H. Warner, S. R. Messenger, R. J. Walters, G. P. Summers, J. R. Lorentzen, D. M. Wilt, and M. A. Smith, Correlation of electron radiation induced-damage in GaAs solar cells,IEEE Transactions on nuclear science **53**, 1988–1994 (2006).

[56] E. El Allam, C. Inguimbert, T. Nuns, A. Meulenberg, A. Jorio, and I. Zorkani, Gamma and electron NIEL dependence of irradiated GaAs,IEEE Transactions on Nuclear Science **64**, 991–998 (2017).

[57] European Space Agency, *MOS.TCN.734403.ASTR,* (2009).

[58] C. Baur, M. Gervasi, P. Nieminen, P. Rancoita, and M. Tacconi, Solar cell degradation analysis applying the displacement damage dose approach using appropriate NIEL values,in "ESA Special Publication," , vol. 719 (2014), vol. 719.

[59] D. Pons, A. Mircea, and J. Bourgoin, An annealing study of electron irradiation-induced defects in GaAs,Journal of Applied Physics **51**, 4150–4157 (1980).

[60] G. A. Seber and C. J. Wild, Nonlinear regression. hoboken,New Jersey: John Wiley & Sons **62**, 63 (2003).

[61] D. C. Marvin, *Aerospace Report: TOR-00(1210)1,*.

[62] R. Campesato, C. Baur, M. Casale, M. Gervasi, E. Gombia, E. Greco, A. Kingma, P. G. Rancoita, D. Rozza, and M. Tacconi, NIEL DOSE and DLTS Analyses on Triple and Single Junction solar cells irradiated with electrons and protons,in "2018 IEEE 7th World Conference on Photovoltaic Energy Conversion (WCPEC)(A Joint Conference of 45th IEEE PVSC, 28th PVSEC & 34th EU PVSEC)," (IEEE, 2018), pp. 3768–3772.

[63] G. Siefer, C. Baur, and A. W. Bett, External quantum efficiency measurements of germanium bottom subcells: Measurement artifacts and correction procedures,in "Photovoltaic Specialists Conference (PVSC), 2010 35th IEEE," (IEEE, 2010), pp. 000704–000707.

[64] D. Pons and J. Bourgoin, Irradiation-induced defects in GaAs,Journal of Physics C: Solid State Physics **18**, 3839 (1985).

[65] T. Mattila and R. M. Nieminen, Direct antisite formation in electron irradiation of GaAs,Physical review letters **74**, 2721 (1995).

[66] G. W. Arnold and W. D. Compton, Threshold energy for lattice displacement in α-Al_2O_3,Physical Review Letters **4**, 66 (1960).

[67] F. Bryant and A. Cox, Atomic displacement energies for binary semiconductors,Journal of Physics C: Solid State Physics **1**, 1734 (1968).

[68] B. Massarani and J. Bourgoin, Threshold energy for atomic displacement in InP,Physical Review B **34**, 2470 (1986).

[69] M. Salzberger, M. Rutzinger, C. Nömayr, P. Lugli, and C. G. Zimmermann, Voltage-dependent photocurrent in irradiated GaAs solar cells,Progress in Photovoltaics: Research and Applications **26**, 317–323 (2018).

[70] R. Hoheisel, D. Scheiman, S. Messenger, P. Jenkins, and R. Walters, Detailed characterization of the radiation response of multijunction solar cells using electroluminescence measurements,IEEE Transactions on Nuclear Science **62**, 2894–2898 (2015).

[71] M. Meusel, C. Baur, W. Guter, M. Hermle, F. Dimroth, A. Bett, T. Bergunde, R. Dietrich, R. Kern, W. Köstler *et al.*, Development status of European multijunction space solar cells with high radiation hardness,in "Proc. 20th European Photovoltaic Solar Energy Conf," (2005).

[72] S. S. Hegedus, Current–Voltage Analysis of a-Si and a-SiGe Solar Cells Including Voltage-dependent Photocurrent Collection,Progress in Photovoltaics: Research and Applications **5**, 151–168 (1997).

[73] S. Hegedus, D. Desai, and C. Thompson, Voltage dependent photocurrent collection in CdTe/CdS solar cells,Progress in Photovoltaics: Research and Applications **15**, 587–602 (2007).

[74] M. Eron and A. Rothwarf, Effects of a voltage-dependent light-generated current on solar cell measurements: CuInSe2/Cd(Zn)S,Applied Physics Letters **44**, 131–133 (1984).

[75] R. Hoheisel, M. Gonzalez, M. Lumb, D. Scheiman, S. Messenger, C. Bailey, J. Lorentzen, T. Tibbits, M. Imaizumi, T. Ohshima *et al.*, Quantum-well solar cells for space: The impact of carrier removal on end-of-life device performance,IEEE Journal of Photovoltaics **4**, 253–259 (2014).

[76] S. Park, J. C. Bourgoin, H. Sim, C. Baur, V. Khorenko, O. Cavani, J. Bourcois, S. Picard, and B. Boizot, Space degradation of 3J solar cells: I-Proton irradiation,Progress in Photovoltaics: Research and Applications **26**, 778–788 (2018).

[77] X. Liu and J. Sites, Solar-cell collection efficiency and its variation with voltage,Journal of Applied Physics **75**, 577–581 (1994).

[78] D. Abou-Ras, T. Kirchartz, and U. Rau, *Advanced characterization techniques for thin film solar cells,* (John Wiley & Sons, 2016).

[79] J. Pallares, L. Marsal, X. Correig, J. Calderer, and R. Alcubilla, Space charge recombination in PN junctions with a discrete and continuous trap distribution,Solid-state electronics **41**, 17–23 (1997).

[80] S. Park, J. C. Bourgoin, O. Cavani, V. Khorenko, C. Baur, and B. Boizot, Origin of the degradation of triple junction solar cells at low temperature,in "E3S Web of Conferences," , vol. 16 (EDP Sciences, 2017), vol. 16, p. 04004.

[81] R. Hoheisel, R. Walters, and A. Bett, Low temperature effects in photovoltaic devices for deep space missions,in "Photovoltaic Specialist Conference (PVSC), 2015 IEEE 42nd," (IEEE, 2015), pp. 1–5.

[82] O. Breitenstein and S. Rißland, A two-diode model regarding the distributed series resistance,Solar Energy Materials and Solar Cells **110**, 77–86 (2013).

[83] M. Niemeyer, J. Ohlmann, A. Walker, P. Kleinschmidt, R. Lang, T. Hannappel, F. Dimroth, and D. Lackner, Minority carrier diffusion length, lifetime and mobility in p-type GaAs and GaInAs,Journal of Applied Physics **122**, 115702 (2017).

[84] M. Yamaguchi and C. Amano, 60Co γ-ray and electron irradiation damage of GaAs single crystals and solar cells,Journal of applied physics **54**, 5021–5029 (1983).

[85] S.-i. Sato, H. Miyamoto, M. Imaizumi, K. Shimazaki, C. Morioka, K. Kawano, and T. Ohshima, Degradation modeling of InGaP/GaAs/Ge triple-junction solar cells irradiated with various-energy protons,Solar Energy Materials and Solar Cells **93**, 768–773 (2009).

[86] C. Baur and A. Bett, Modeling of the degradation of III–V triple-junction cells due to particle irradiation on the basis of component cells,in "Photovoltaic Specialists Conference (PVSC), 2010 35th IEEE," (IEEE, 2010), pp. 001100–001105.

[87] M. A. Green, E. D. Dunlop, J. Hohl-Ebinger, M. Yoshita, N. Kopidakis, and X. Hao, Solar cell efficiency tables (Version 58),Progress in Photovoltaics: Research and Applications **29**, 657–667 (2021).

[88] 30% efficiency solar cell,`https://www.esa.int/spaceinimages/Images/2018/05/30_efficiency_solar_cell`. Accessed: 2019-01-23.

[89] F. Dimroth, C. Baur, A. Bett, W. Kostler, M. Meusel, and G. Strobl, Thin 5-junction solar cells with improved radiation hardness,in "2006 IEEE 4th World Conference on Photovoltaic Energy Conference," , vol. 2 (IEEE, 2006), vol. 2, pp. 1777–1780.

[90] F. Dimroth, C. Baur, A. Bett, M. Meusel, and G. Strobl, 3-6 junction photovoltaic cells for space and terrestrial concentrator applications,in "Conference Record of the Thirty-first IEEE Photovoltaic Specialists Conference, 2005.", (IEEE, 2005), pp. 525–529.

[91] G. Strobl, L. Ebel, D. Fuhrmann, W. Guter, R. Kern, V. Khorenko, W. Köstler, and M. Meusel, Development of lightweight space solar cells with 30% efficiency at end-of-life,in "2014 IEEE 40th Photovoltaic Specialist Conference (PVSC)," (IEEE, 2014), pp. 3595–3600.

[92] P. Patel, D. Aiken, A. Boca, B. Cho, D. Chumney, M. Clevenger, A. Cornfeld, N. Fatemi, Y. Lin, J. Mccarty *et al.*, Experimental results from performance improvement and radiation hardening of inverted metamorphic multijunction solar cells,IEEE Journal of Photovoltaics **2**, 377–381 (2012).

[93] M. Martinez-Sanchez and J. E. Pollard, Spacecraft electric propulsion - An overview,Journal of propulsion and power **14**, 688–699 (1998).

[94] S. R. Messenger, F. Wong, B. Hoang, C. D. Cress, R. J. Walters, C. A. Kluever, and G. Jones, Low-thrust geostationary transfer orbit (LT2GEO) radiation environment and associated solar array degradation modeling and ground testing,IEEE Transactions on Nuclear Science **61**, 3348–3355 (2014).

[95] U. Rau, Reciprocity relation between photovoltaic quantum efficiency and electroluminescent emission of solar cells,Physical Review B **76**, 085303 (2007).

[96] S. Roensch, R. Hoheisel, F. Dimroth, and A. W. Bett, Subcell IV characteristic analysis of GaInP/GaInAs/Ge solar cells using electroluminescence measurements,Applied Physics Letters **98**, 251113 (2011).

[97] T. Kirchartz, U. Rau, M. Hermle, A. W. Bett, A. Helbig, and J. H. Werner, Internal voltages in GaInP/GaInAs/Ge multijunction solar cells determined by electroluminescence measurements,Applied Physics Letters **92**, 123502 (2008).

[98] D. Alonso-Álvarez and N. Ekins-Daukes, Photoluminescence-based current–voltage characterization of individual subcells in multijunction devices,IEEE Journal of Photovoltaics **6**, 1004–1011 (2016).

[99] H. Nesswetter, N. Jost, P. Lugli, A. Bett, and C. Zimmermann, Determination of subcell IV parameters by a pulsed suns-Voc method including optical coupling,Applied Physics Letters **106**, 023903 (2015).

[100] M. Rutzinger, H. Nesswetter, P. Lugli, A. Bett, and C. Zimmermann, Determination of subcell open circuit voltages and Iph–Voc curves in multijunction solar cells by sequentially pulsed, monochromatic illumination,Applied Physics Letters **108**, 253902 (2016).

[101] M. Rutzinger, M. Salzberger, H. Nesswetter, D. Lackner, A. W. Bett, P. Lugli, and C. G. Zimmermann, Subcell Characterization in Multijunction Solar Cells Using Pulsed Light,IEEE Journal of Photovoltaics **7**, 709–714 (2017).

[102] C. G. Zimmermann, M. Rutzinger, C. Pellegrino, M. Salzberger, and H. Nesswetter, Determination of subcell properties in multijunction solar cells through pulsed illumination,in "2018 IEEE 7th World Conference on Photovoltaic Energy Conversion (WCPEC)(A Joint Conference of 45th IEEE PVSC, 28th PVSEC & 34th EU PVSEC)," (IEEE, 2018), pp. 1564–1569.

[103] M. Rutzinger, M. Salzberger, A. Gerhard, H. Nesswetter, P. Lugli, and C. Zimmermann, Measurement of subcell depletion layer capacitances in multijunction solar cells,Applied Physics Letters **111**, 183507 (2017).

[104] L. W. Nagel, SPICE-simulation program with integrated circuit emphasis,Memo No.. ERL-M382, Electronics Research Laboratory, Univ. of California, Berkeley (1973).

Publications

1. M. Salzberger, C. Nomayr, M. Rutzinger, P. Lugli, and C. G. Zimmermann, "Using variable threshold displacement energy for degradation fitting of particle irradiated multi-junction space solar cells," in "2016 IEEE 43rd Photovoltaic Specialists Conference (PVSC)," (IEEE, 2016), pp. 3405–3410.

2. M. Rutzinger, L. Krempel, M. Salzberger, M. Buchner, A. Höhn, M. Kellner, K. Janzer, C. G. Zimmermann, and M. Langer, "On-orbit verification of space solar cells on the cubesat move-ii," in "2016 IEEE 43rd Photovoltaic Specialists Conference (PVSC)," (IEEE, 2016), pp. 2605–2609.

3. M. Rutzinger, M. Salzberger, H. Nesswetter, P. Lugli, and C. Zimmermann, "Direct measurement of subcell voltage in multi-junction solar cells using pulsed laser illumination," in "43rd IEEE Photovoltaic Specialists Conference," (2016).

4. M. Salzberger, C. Nömayr, P. Lugli, S. R. Messenger, and C. G. Zimmermann, "Degradation fitting of irradiated solar cells using variable threshold energy for atomic displacement," Progress in Photovoltaics: Research and Applications 25, 773–781 (2017).

5. M. Rutzinger, M. Salzberger, H. Nesswetter, A. Gerhard, P. Lugli, and C. Zimmermann, "Measurement of subcell capacitance in triple junction solar cells with pulsed illumination," in "33rd European Photovoltaic Solar Energy Conference and Exhibition, III-V-Based Devices for Terrestrial and Space Applications, Concentrator and Space Photovoltaics, Session 4DO. 4.4," (2017).

6. M. Salzberger, M. Rutzinger, C. Nömayr, P. Lugli, and C. G. Zimmermann, "Modelling voltage dependence of photocurrent in proton irradiated gaas cells," in "2017 17th European Conference on Radiation and Its Effects on Components and Systems (RADECS)," (IEEE, 2017), pp. 1–6.

7. M. Rutzinger, M. Salzberger, A. Gerhard, H. Nesswetter, P. Lugli, and C. Zimmermann, "Measurement of subcell depletion layer capacitances in multijunction solar cells," Applied Physics Letters 111, 183507 (2017).

8. M. Rutzinger, M. Salzberger, H. Nesswetter, D. Lackner, A. W. Bett, P. Lugli, and C. G. Zimmermann, "Subcell characterization in multijunction solar cells using pulsed light," IEEE Journal of Photovoltaics 7, 709–714 (2017).

9. M. Salzberger, M. Rutzinger, C. Nömayr, P. Lugli, and C. G. Zimmermann, "Voltage-dependent photocurrent in irradiated gaas solar cells," Progress in Photovoltaics: Research and Applications 26, 317–323 (2018).

10. C. G. Zimmermann, M. Rutzinger, C. Pellegrino, M. Salzberger, and H. Nesswetter, "Determination of subcell properties in multijunction solar cells through pulsed illumination," in "2018 IEEE 7th World Conference on Photovoltaic Energy Conversion (WCPEC)(A Joint Conference of 45th IEEE PVSC, 28th PVSEC and 34th EU PVSEC)," (IEEE, 2018), pp. 1564–1569.

Disclaimer

I hereby declare that this thesis is entirely the result of my own work except where otherwise indicated. I have only used the resources given in the list of references.

Müchen, 22.03.2022 Manuel Wildfeuer

Acknowledgments

Ich möchte mich bei allen bedanken, die mich bei dieser Arbeit unterstützt haben. Besonderer Dank geht an:

Prof. Dr. Paolo Lugli für die Möglichkeit, diese Arbeit als externer Doktorand an seinem Lehrstuhl durchzuführen.

Dr. Claus G. Zimmermann für die Initiierung dieser Doktorarbeit, für die zahlreichen Diskussionen während der Doktorarbeitszeit, für das Korrekturlesen aller Paper und der Doktorarbeit und für die fachlich ausgezeichnete Betreuung während der ganzen Zeit.

Jens Birkel, Angelika Bals und Rainer Müller für die Möglichkeit, diese Arbeit in der Entwicklungsabteilung des Solargenerators von Airbus Defence and Space durchzuführen.

Martin Rutzinger für die interessanten Diskussionen über fachliche und sonstige Themen und die jederzeit angenehme Büroatmosphäre.

Dr. Christel Nömayr für die interessanten Diskussionen während zahlreicher Treffen.

Dr. Helmut Nesswetter für zahlreiche Diskussionen und Hilfestellungen bezüglich Solarzellen und deren Charakterisierung vor allem mit dem Photolumineszenzarbeitsplatz.

Helmut Janker und Matthias Nikusch für die Hilfe bei den Messungen an den Sonnensimulatoren und sonstigen technischen Fragen im Labor.

Dr. Andreas Gerhard für zahlreiche Diskussionen und die Hilfe bei den Messungen und der Kalibrierung des EQE-Messplatzes und des CV-Messplatzes mit Linuxcomputer.

Daniel von Eichhorn für die detaillierte Korrektur dieser Arbeit hinsichtlich Grammatik, Rechtschreibung und insbesondere Kommasetzung im Englischen.

Dr.-Ing. Markus Becherer für die Hilfe bei organisatorischen Fragen am Lehrstuhl und Lizenzschwierigkeiten bei Origin und dem Universitätsemailaccount.

Sylvana Strobel und Beate Griffel für die Hilfe bei organisatorischen Fragen bei Airbus.

Meine Eltern für die grossartige Unterstützung, die ich während meines Studiums und der Promotion erhalten habe.

Julia für ihre Liebe und ihre allzeitige Bereitschaft für wissenschaftliche Diskussionen.